SURFACE ACOUSTIC WAVE TECHNIQUES IN LASER PUMP-PROBE SYSTEMS AND ITS APPLICATIONS IN STUDYING MECHANICAL PROPERTIES OF MATERIALS

BY

DONGYAO LI

DISSERTATION

Submitted in partial fulfillment of the requirements
for the degree of Doctor of Philosophy in Materials Science and Engineering
in the Graduate College of the
University of Illinois at Urbana-Champaign, 2017

Urbana, Illinois

Doctoral Committee:

Professor David G. Cahill, Chair
Assistant Professor André Schleife
Professor Nancy R. Sottos
Associate Professor Taylor L. Hughes

ABSTRACT

Ultrasonic technologies in kHz and MHz frequency regime have been well developed and widely applied in the past half century, thanks to the utilization of piezoelectric transducer. Acoustic techniques that can reach GHz level is needed as the scales of materials under study reaches sub-micron and nanometer. In this dissertation, I develop and improve surface acoustic wave (SAW) techniques in optical pump-probe system, and apply them to measure shear elastic constants of thin films and damping of high frequency shear acoustic waves.

While longitudinal elastic constants of thin films can be measured conveniently in optical pump-probe system, there is no practical methods to measure shear elastic constants of thin films. I develop a SAW measurement technique using phase-shift mask in optical system. It is convenient and compatible with various kinds of thin films materials. I demonstrate the capability of the technique by measuring shear elastic constants of hard materials, soft materials, and layered materials with thickness as small as 60 nm. Ultra small shear elastic constant is observed in misfit layered compound [SnSe][$MoSe_2$].

The intrinsic attenuation of GHz acoustic wave in dielectric sets the upper bound of the quality factor of mechanical oscillation system operated at GHz frequency regime. There was no reliable experimental results regarding the intrinsic attenuation of GHz shear acoustic in Si. By careful experimental design, I am able to measure the attenuation of 7 GHz SAW on Si, which largely represents the attenuation of shear acoustic wave. The experimental scheme can be readily applied to other dielectric materials.

For quantitative analysis, I implement a general calculation scheme which can calculate SAW of layered structure with any number of layers of anisotropic material and SAW of structure with thin grating on surface. It can also be used to calculate various other acoustic modes such as Stoneley

wave and Lamb wave.

Density functional theory (DFT) calculation is used in the these studies to assist the analysis and understanding of the experiments. I calculate elastic constant of cubic crystals and hexagonal layered materials (graphite, MoS_2, and misfit layered compound [SnSe][$MoSe_2$]). I calculate the generalized mode Grüneisen parameter of Si in order to understand the relatively small attenuation of shear acoustic comparing with longitudinal acoustic wave in Si.

There is only one heroism in the world:
to see the world as it is, and to love it.
-Romain Rolland

ACKNOWLEDGMENTS

Back when I applied and started graduate school, I was hoping I could learn how to think, approach, and solve problems in different areas of science and engineering using my background in physics. I consider the goal is fulfilled now, maybe even better than I expected. This would never happen without my adviser Professor David G. Cahill. The trust and freedom he gives to me is essential for me to learn how to think and work independently. He helps me to focus when I was wandering around; he helps me to reorient when I was stuck; he teaches me how to prepare for further exploration if I am ready. Not to mention the physical intuition, scrupulous attitude, and qualities of an exceptional experimentalist that I learn from him every day. Although most of the time is not filled with rainbow, flowers, and laughter, that is when I truly learn, isn't it.

I would like to thank the Cahill group members, with no particular order: Ji Yong Park, Tamlin Matthews, Wang Wei, Trong Van Tong, Gyungmin Choi, Johannes Kimling, Judith Kimling geb Moser, Jun Liu, Qiye Zheng, Jungwoo Shin, Hyejin Jang, Ella Pek, Xu Xie, John A. Brethauer, Jordan M. Dennison, Kexin Yang, Sushant Mahat, and Zhu Diao. I would like to thank especially Richard B. Wilson, Jonglo Park, Joseph Feser, Gregory Hohensee, and Xiaojia Wang, for their friendship and the advises, help, and encouragement they gave me.

I would like to thank Li Gao, a former group member in Professor J. A. Rogers' group, and Professor Rogers himself, for their generous sharing of the technique of nano-imprint lithography.

I would like to thank Peng Zhao, a former graduate student in Professor Ji-Cheng Zhao's group in Ohio State University. His early work on calculation of SAW really helped me started to understand and develop the calculation tool that is essential to my work.

I would like to thank Professor André Schleife for his patient guidance

and advises regarding the density functional theory calculation.

I would like to express my admiration towards Professor Humphrey J. Maris at Brown University. His works on pump-probe system, SAW by metal grating, and theory of attenuation of acoustic wave in dielectrics, to name a few, are constant inspirations to me. He gave a very interesting talk about quantum mechanics recently at UIUC and I was able to meet him in person thanks to Professor Cahill. He impressed me as a role model for researchers and scientists.

I would like to thank Zichao Ye, Zhengfeng Yang, and Huize Li. We started this journey together and supported each other all the way through. This friendship is one of the biggest prizes for me of the past five plus years.

I would like to thank my wife, Jingqi Liu. Although we were either separated by the Atlantic ocean or two continents for the majority of the past nine years, you have always been the other half of my soul. So half of the degree belongs to you.

In the past five and half years, I have been together with my parents for no more than two months. And I would have never expected the day, exactly one year before the time I wrote this down, was the final goodbye to my father. I would like to thank Life, who is generous enough to let me be there with my father at the final moment. I would like to thank my mother, for everything she has sacrificed and suffered for me. I know I got an F in the subject of being a good son. I will try harder. I would like to thank my father. Your quiet and steady influence accumulated deep inside of me. You live on through me.

TABLE OF CONTENTS

CHAPTER 1

INTRODUCTION

1.1 Surface acoustic wave research and applications

Surface acoustic wave (SAW) was initially investigated to understand earthquake, as it's the wave form in earthquake that causes most damage. It was first discussed by Lord Rayleigh [1] at 1885 where the earth shell is treated as isotropic medium. The SAW on the surface of isotropic medium is later named as Rayleigh wave. Rayleigh wave has the simplest form of SAW. In Rayleigh wave, the wave energy is confined near the surface, within a fraction of wavelength deep and the displacement plane (sagittal plane) of the wave is perpendicular to the surface of the medium.

SAW of an anisotropic half-space was first studied by Stoneley [2], Gold [3], Deresiewics [4], and Synege [5] etc. at 1940s and 1950s. However most of the studies incorrectly concluded that SAW only exists in certain discrete directions or regions. This was later corrected by Lim and Farnell in a series of papers [6, 7] using better computational power at late 1960s.

This minor setback in SAW research may be seen as an indication of the complexity of SAW when anisotropy is involved. However even in the simplest case, SAW is still not intuitive comparing with bulk acoustic waves. An evidence is that until now, some papers [8, 9] in high impact journals can still make mistakes about features of SAW in isotropic material. A correct and clear picture of deformation and particle motion of Rayleigh wave of isotropic medium can be found in Professor Daniel A. Russell's webpage: `http://www.acs.psu.edu/drussell/Demos/waves/wavemotion.html`. In Chapter 3, I describe in detail a general calculation method for SAW and other acoustic behaviors.

The development of piezoelectric transducer greatly expand the application of SAW techniques. For example, SAW has been widely used in

acoustic filters and sensors. SAW filters have been at the center of the wireless communication for decades till today. As the continuous development of smart phones and the proposed "Internet of Things" in recent years, the industries call for acoustic filters with higher frequencies and higher quality factors. Two of the key fundamental knowledge involved in the development of acoustic filters are the stiffness of the material and acoustic attenuation of the materials, which are at the center of this thesis.

Recently, there is a renewed interest in SAW using piezoelectric transducer for the application of quantum computation [10, 11, 12, 13, 14]. Although these studies are out of the scope of current thesis, it's my hope that this work can open up the possibilities of using optical systems in these experiments.

From a broader perspective, the development of piezoelectric techniques greatly improved the capability and application of acoustic techniques. Medical ultrasound or diagnostic sonography has been a routine examination in medical treatment. Acoustic method with piezoelectric transducer were widely used to measure elastic constants of various bulk materials in the 50s and 60s last century, especially by H. J. McSkimin in Bell Telephone Laboratories. The applications of acoustic technique as a non-destructive technique in materials science and as sensor in biological or medical application are still very active research areas.

The huge success of piezoelectric transducer, however, also pose a limitation to the acoustic technology: the piezoelectric transducer is a necessity. The available piezoelectric material is limited and the transducer needs to be attached to the specimen. These requirements greatly limit the application of acoustic waves as a general characterization tool for materials of small scale.

Due to the reasons above, people started to investigate acoustic techniques without piezoelectric transducers. In the late 80s and 90s, several ultrasonic techniques using optical systems started to appear. The longitudinal acoustic echo technique described in Sec. 2.2 is a very good example. Another example is the spontaneous Brillouin scattering. It is widely used to study the longitudinal speed of sound or elastic constant of transparent materials. In Chapter 2, I briefly describe the optical pump-probe systems which I use extensively. My main work during Ph.D. is to develop, improve, and utilize measurement techniques of SAW measurement in optical pump-probe

systems.

Ultrasonic techniques using piezoelectric transducer have been utilized to generate both longitudinal and transverse bulk acoustic wave in bulk materials, so people can measure the full set of elastic constants. Despite the huge success in longitudinal acoustic echo technique, there are no effective methods to generate bulk transverse acoustic wave in optical pump-probe system. The key reason is that it's difficult to break the symmetry in the form of shear optically and it can also be difficult to detect the pure shear deformation optically. In order to study the shear mechanical properties of thin film materials, SAW is a good alternative. Because SAW involves complicated deformation but mostly shear, which is demonstrated in Chapter 6.

SAW also has inherent advantage as characterization tool for thin film materials, since the wave energy is mostly confined close to the surface within about wavelength deep into the material. In another word, it is mostly sensitive to the top layer. SAW with higher frequency (smaller wavelength) is capable of measuring thinner films. The time-resolved optical pump-probe system using femtosecond pulse laser provides the highest possible frequency response. Other methods are needed to define a high spatial frequency in order to generate high frequency SAW.

1.2 Surface acoustic wave techniques in optical pump-probe system

If one wants to use high frequency SAW (high MHz to GHz) as a general characterization tool, generating and detecting SAW by piezoelectric transducer is not a feasible approach. This is because it typically requires metal fingers on top of a layer of piezoelectric materials, just like in a SAW filter. Metal fingers are made by complicated fabrication process on the materials under study and they limit the sensitivities of the measurement.

The optical method is preferable to generate high frequency SAW as characterization tool for thin film materials, as it is inherently non-contact and non-destructive. One method developed in the 90s and early this century is the transient grating technique developed by Nelson group at MIT [15]. This technique is a modification of the standard optical pump-probe system which is described in Chapter 2. In transient grating technique, the pump

pulse is further split to two separate pump beams in the downstream and focused on the sample surface at an angle θ with each other. Since the two pump pulses are coherent, they interfere with each other and create a periodic intensity pattern on the sample surface. The periodicity Λ of the pattern is:

$$\Lambda = \frac{\lambda}{2\sin(\theta/2)} \tag{1.1}$$

where λ is the laser wavelength and θ is the separation angle between two pump pulses. This periodic intensity pattern causes periodic heating on the metal surface and generates SAW by thermal expansion. The transient grating refers to the periodic heating pattern, in the sense that it only appears at the moment when the two pump pulses interfere with each other on the surface, not a permanent grating. The transient grating method is a completely non-contact technique. No sample preparation is required other than a possible thin metal film deposited on the top surface. It has been used mostly on polymer films to identify acoustic modes and detect possible delaminated interface between polymer and substrate [15]. It has also been used to measure thickness of metal films [16] and later to measure nanoscale thermal transport [17, 18].

However the wavelength of SAW generated by transient grating method is limited by the laser wavelength and separation angle. In practice, it's very difficult to create a large θ. The typical wavelength generated by transient grating is usually on the level on several micron. This means that it is not sensitive films of sub-micron to tens of nanometer thickness. Another difficulty in transient grating method is the detection scheme. In principle it relies on surface displacement caused by SAW on a homogeneous surface which is a second order effect. This can be mitigated using the thermal background to make the signal to be at the first order. However it means that if one wants to measure SAW propagated far away, the heterodyne detection scheme must be used. This will further complicates the already relatively complicated optical setup. Due to various restraint, the transient grating method has not really been used to measure shear elastic constants of thin films.

An alternative technique to transient grating is to use "permanent grating". A sub-wavelength scale metal grating can be patterned on the sample surface and interrogated using conventional pump-probe techniques [19]. In

this case, the periodic heating is caused by the heating of periodic metal bars. So the wavelength of SAW, which is the same as the periodicity of the grating, can be as small as several tens of nanometers. But this is no longer a non-contact measurement. The nanofabrication processes required, such as electron-beam lithography and focused-ion beam machining, often have restrictive requirements on the chemistry and surface properties of the sample which make these approaches impractical for many materials of interest. Electron-beam lithography and focused-ion beam machining are also costly and time consuming. So the SAW measurements using metal grating have not been widely used to measure elastic constants of different films [19]. However if more convenient and compatible nanofabrication techniques are feasible, such as the laser lithography systems of Nanoscribe, the patterned metal gratings can still be good approach to measure GHz frequency SAWs.

In Chapter 4, I describe the technique I have developed for generating and detecting GHz frequency SAWs using a phase-shift elastomeric mask in conventional optical pump-probe systems, for the purpose of measuring shear elastic constant of thin film materials.

1.3 Outline of the Thesis

In this thesis, I focus on the SAW techniques in optical pump-probe system and its application in mechanical property measurement, specifically, the elastic constant measurements and attenuation measurements. This work involves nanofabrication, characterization, calculation, and simulation. I try to provide enough details of theories and experiments in the thesis for the purpose that people who are interested can fully understand and reproduce these results.

In Chapter 2, I describe the ultra-fast optical pump-probe system that I use extensively in the work. The optical pump-probe measurement is a rich measurement scheme with a further extension to the time-domain thermoreflectance (TDTR) technique. In this chapter I focus on two of the key concepts of the systems: phase-sensitive detection and the measurement in frequency domain. Two commonly used experimental methods in my work are described, namely the longitudinal acoustic echo measurement and nanoimprint lithography.

Chapter 3 first summarizes fundamental knowledge that is necessary for the calculation of SAW. Then I describe in detail the math involved in the calculation of SAW on a half-space, layered structure of any number of layers, and with thin metal grating on top of half-space. I also demonstrate the generality of the calculation method by expanding the calculation to acoustic modes other than SAW. At the end of the chapter, I briefly introduce my implementation of the SAW calculation using `MatLab`.

Chapter 4 is about the new SAW measurement technique in optical pump-probe system I developed using a phase-shift mask. This technique is for the purpose of measuring shear elastic constant of any thin film materials conveniently. The chapter includes the design, experimental procedures, and experimental validation of the technique.

In Chapter 5, I describe how to measure shear elastic constant of different thin film materials. It summarizes several applications of the SAW technique developed in Chapter 4 and demonstrates its capabilities. In the chapter I list the observations, details, and tricks in the measurement so the technique can be easily repeated and possibly improved later. At the end of the chapter I especially talk about the ultra small shear elastic constants I measured in the misfit layered compound $[SnSe]_n[MoSe_2]_n$ with $n = 1, 2, 3$.

In Chapter 6, I describe how to measure the attenuation of 7 GHz SAW on Si. An accurate attenuation measurement for high frequency acoustic wave requires careful experimental design and data analysis, which I state in detail. This experiment process I developed can be readily used for measuring attenuation of SAW on any materials that can be fabricated with a set of thin metal gratings.

In Chapter 7, I describe how to calculate elastic constant and Grüneisen parameter using density functional theory (DFT). The calculation of elastic constants is to assist the shear elastic constants measurements for crystal with relatively low symmetry. The calculation of Grüneisen parameter is for further understanding of acoustic attenuation in silicon. A more involved theory of solid mechanics is introduced to better understand the Grüneisen parameter and experimentally measured third order elastic constant (TOEC)

Chapter 8 is the conclusion and summary of the whole dissertation.

CHAPTER 2

EXPERIMENTAL METHODS

2.1 Experimental paradigm of optical pump-probe system

Early applications of optical pump-probe system can be found in the work of Paddock and Eesley [20] and of Maris and Tauc [21]. The concept of optical pump-probe system is straightforward. A pump laser pulse first hits the sample to excite certain physics phenomenon, such as thermal, mechanical, or magnetic process. Then a probe pulse reflects from the sample surface after a certain time delay and is collected by the detector. The change of reflectance of probe pulse is extracted from the signal of photodiode by a lock-in amplifier. The reflectance change is then interpreted to understand the underlying physical process.

Generally an optical measurement can suffer from huge noise from the ambient light. Typically the thermorelectance coefficients are on the order of 10^{-5} K^{-1}. The change of reflectance due to acoustic behavior in our measurement is on the order of 10^{-6} to 10^{-5}. The key technique that the optical pump-probe system uses to capture such tiny reflectance change is the *phase sensitive detection*. Next I briefly describe the concept of phase sensitive detection.

2.1.1 Phase-sensitive detection

In phase-sensitive detection, we are given the signal V received by the detector which contains the signal of interest with frequency f_s:

$$V = V_s \sin(\omega_s t + \theta_s) + V_{noise} \tag{2.1}$$

where V_s is the amplitude of the signal of interest, θ_s is the phase, and V_{noise} is the noise signal. The noise can be from many different sources and it is typically huge and spreads over wide range of frequencies.

In the optical pump-probe systems, the pulsed excitation is modulated at frequency f_s. So the physical processes excited contain the response at frequency f_s (and angular frequency $\omega_s = 2\pi f_s$) along with responses at other frequencies. The behavior of the pulsed excitation and detection will be discussed in detail later.

A band pass filter centered at f_s cannot successfully filter out the signal of interest. This is because a band-pass filter with extremely narrow bandwidth (or extremely high quality factor) is difficult to make. Even if it is possible, the properties of the devices (such as operational amplifiers) inside the band-pass filter can vary due to environment, such as temperature. This can cause the center frequency of the filter to drift which severely affect performance.

The trick in phase-sensitive detection is to utilize a reference signal: $V_r \sin(\omega_r t + \theta_r)$. The reference and the signal are multiplied with each other:

$$\begin{aligned} V_{psd} &= V_s \sin(\omega_s t + \theta_s) V_r \sin(\omega_r t + \theta_r) \\ &= \frac{1}{2} V_s V_r [\cos((\omega_s - \omega_r)t + \theta_s - \theta_r) - \cos((\omega_s + \omega_r)t + \theta_s + \theta_r)] \end{aligned} \tag{2.2}$$

If $\omega_s = \omega_r$, the V_{psd} has the DC component of $V_r V_s \cos(\theta_s - \theta_r)$. If V_{psd} goes through a low pass filter, which is easier to make and much more stable than a narrow band-pass filter, the DC component left is:

$$V_{psd} = \frac{1}{2} V_r V_s \cos(\theta_s - \theta_r) \tag{2.3}$$

which is proportional to V_s. For the noise and responses that are far away from the reference frequency f_r, their contribution after multiplication doesn't have DC components and they are completely removed by the low pass filter.

In practice, a second PSD signal is obtained by multiplying signal with reference shifted by $\pi/2$, i.e., $V_r \sin(\omega_r t + \theta_r + \pi/2)$. The low pass filter output is

$$V_{psd2} = \frac{1}{2} V_r V_s \sin(\theta_s - \theta_r) \tag{2.4}$$

The purpose of the second PSD signal is to help remove the phase depen-

dence. By setting the amplitude of reference to be 1, two output are obtained from the lock-in amplifier: $X = V_s \cos(\Delta\theta)$ and $Y = V_s \sin(\Delta\theta)$, where $\Delta\theta$ is the phase difference between the signal and reference. X is called the *in-phase* signal and Y is called the *out-of-phase* signal. V_s can be calculated: $V_s = \sqrt{X^2 + Y^2}$.

If $e^{i\omega t}$ is considered as a Fourier kernel rather than $\cos(\omega t)$ or $\sin(\omega t)$ in the Fourier transform, the lock-in amplifier can also be viewed as a Fourier transform machine that can output the Fourier components where the reference is at. In Fourier transform, the "reference signal" is $e^{i\omega t}$. In lock-in amplifier, if the reference signal is set to be *in-phase* with $e^{i\omega t}$, then the in-phase signal is the *real part* of the Fourier transform at frequency f_r; the out-of-phase signal is the *imaginary part* of the Fourier transform at frequency f_r.

In practice, the reference signal used is typically not sine wave, since it is relatively difficult to generate a perfect sine wave in digital circuits. A square wave with 50% duty cycle is usually used as the reference signal, which contains multiple frequency components at f_r, $3f_r$, $5f_r$, etc. In this case if only the physical response at frequency f_r is desired, the higher harmonic components in the signal should be filtered out before the signal entering the lock-in amplifier. Because lock-in amplifier is not capable of removing frequency components that the reference signal also contains. In the optical pump-probe system, a reference signal of square wave ($f_r \approx 10$ MHz in our systems) is generated by a function generator and feeds into both the lock-in amplifier and electro-optic modulator (EOM). The EOM modulates the pump pulses so the excitation has the f_r component (and also $3f_r$, $5f_r$, etc.), which makes the response also contain the f_r component (and $3f_r$, $5f_r$, etc.). The reflected probe beam is collected by the photodiode and fed into the lock-in amplifier after going through a resonance filter centered at f_r. The lock-in amplifier picks out the response at frequency f_r and output both in-phase and out-of-phase signals, comparing the phase of the signal with the reference. This is the basic interpretation of the in-phase signal (V_{in}) and out-of-phase signal (V_{out}) in our pump-probe systems. The physical interpretation of the V_{in} and V_{out} in the measurement is more complicated and is discussed in Sec. 2.1.3.

2.1.2 Setup of optical pump-probe system

The optical pump-probe system has been developed in the past decades to become the time domain thermoreflectance (TDTR) technique, which is one of the best way to measure thermal properties of material. TDTR has been the workhorse in Cahill group and I have been using the system for all the acoustic measurements. The signal I collect is not the thermoreflectance but the reflectance change due to acoustic phenomena.

The schematic of the optical pump-probe system I used can be found in Fig. 2.1. The light source is a $\approx$ 80 MHz mode-locked Ti:sapphire laser centered at wavelength of $\approx$ 785 nm. Every $\approx$ 12.5 ns, a laser pulse of a few hundreds of femtosecond is emitted from the laser source, and the laser pulse is separated by a polarizing beam splitter into a pump pulse and probe pulse. The polarization of pump and probe pulse is perpendicular to each other. The pump pulse then passes through an electro-optic modulator (EOM) at $\approx$ 10 MHz, and a delay stage to change the length of optical path of the pump beam, and finally focused on the sample surface by an objective lens. The path of probe pulses is different. The probe pulses go through a chopper modulated at 200 Hz before the probe pulses are focused on the sample surface by the same objective lens. During measurements, the length of the optical path of pump beam is changed by the delay stage, which introduces a time delay between the arriving time of pump pulse and the corresponding probe pulse at the sample surface. This time window is limited by the length of the delay stage and is about 4 ns in our current setup.

In our setup the pump and probe pulses are at normal incidence and their paths are overlapped with each other. This is very convenient for the setup and alignment. But in this geometry the pump pulse can be reflected back into the photodiode. This part of pump pulse is the noise that cannot be removed by the lock-in amplifier. There are two designs in the system to remove the reflected pump pulse from final signal. First the pump-probe system employs the two-tint feature, which means that pump and probe pulses have slightly different wavelength and a sharp edge filter is used to remove majority of the reflected pump beam. Second design is the addition of a chopper on the probe path operating at 200 Hz. The chopper introduces $\approx$ 200 Hz frequency to the physical responses of interest. The in-phase and

out-of-phase signal from the physical lock-in amplifier are next processed by a computer lock-in amplifier with the reference frequency same as the chopper frequency, which is read by a sensor located at the chopper.

One important feature in the measurements of optical pump-probe systems is the accumulation effect. In the thermal analysis, the accumulation effect is related with the fact that the thermal process can last longer than 12.5 ns. The thermal responses corresponding to each pump pulse accumulate with each other in time domain. Accumulation effect in thermal measurement mostly affect the out-of-phase signal. It was indeed the understanding and utilization of the out-of-phase signal that greatly improved the capability of TDTR in thermal measurement. A good picture is made by Aaron Schmidt [22] to describe the accumulation effect in TDTR (although the figure does not plot the accumulation effect quite correctly). The mathematical treatment can be found in the theory of TDTR by Cahill [23]. In acoustic measurement, the accumulation effect also exists but in a clearer form as I describe later in Chapter 6.

2.1.3 Pulsed excitation and detection in the frequency domain

The nature of pulsed excitation with modulation complicates the measurement scheme. Although the final signal is plotted in the time domain (delay time between pump and probe pulse), the measurement cannot be viewed as simple time domain measurement. This section does not try to cover the whole idea behind the experimental scheme in frequency domain but only discusses the application in optical pump-probe systems, in order to deepen the understanding of the application of optical pump-probe systems in the measurements of mechanical oscillations.

I would like to introduce the concept of "excitation and response" or more specifically the linear response to an excitation. This is used again in Chapter 3. In my understanding, "response" is a way to view any physical process. In this point of view, a physical process is composed of three components: the excitation, the response function, and the response. A particular excitation generates a particular response through the response function. The excitation is applied to the system in experiments. The response function contains all the underlying physics. The response is observed/measured

in experiments corresponding to the particular excitation. The advantage of considering physics problem from this point of view is that the problem can be first understood/solved under simple excitation and solutions to more complicated cases can be constructed based on the solutions of simple cases. based on the response theory. A simple excitation can be a plain wave excitation, because it usually leads to very simple solution of the partial differential equations; it can also be a delta function, because a delta function (in time domain or spatial domain) contains all the Fourier components (in frequency or spatial frequency domain).

A necessary theorem involved is the convolution theorem, which states that the Fourier transform of a convolution of product in one domain (for example, time domain) equals point-wise multiplication in the Fourier transform domain (for example, frequency domain):

$$\mathcal{F}[f * g] = \mathcal{F}[f]\mathcal{F}[g] \tag{2.5}$$

where $*$ represents convolution and $\mathcal{F}$ represents Fourier transform.

In optical pump-probe method with pulsed laser, a single pulse can be viewed as delta function since the length of one pump pulse (a few hundreds fs) is assumed much shorter comparing with the physics process under investigation. The total excitation of the pump pulse train is a Dirac comb, i.e. a periodic delta function, with frequency f_0. In frequency domain the excitation is also a Dirac Comb contain frequencies components: ... $-2f_0$, $-f_0$, 0, f_0, $2f_0$, $3f_0$, ... :

$$\sum_n \delta(\omega - n\omega_0) \tag{2.6}$$

where $\omega_0 = 2\pi f_0$. If the response of the system is $G(t)$ (in time domain) or $g(\omega)$ (in frequency domain) with respect to a delta excitation, the responses subject to an excitation of Dirac comb is the convolution between Direct comb and $G(t)$ at time domain and product between Direct comb and $g(\omega)$ in frequency domain.

The probe pulse train, which is the same pulse train as the pump with a time delay (which introduce a phase difference between the two in frequency domain), measures the response. The measured signal is the product between the probe and the response in the time domain. The measured signal can also be calculated as the convolution between the probe and the responses

in the frequency domain. The convolution in the frequency domain basically makes sure that probe can collect all the responses excited by the pump pulse train.

For thermal process, the thermal responses can be at any frequency. The analysis of the measurement scheme of thermal measurement (i.e., TDTR analysis) can be found in Ref. [23]. For mechanical oscillation, the situation is slightly different. For a particular oscillation system, the response in frequency domain is centered at one inherent frequency, which is determined by the mechanical properties of the system. The width of the response in frequency domain represents the quality factor Q of the mechanical oscillation. Higher quality factor Q indicates narrow response of high peak amplitude and low damping of the oscillation. In excitation, the Dirac comb of pump excitation multiplies with this response in frequency domain. If the response is very narrow, the excited responses can possibly be far away from the resonance frequency. This can be seen from the Fig. 2.2. In reality, there is always damping in the mechanical system so the response always has finite width. The damping can be from any energy loss mechanism or can be simply from the fact that the acoustic wave propagates out of the measurement area.

If the laser frequency can be tuned so that the excitation can sweep the response at frequency domain, the response function can be plotted in frequency domain and the quality factor can be measured. I have tried this in the past. But for various reasons I didn't obtain useful results.

2.2 Longitudinal acoustic echo measurement

One of the success at the early stage of the development of optical pump-probe system is the technique named by H. Maris and J. Tauc *et al.* as the "picosecond ultrasonic" techniques [24]. Before people figured out how to effectively analyze the thermal signal, one direct observation is the acoustic signal appeared in the reflectance change. The advantage of the technique is its convenience and versatility. It can be used to measure elastic constants, film thickness, and acoustic attenuation. This technique was later commercialized and is utilized now in the "MetaPULSE" system made by Rudolph Technology. It is widely used, especially in the semiconductor industry, as

a very convenient technique for thickness measurements for opaque layers or multilayer. I refer to this technique as the longitudinal acoustic echo measurement in order to distinguish it from the other SAW measurements.

2.2.1 Measurement techniques

The concept of the longitudinal acoustic echo measurement is very straightforward and the schematic is shown in Fig. 2.3. In the measurement, if the top film or film of interest cannot absorb the laser effectively, a thin metal film is deposit on the top. We usually use Al. In the optical pump-probe measurement, a pump pulse first hits the sample surface. The pump pulse is partially absorbed by the top metal layer, assuming Al. Then the temperature of Al layer increases and causes thermal expansion within Al. The thermal expansion causes strain and further generates a longitudinal acoustic wave. The longitudinal acoustic propagates downward into the structure (not upward into air due to the huge impedance mismatch between metal and air). During the propagation, part of the the longitudinal acoustic wave can be reflected by every interface and propagates toward surface. The strength of the reflected echo is determined by the acoustic impedance mismatch at each interface. After the reflected echo reaches the top surface, it can be measured by the probe beam in the time domain. Note that in our setup the pump and probe beam are overlapped on the sample surface, which is not shown in Fig. 2.3.

Fig. 2.4 shows a typical longitudinal acoustic echo signal corresponding to the sample structure in Fig. 2.3. If one can identify each echo and assign it to an interface, the travelling time t_l of the longitudinal acoustic wave within each layer can be calculated. So if the film thickness h is known, one can calculate the velocity of longitudinal acoustic wave by $v_l = 2h/t_l$ and further calculate the corresponding elastic constant by $c_l = \rho v_l^2$ given the density of the film ρ. On the other hand, if the velocity of longitudinal acoustic wave v_l is known, one can obtain the film thickness $h = v_l t_l/2$. As mentioned before, this technique is used mostly in industry to measure film thickness of opaque films. During my work, this technique is used extensively to measure the longitudinal elastic constant of thin films.

The longitudinal acoustic echo technique has been further used in other

studies such as attenuation measurement [25], etc. I won't describe the detail of these studies.

2.2.2 Detection mechanism in longitudinal acoustic echo measurement

It's important to understand the generation and detection mechanism of the physical process measured by pump-probe system in order to improve and develop techniques. In longitudinal acoustic echo measurement, the longitudinal acoustic wave is excited by the strain caused by thermal expansion. In detection, the optical pump-probe technique measures the change of reflectance of the probe pulse. Generally speaking, two kinds of mechanisms can contribute to the change of reflectance. The first one is the change of the refractive index; the second kind is any phenomenon of interference, diffraction, or scattering.

In longitudinal acoustic echo measurement, the detection mechanism is mostly from the piezooptic effect. The piezooptic effect, similar to the piezoelectric effect, is the change of refractive index due to the strain applied to the material. The reflected acoustic echo can certainly cause (mostly perpendicular) displacement of the top surface. This bump on the surface can scatter the probe beam. However in the typical setup the scattered light can still be collected by the objective length and reflected back to the photodiode, since detector has relatively large area and the deflection angle is very small. So this surface displacement cannot contribute to the change of reflectance in a typical pump-probe setup. More designs are needed in order to be sensitive to the surface displacement, for example, the beam deflection measurement. The SAW measurement introduced in Chapter 4 is sensitive to the phase change due to the perpendicular surface displacement.

Since the detection is mostly from piezooptic effect, the materials with smaller piezooptic coefficient have weaker detection signal. For example, the standard longitudinal acoustic echo technique cannot be used for Au film. To measure acoustic echo in Au film, the scattering of probe beam caused by the small displacement is utilized. An aperture or blade can be put in front of the photodiode to block part of the reflected probe that is scattered by the bump at the surface.

We will see later that for different acoustic behavior, the detection mechanism may very well be different. A good understanding of the detection mechanism is helpful to develop and improve the measurement techniques.

2.3 Nano-imprint lithography

As mentioned in Sec. 1.2, SAW can be generated and measured optically using a patterned metal grating. A major restriction to this technique is the nano-fabrication process. As is discussed in Chapter 6, the SAW technique using metal grating is necessary in the attenuation measurement. The feature size of metal bar is a ≈ 300 nm which is too small for the photolithography capability on our campus. So I am in need of a nano-fabrication method, that is capable of making feature size of a few hundred nanometer and also convenient and have high throughput and large pattern area.

After many literature search and trials/experiments, I learned the hard truth: it is very difficult to reproduce a non-standard or an advanced nano-fabrication technique by just reading journal papers. But I was fortunate to be able to learn the nano-imprint lithography from Li Gao, a former member in Professor J. A. Rogers' group. After some tuning and refinement, I was able to successfully fabricate the required grating patterns. In this section, I describe all the details in this nano-fabrication technique and hopefully people who want to use it again would have a better experience than I did.

The nano-imprint lithography is a kind of soft-lithography [26]. The main idea behind it is to define the nano-structure by deforming the soft resist using a hard stamp. The commonly used hard stamp is a silicon mold with desired feature. The commonly used soft resist is a certain kind of PMMA. This "imprint" process typically requires external pressure on the level of kPa or even MPa, using a special instrument to apply the external pressure. This external pressure is one of the major disadvantages, because it's difficult to apply a homogeneous/proper pressure and it could damage the hard stamp.

The nano-imprint lithography I describe here [27, 26] deviates from the standard imprint lithography. To my understanding, the key is to use a kind of SU8 monomer as the soft resist. This SU8 monomer has a workable 95 °C glass transition temperature. And it has low enough viscosity so that it can

be deformed easily without any external pressure when the temperature is beyond the glass transition temperature. The full name of the resist monomer in solid form is: Hexion EPON Resin SU-8 (Also known as EPIKOTE 157), Bisphenol A novolac Epoxy Resin 28906-96-9. To make the solution of resist, the monomer solid is dissolved in cyclopentanone (29770-1L Fluka Analytical $> 99.0\%$, C5H8O). The viscosity of the SU8 solution is determined by the concentration. It's very important to tune the viscosity to the proper level to have the proper thickness of the resist. The concentration I use in the end is 6% by weight.

With a resist that is very easy to work with, there are many options for the stamp. The stamp I use is made of polydimethylsiloxane (PDMS), with a layer of stiffer PDMS (hard-PDMS) on the grating side of the stamp. This so-called "hard-PDMS" is made by first mixing of 3.4 g trimethylsiloxyterminated vinylmethylsiloxane-dimethylsiloxane (VDT-731, Gelest) with 2 drops of 1,3,5,7-Tetravinyl-1,3,5,7-Tetramethylcyclotetrasiloxane (SIT 7900.0, Gelest) and 1 drop of Platinum-divinyltetramethyl-disiloxane comple in xylene (SIP 6831.2). Mix them for 2 minutes and then add 1 g of methylhydrosiloxane-dimethylsiloxane (HMS-301, Gelest) copolymers [28], mixing for another 2 minutes. Then the mixer is cast on the surface a commercial silicon grating mold (LightSmyth Technology) with the desired feature. Everything is now placed in a plastic petri dish. The hard PDMS typically cannot wet the Si master very well. One can try to evenly distribute it by blowing N_2 on it. In practice I found the hard PDMS can wet an old Si master that have been used many times much better than a new Si master. There will be a lot of bubbles in the solutions. So the petri dish is placed inside a desiccator connected with a pump to degas. After any obvious bubbles are gone, the petri dish is placed inside an oven at 80°C for about 6 mins to cure the hard PDMS. The hard PDMS is cured very fast comparing with the conventional PDMS. After curing, one can test the property of the hard PDMS using the part that is not on the stamp. It's not rubber like and very brittle. The thickness of the hard PDMS layer is about 1 mm or less.

Then the conventional PDMS (Sylgard 184, Dow Corning) is cast on top of everything. The conventional PDMS forms the majority of the stamp so that it is easy to handle. I usually place a very thick layer (> 1 cm) of PDMS on top. The recipe of the conventional PDMS is the typical 10:1 ratio of polymer and curing agent by weight. After mixing there are a lot

of bubbles. The conventional PDMS is degassed again inside a desiccator under vacuum until all obvious bubbles are gone. Then the whole petri dish is placed in the oven at 80°C. After curing (at least 2 hours), the stamp is peeled off from the Si master. Then its backside is immediately attached to a new and clean glass slide. The clean surface of the newly made PDMS can attach to the glass slide very well. It won't fall off unless it is intentionally peeled off. The purpose of the glass slide is again for the easy handle of the stamp. One no longer needs to touch the PDMS part but can just work with the large glass slide either with hand or tweezer. This stamp is now ready to be used in nano-imprint lithography. Fig. 2.7 is a picture of one PDMS stamp I made.

A thin Al layer ($\sim$ 15 nm) is first sputtered onto the sample surface. To prepare the sample for nano-imprint lithography, I spin coat (2000 rpm for 30 s) SU-8 monomer solution prepared before on top of the Al film, followed by curing at 65 °C for 1 min and 95 °C for 1 min successively on a hot plate. The glass transition temperature of the SU-8 monomer film is $\approx$ 95 °C. Then the PDMS stamp is placed on top of the sample, on a 95 °C hot plate. The weight of the stamp is sufficient to press the stamp into the resist; i.e., no external force is needed. After $\approx$ 1 min, the sample is taken off the hot plate and cooled to room temperature. In the end the stamp is peeled off and the SU8 layer is deformed with the desired structure.

I then use reactive ion etching (RIE) to remove the thin SU-8 regions and expose the Al underneath without etching through the thick SU-8 regions. The RIE tool parameters are an oxygen pressure of 100 mTorr, rf power of 100 W, and 20 s etching time. However the parameter can vary due to different RIE tool and different environment such as temperature. So the RIE condition needs to be tuned. In RIE, the etching process includes both chemical etching and physical etching. The physical etching has a preferred etching direction, i.e. it etches mostly in the direction perpendicular to the surface. But the chemical etching is isotropic. It will also make the remaining SU8 pillar narrower. The chemical etching is always inevitable. The width of remaining SU8 directly affects the filling factor, i.e. the ratio between the width of metal bars and the periodicity of grating, of the final grating feature. As will be discussed in Chapter 6, the filling factor is an important parameter to control. It's usually preferable to have a relatively wide remaining SU8, since one can always make it narrower with longer RIE etching time. One

trick is to choose the Si master with wider intrusion region (I use close to 55%) so the SU8 feature, which has the same geometry (inverse of PDMS stamp) of Si master, inherently has wider protrusion part. Another trick is to make the thin part of SU8 pattern as thin as possible so it only require very short (a few tens of seconds) to etch away all the thin part of SU8. To achieve this, one needs to tune the concentration of SU8 solution which changes the viscosity and the thickness of the spin-cast film. Usually it's more effective to change the viscosity than the parameter in spin coating to change the resulting film thickness. A change in viscosity can also affect how much SU8 can be pushed away by the stamp during the imprint. They can all affect the final thickness of the thin region of SU8. The concentration cannot be too low either, or the result of imprint won't be homogeneous. Fig. 2.5 is the SEM image of after the RIE. The darker region is the SU8; the brighter part is the exposed Al.

The exposed Al is then chemically etched (Al etchant D, Transene) at room temperature for approximately 100 s. Finally the remaining SU-8 is removed using RIE (100 mTorr oxygen, 400 W rf power, 5 mins). The filling factor can also be tuned by controlling the time of Al wet etching. Al grating with 50% and 35% filling factor have been fabricated in my experiment. Fig. 2.6 is the SEM figure of the final grating structure.

2.4 Figures

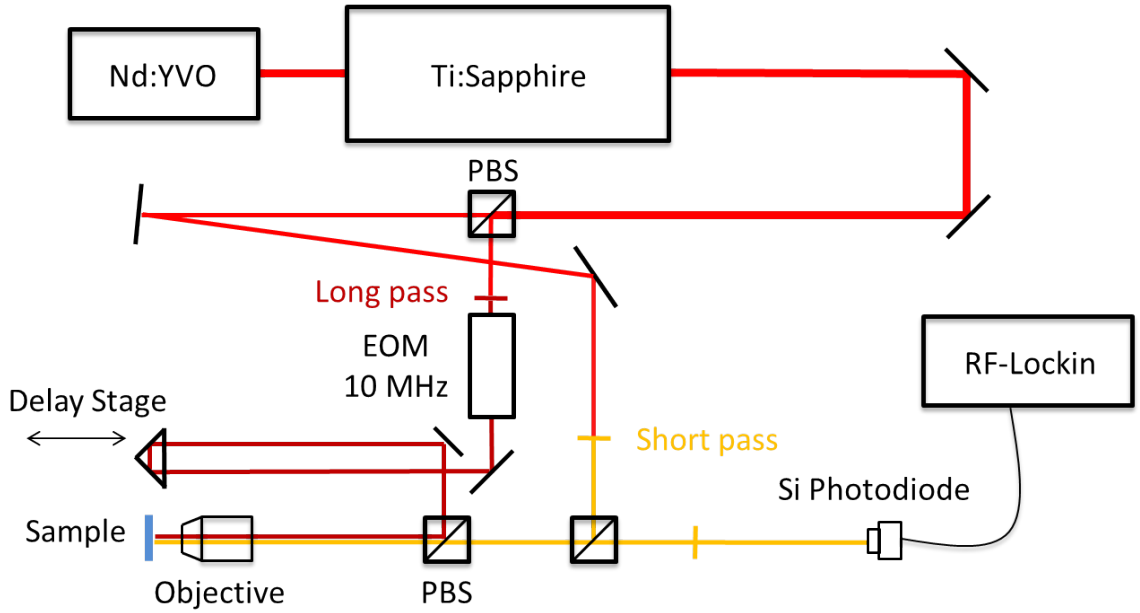

Figure 2.1: The schematic of optical pump-probe setup used in the experiments. The laser is separated into pump and probe by a polarizing beam spliter (PBS). The pump beam goes through the long pass filter, EOM, delay stage, and is focused on sample surface by objective lens. The probe beam goes through a chopper (not shown), short pass filter, and is focused on sample by the same objective lens. The probe beam is then reflected by the sample into the Si photodiode. The signal of Si photodiode is fed into a RF lock-in amplifier.

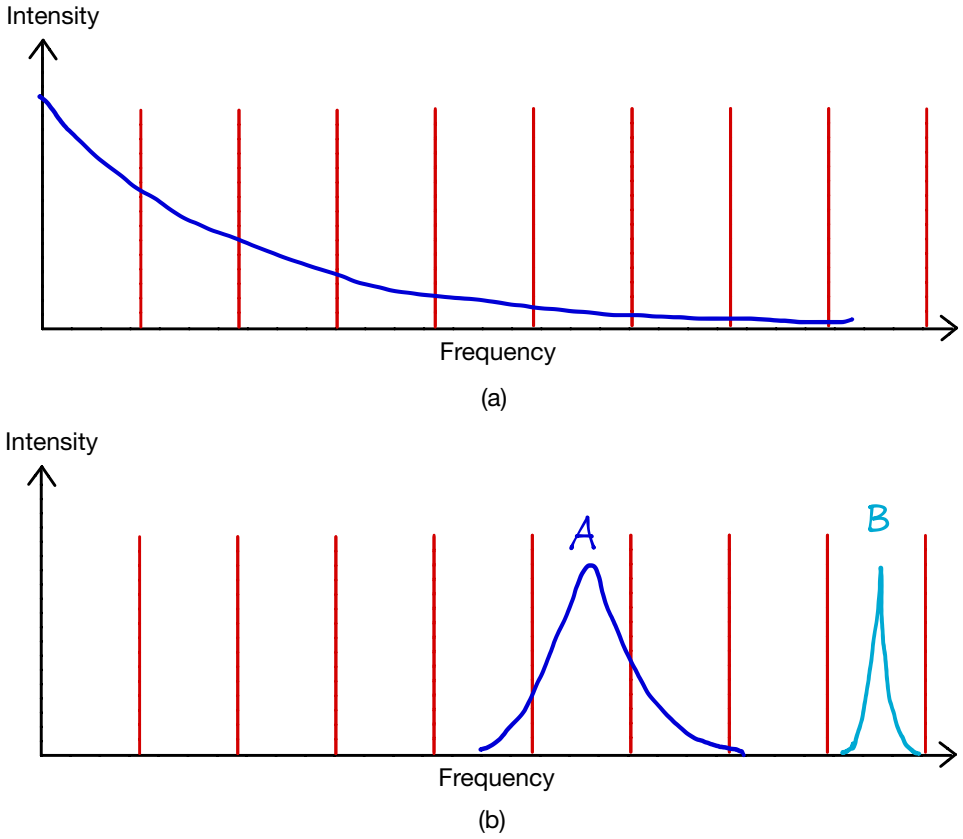

Figure 2.2: Schematic of the excitation of pump pulses in frequency domain. (a) the blue line represents the response of a thermal system which spans over all frequencies. The response components that are excited are the components overlapped with the periodic delta function. (b) the blue line represents the response of a mechanical oscillation system which centred at a particular frequency. The responses of system B excited by pump beams are small.

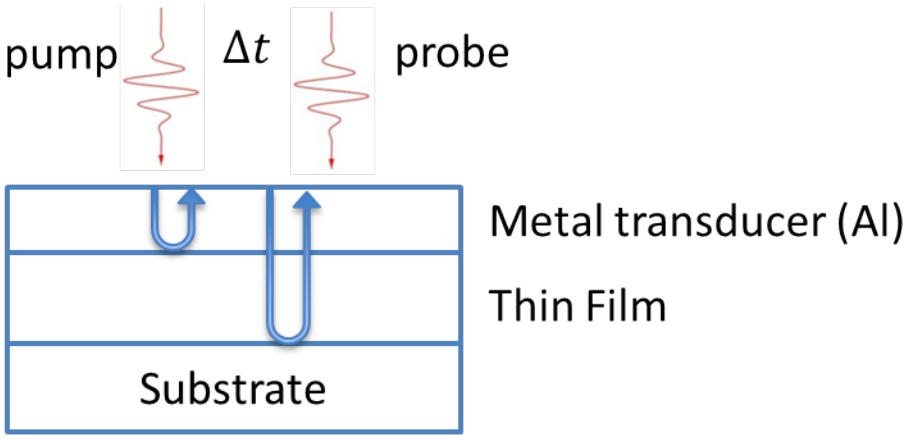

Figure 2.3: Schematic of the longitudinal acoustic echo measurement. In the measurement, pump and probe beams are overlapped, unlike what looks like in the figure. It is presented in this way for clarity.

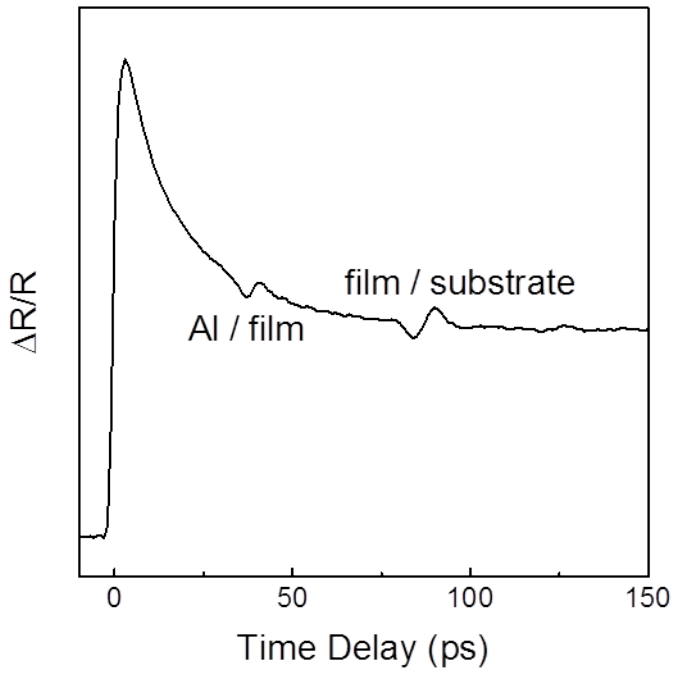

Figure 2.4: The typical signal in the longitudinal acoustic echo measurement. The echos are assigned to each interfaces

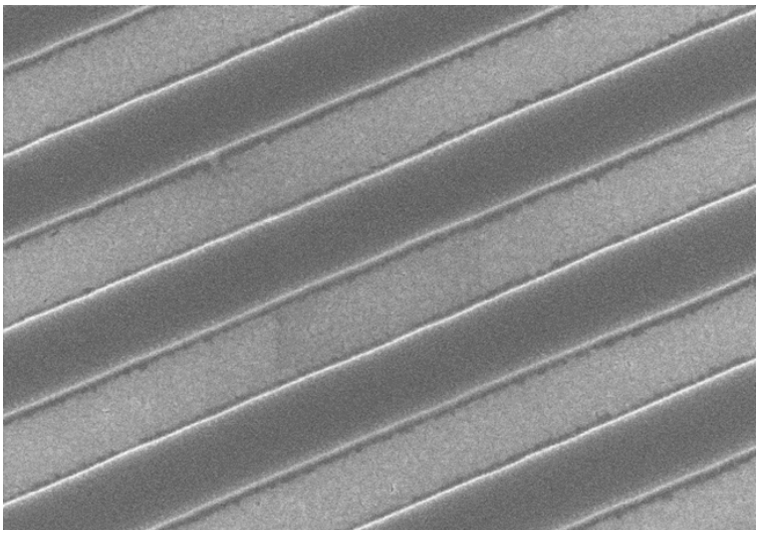

Figure 2.5: SEM image of the sample after RIE of the region with thin SU8. The bright region is the exposed Al. The dark region is the remaining SU8.

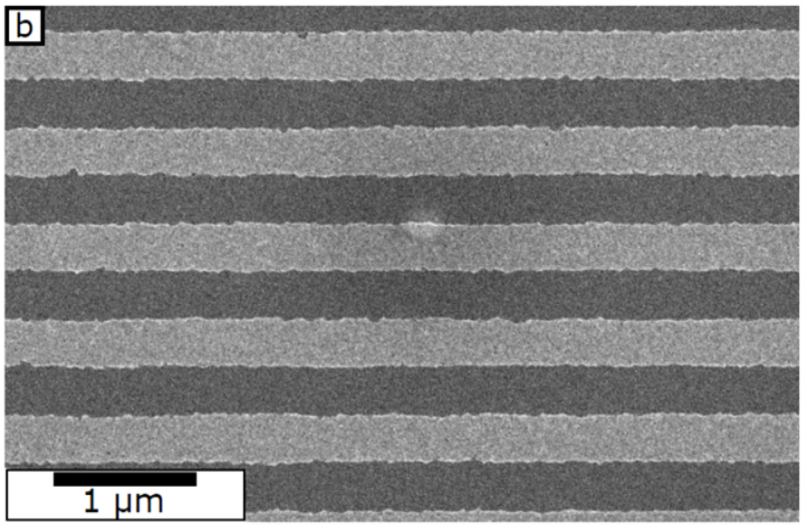

Figure 2.6: SEM image of the final Al grating pattern. The bright region is Al. The dark region is exposed Si substrate.

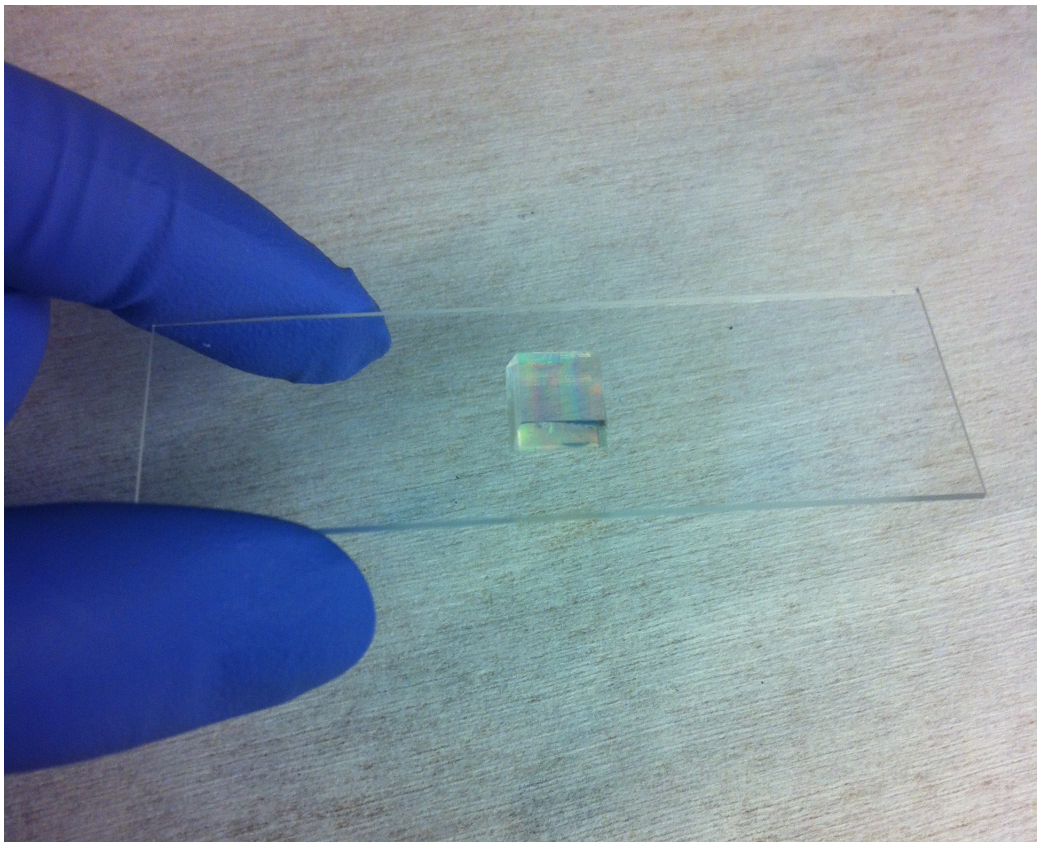

Figure 2.7: The hard PDMS stamp I use in nano-imprint lithography. The glass slide is for easy handling. The bottom of the stamp is cut to be larger than the top side intentionally, for identification as well as easy handling.

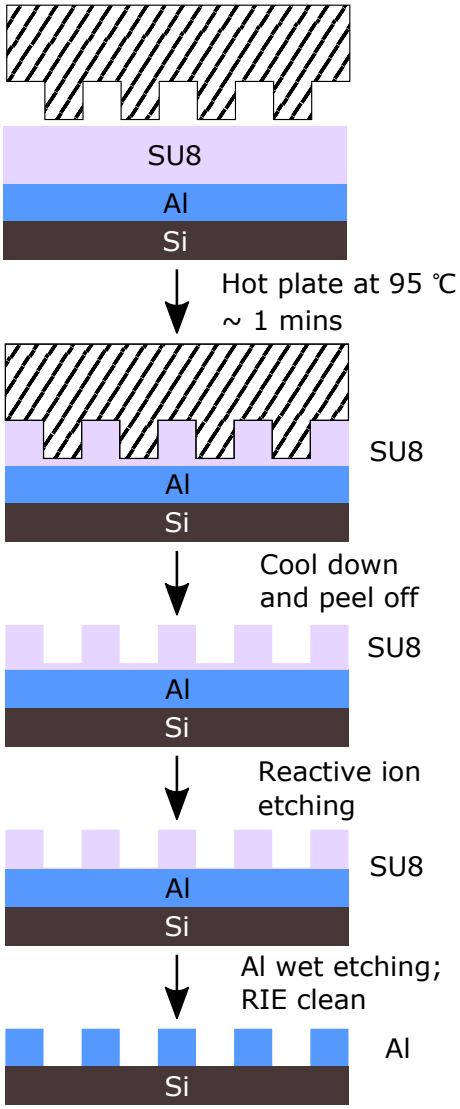

Figure 2.8: Process flow diagram for the fabrication of Al gratings using nano-imprint lithography.

CHAPTER 3

THEORY AND CALCULATION OF SURFACE ACOUSTIC WAVE AND ITS IMPLEMENTATION

Although longitudinal and shear bulk acoustic wave is relatively easy for people to understand and picture in mind, the concept of SAW is not straightforward and intuitive, as mentioned in the introduction. I think this is partly because SAW is a complicated combination of different acoustic eigenmodes. It differs from any bulk acoustic wave we are familiar with and it also differs from the water surface waves that are common in daily life.

For SAW to be used as a quantitative measurement technique, a full and detailed understanding of SAW properties are needed, such as its velocity, motion, stress distribution, strain distribution, and energy. A rigorous mathematical treatment of the problem is necessary. Surprisingly, I didn't find a easy-to-use and complete calculation software to calculate SAW of a multilayer structure composed of anisotropic materials. A finite element calculation is not convenient and have limited help to physical understandings. In this chapter, I lay out the details of the mathematical derivations involved in SAW and my implementation of the calculation. The calculation method can also be used in calculations of various other acoustic modes. The purpose is to help anyone who wants to have a deep understanding of SAW and wants to modify or improve my implementation of calculation.

The theory in this chapter and later in Chapter 7 involves a lot of computation between vectors and tensors. In these derivations, I typically use $i, j, k, ...$ to represent the Cartesian coordinates 1, 2, and 3, unless specified otherwise. I use the form of x_i to represent a vector, x_{ij} to represent a second order tensor, and so on (they can also be regarded as individual component with no confusion). The arithmetic between vectors and tensors will be written in the form like $x_i = F_{ij}a_j$ and the Einstein summation notation is always implied, i.e., summation over all the values of the repeated index.

From my personal experience, the linear algebra involved in the theory can be challenging initially, for example the fourth rank tensor elastic

constant: c_{ijkl}. It may not be necessary to assign everything a physically meaning immediately. Some concept can be initially treated just as a set of parameters from the point of view of mathematics. And as the derivation proceeds, the physically meaning can manifest itself later. As for the difficulties of the math involved, I will have to quote John von Neumann's response to Felix Smith: "Young man, in mathematics you don't understand things. You just get used to them." So after writing down these equations and derivations again and again, I finally felt like I understood them.

3.1 Solid mechanics and bulk acoustics wave

Continuum mechanics or solid mechanics is very wide subject that is studied by people in areas of mechanics, civil engineering, and materials science, to only name a few. People in different area of expertises have different focus and can often use different names and descriptions for the same concept. Because of this, it's difficult to find one book that is perfect for the scope of this study. It's not in the purpose of this section to give the reader a complete review of the subject of solid mechanics. I only want to summarize and even simplify (based on my understanding) the necessary concept that is needed for the calculation of SAW, in order to help people who don't want to or don't have the time to delve into the huge books of solid mechanics. In Chapter 7, I revisit some of the same concepts from a slightly different point of view in order to understand the theory behind the third order elastic constants.

I start from the concept of stress and strain. For a continuum, the material within can be subject to two kinds of force, body force and traction. Consider a small region $\mathcal{P}$ with boundary $\mathcal{D}$ inside the solid, the body force acts at each point of the interior of $\mathcal{P}$, which is force per unit volume. The traction acts on the boundary $\mathcal{D}$ and has the unit of force per unit area. A very common body force is the gravity.

If the body force is homogeneous across the whole solids, like gravity, it can be omitted, since we are interested in the relative motion of particles within the solids. We are more interested in the force applied on a certain plane within the solid. The way to describe the traction is to use the *stress tensor* σ_{ij}, where $i, j = 1,\ 2,\ 3$ are the Cartesian coordinates. The stress

tensor is constructed so that the traction T_i applied on a material plane with normal vector n_j can be calculated as:

$$T_i = n_j \sigma_{ij} \tag{3.1}$$

which is sometimes called the Cauchy's Theorem. σ_{ij} is also called the Cauchy stress tensor, to distinguish with the other stress tensors that are introduced in Chapter 7. σ_{ij} is a 3×3 tensor. The physical meaning of σ_{ij} is that its the stress acting on the plane perpendicular to axis i and pointing at direction j. A very important property of σ_{ij} is it's symmetric $\sigma_{ij} = \sigma_{ji}$. The real symmetric tensor σ_{ij} can always be diagonalized and the diagonals are the principle stresses. The principle stresses are very important in many different analysis but not in the current case. The symmetric property in stress tensor helps the simplification of stress-strain relation which is described shortly.

Strain describes the change of the length of a certain material component under deformation. In acoustic wave, the deformation of the material is very small. Under this condition, the strain η_{ij} can be defined as:

$$\eta_{ij} = \frac{1}{2}\left(\frac{\partial u_i}{\partial x_j} + \frac{\partial u_j}{\partial x_i}\right) \tag{3.2}$$

where u_i is the displacement vector of the particle in solid which is very small, and x_i is the Cartesian coordinate. Here η_{ij} is also a 3×3 tensor and sometimes called the Lagrangian strain tensor. The full derivation of Lagrangian tensor is introduced in Chapter 7. Here the acoustic wave under discussion is within a undeformed material and the above definition is enough for the strain generated by the acoustic wave. It is obvious from the definition that the strain tensor is also symmetric.

Since the deformation in acoustic wave is very small, the material is assumed to be always in the elastic regime, i.e. the stress is linear with respect to the deformation which is the famous Hook's Law. This set of coefficients is the second order elastic constants. Notice that this set of coefficients connects two 3×3 tensor. So the coefficient needs to be a $3 \times 3 \times 3 \times 3$ tensor to establish the linear relationship:

$$\sigma_{ij} = c_{ijkl}\eta_{kl} \tag{3.3}$$

The inverse relationship is captured by the compliance tensor s_{ijkl} which is the inverse of the c_{ijkl}. Compliance tensor can be convenience and useful in some stress-strain experiments. But it won't be used and discussed in the current context.

The full fourth-rank tensor c_{ijkl} contains 81 components. After considering the symmetry in η_{ij} and σ_{ij}, it can be shown that c_{ijkl} contain the following symmetry:

$$c_{ijkl} = c_{ijlk} = c_{jikl} = c_{jilk} = c_{klij} = ...$$

This can lead to great simplification in the notation. A most commonly used notation is to convert the index:

$$11 \to 1,\ 22 \to 2,\ 33 \to 3,\ 23 \to 4,\ 13 \to 5,\ 12 \to 6.$$

This conversion is not intuitive and I wrote it down on a sticky note and stuck it on the wall right besides me in my first two years. This index conversion is applied to stress, strain, and elastic constant to write down the Hooke's Law in a simplified manner:

$$\sigma_m = c_{mn}\eta_n,\ m, n = 1, 2, 3, 4, 5, 6 \tag{3.4}$$

There is an subtle but important point involved in the conversion: both stress and elastic constant can be converted directly as $\sigma_{ij} \to \sigma_n$ and $c_{ijkl} \to c_{mn}$ based on the conversion rule above; but for strain the conversion is slightly different: $\eta_{ii} \to \eta_n$ and $\eta_{ij} \to 0.5\eta_n$ for $i \neq j$. The extra coefficient in components of shear strain is from the direct comparison between the original equation and simplified equation. η_m with $m = 1...6$ is called the engineering strain. The difference in shear components between Lagrangian strain and engineering strain needs extra attention. Although through the thesis c_{mn} is commonly used, I only use Cauchy stress σ_{ij} and Lagrangian strain η_{ij} to avoid any potential confusion and mistakes.

The simplified elastic constant tensor c_{mn} has 36 components. Since it is also symmetric, it only has 21 independent element. It can be further simplified using the symmetry of crystal lattice. For isotropic crystal, there are only two independent elastic constants c_{11} and c_{44}; for cubic crystal, there are three independent elastic constants c_{11}, c_{12}, and c_{44}; for hexagonal crystal,

there are five independent elastic constants c_{11}, c_{12}, c_{13}, c_{33}, and c_{44}. The following is the elastic constant c_{ij} of a isotropic crystal and cubic crystal:

$$c_{ij} = \begin{bmatrix} c_{11} & c_{12} & c_{12} & 0 & 0 & 0 \\ c_{12} & c_{11} & c_{12} & 0 & 0 & 0 \\ c_{12} & c_{12} & c_{11} & 0 & 0 & 0 \\ 0 & 0 & 0 & c_{44} & 0 & 0 \\ 0 & 0 & 0 & 0 & c_{44} & 0 \\ 0 & 0 & 0 & 0 & 0 & c_{44} \end{bmatrix}$$

The difference is that in isotropic crystal, there exists the relation: $c_{44} = (c_{11} - c_{12})/2$. But this relationship no longer holds in cubic crystal.

To obtain the equation of motion of bulk acoustic waves, we consider the variation of stress across an infinitesimal parallelepiped with its three edge parallel to the Cartesian coordinates axes. The motion of this infinitesimal material element is determined by the net force applied on it, which is the summation of all stress on the boundaries. For example, the force acting in the x_1 direction is:

$$\begin{aligned}(\sigma_{11} + \frac{\partial \sigma_{11}}{\partial x_1}\,\mathrm{d}x_1)\,\mathrm{d}x_2\,\mathrm{d}x_3 - \sigma_{11}\,\mathrm{d}x_2\,\mathrm{d}x_3 + (\sigma_{12} + \frac{\partial \sigma_{12}}{\partial x_2}\,\mathrm{d}x_2)\,\mathrm{d}x_1\,\mathrm{d}x_3 - \sigma_{12}\,\mathrm{d}x_1\,\mathrm{d}x_3 \\ +(\sigma_{11} + \frac{\partial \sigma_{11}}{\partial x_1})\,\mathrm{d}x_2\,\mathrm{d}x_3 - \sigma_{11}\,\mathrm{d}x_2\,\mathrm{d}x_3 = (\frac{\partial \sigma_{11}}{\partial x_1} + \frac{\partial \sigma_{12}}{\partial x_2} + \frac{\partial \sigma_{13}}{\partial x_3})\,\mathrm{d}x_1\,\mathrm{d}x_2\,\mathrm{d}x_3\end{aligned} \tag{3.5}$$

According to the Newton's second law, one can write down the equation of motion:

$$\rho \frac{\partial^2 u_i}{\partial t^2} = \frac{\partial \sigma_{ij}}{\partial x_j} \tag{3.6}$$

Utilizing Hooke's Law and the relationship between Lagrangian strain and displacement, we convert the equation of motion to be:

$$\rho \frac{\partial^2 u_i}{\partial t^2} = c_{ijkl} \frac{\partial \eta_{kl}}{\partial x_j} = c_{ijkl} \frac{\partial^2 u_k}{\partial x_l \partial x_j} \tag{3.7}$$

Now the equation of motion becomes a partial differential equation about the displacement of the particles which is exactly what we want.

To solve this partial differential equation without any boundary condition, we can find the plane wave solution, or the general solution by assuming

Table 3.1: Velocity of bulk acoustic wave at high symmetry direction in cubic crystal

Mode	parameter c
$\langle 100 \rangle$ Transverse	$c = c_{44}$
$\langle 100 \rangle$ Longitudinal	$c = c_{11}$
$\langle 111 \rangle$ Transverse	$c = \frac{1}{3}(c_{11} - c_{12} + c_{44})$
$\langle 111 \rangle$ Longitudinal	$c = \frac{1}{3}(c_{11} + 2c_{12} + 4c_{44})$
$\langle 110 \rangle$ Transverse,polarization $\langle 001 \rangle$	$c = c_{44}$
$\langle 110 \rangle$ Transverse,polarization $\langle 1\bar{1}0 \rangle$	$c = \frac{1}{2}(c_{11} - c_{12})$
$\langle 110 \rangle$ Longitudinal	$c = \frac{1}{2}(c_{11} + c_{12} + 2c_{44})$

$u_i = U_i \exp[i(k_j x_j - \omega t)]$, where U_i is the amplitude of the wave (assuming unit length), k_j is the wave vector and ω is the angular frequency of the wave. By inserting the plane wave solution back to the equation of motion, one reaches the famous Christoffel equation:

$$(c_{ijkl} k_j k_l - \rho\omega^2 \delta_{ik}) U_k = 0 \tag{3.8}$$

The physical meaning of the Christoffel equation is: for wave with wave vector k_i, which specifies both wavelength and direction, the angular frequency of the acoustic wave is ω and $\rho\omega^2$ is the eigenvalue of the Cristoffel matrix $\Gamma_{ik} \equiv c_{ijkl} k_j k_l$. Since Γ_{ij} is a 3×3 tensor, it has three eigenvalues corresponding to three acoustic modes at certain direction. The three acoustic modes contain one quasi-longitudinal wave and two quasi-transverse acoustic wave. The reason that they are "quasi" is because in general the amplitude of the wave may not have pure longitudinal or transverse relation with respect to the propagation direction. For crystal with high symmetry, at certain high symmetry directions, the Christoffel equation becomes simple and the speed of sound at these directions can be easily calculated. These relationships can be convenient if remembered or documented. Here I list the speed of sound at high symmetry directions in cubic crystal with three independent elastic constants c_{11}, c_{12}, and c_{44}. The velocity of acoustic waves can be written in the form of $v = \sqrt{c/\rho}$ where c is a certain combination of elastic constants and ρ is the density. c of cubic crystal at certain high symmetry direction can be found in the Table. 3.1:

For isotropic material, one can replace $(c_{11} - c_{12})/2$ by c_{44} and Table 3.1 can be used for isotropic material. Table 3.1 also assigns physical meanings

to the elastic constants in the sense that it conjugate elastic constants with acoustic mode. For example, c_{11} corresponds to the bulk acoustic wave so it can be viewed as the longitudinal elastic constant; c_{44} and $(c_{11} - c_{12})/2$ correspond to transverse acoustic wave and they can be viewed as shear elastic constant. Actually $(c_{11} - c_{12})/2$ of a cubic crystal has a specific name which is the tetragonal shear elastic constant. In isotropic material, $c_{44} = (c_{11} - c_{12})/2$. The difference between c_{44} and $(c_{11} - c_{12})/2$ can be viewed as a parameter representing the degree of anisotropy of cubic crystals. $r = 2c_{44}/(c_{11} - c_{12})$ can be defined as the anisotropy of cubic crystal. When $r = 1$, it is isotropic. The material is more anisotropic as r deviates more from 1.

The relationship between elastic constants c_{mn} and speed of sound like Table. 3.1 is also the reason that in acoustic community people prefer to use elastic constants instead of compliance matrix s_{mn} and other parameters like Young's modulus and Poisson's ratio.

3.2 Calculation of surface acoustic wave of half-space using Green's function method

From a general point of view, there is nothing special about SAW in the sense that, just like bulk acoustic wave, SAW is the motion of solid and it is still governed by the equation of motion Eq. 3.7. But SAW is no longer a general solution to the partial differential equation Eq. 3.7 but a special solution because (at least) one boundary condition is applied: the free surface. So solving SAW becomes a typical problem of solving partial differential equations with boundary conditions.

Unfortunately, there is no analytical solution to the SAW like the solutions the bulk acoustic wave in Table. 3.1. Even for the easiest case, the isotropic material, one can at best reach to a non-linear equation. So numerical solution is absolutely necessary. This fact possibly posed difficulties for early researchers who studied SAW initially. Powerful computers and algorithms weren't available at that time.

Although we have much more powerful computers now, we still need to pay attention to the difficulties from the fact that this is in the end a numerical solution. As discussed later, since the free boundary condition means no stress on the surface, in the end a numerical problem appears:

what is numerically zero in the calculation? This is especially problematic when the structure is complicated (layered), and multiple modes can exist. Then it's hard to distinguish between different modes and make sure that all solutions are found. For example in the paper by Lim and Farnell [29] about the "forbidden directions" of SAW in anisotropic crystals, the authors had to carefully exam all possible solutions and tried to develop a algorithmic process to successfully find all proper solutions numerically.

This is when the Green's function method becomes useful. Green's function is used in many fields and people may have slightly different definition of it. Here I briefly summarize how it is used in the current problem and its physical interpretation.

Mathematically, the Green's function method means that the boundary conditions are not homogeneous boundary conditions, but have a delta function at time zero. Physically, I prefer to understand Green's function method as a "excitation-response" method, very similar with the response theory discussed in Chapter 2. The delta function applied initially is the excitation to the system and the solution is the response of the system to this particular excitation. The delta excitation is usually a delta function in both time domain and spatial domain. So this excitation is capable of exciting all possible modes at all frequency and wave vector. Also one can directly compare the amplitude of the response of each mode to tell whether a mode is relatively strong or weak comparing with other modes. Another advantage is that the excitation can be tailored to fit a particular requirement or experimental setup. For example, one can apply excitation only at perpendicular direction or only at parallel direction by setting the vector components of the delta boundary condition. One can also put the excitation at an interface instead of a surface to test the possible interface acoustic mode. This generalization is discussed at the end of this chapter. All these advantages are possible due to the Green's function method. It makes the calculation a much more general and flexible tool.

In this section I describe how to calculate SAW of a half-space. In the later sections, I describe how to calculate more complicated structure based on the method presented here. A brief discussion of the use of Green's function method to calculate SAW can be found in Ref. [30].

3.2.1 SAW of half-space

I start with the calculation of a half-space (bare substrate). For any acoustic waves, the displacement $\bar{U} = [U_1, U_2, U_3]$ satisfies the equation (adopts Einstein summation notation):

$$c_{ijkl}\frac{\partial^2 U_k}{\partial x_j \partial x_l} = \rho\frac{\partial^2 U_i}{\partial t^2}, \quad i,j,k,l = 1,2,3 \tag{3.9}$$

where c_{ijkl} is the elastic constant tensor of the half-space, U_i is the displacement at i direction, and ρ is density of substrate.

Again, the first step to solve the partial differential equation is to find the general solution. Eq. 3.9 admits plane wave solution of:

$$U_i = \tilde{U}_i exp[i(\bar{k}\cdot\bar{x} - \omega t)] \tag{3.10}$$

where $\tilde{U}_i$ is the unit polarization vector; $\bar{k} = 2\pi\bar{n}/\lambda$ is the wave vector; λ is the wavelength and $\bar{n}$ is the wave normal. Putting Eq. 3.10 back to Eq. 3.9 gives the famous Christoffel equation:

$$\Gamma_{ik}\tilde{U}_k \equiv C_{ijkl}k_j k_l \tilde{U}_k = \rho\omega^2\tilde{U}_i \tag{3.11}$$

Γ_{ik} is defined as the Cristoffel matrix. For the eigenvalue problem of the 3×3 Cristoffel matrix to have solution, $\bar{k}$ and ω should have the relationship:

$$det(\Gamma_{ik} - \rho\omega^2\delta_{ik}) = 0 \tag{3.12}$$

For SAW with wave vector $\mathbf{k}_\parallel = (k_1, k_2)$ and propagating on (x_1, x_2) plane, the displacement U_i satisfies Eq. 3.9. U_i can be written in Fourier space of $(\omega, \bar{k}_\parallel)$:

$$U_i(\bar{x}, t) = \int_{-\infty}^{\infty} d\bar{k}_\parallel \int_{-\infty}^{\infty} d\omega\, u_i(\bar{k}_\parallel, x_3, \omega) e^{i(\bar{k}_\parallel\cdot\bar{x}_\parallel - \omega t)} \tag{3.13}$$

With given ω and (k_1, k_2), Eq. 3.12 can be solved to give 6 $k_3^{(n)}$ (possible complex numbers) and 6 corresponding eigenvectors $\alpha_i^{(n)}$ with the superscript (n) ranging from 1 to 6. According to linear algebra, they are components of SAW with ω and (k_1, k_2). SAW should not have wave components that come from substrate or with higher energy when deeper into substrate. This

selection rule eliminates three $k_3^{(n)}$ and corresponding $\alpha_i^{(n)}$. With the three solutions left, the Fourier kernel in Eq. 3.13 can be written as:

$$u_i(\bar{k}_\parallel, x_3, \omega) = \sum_{n=1}^{3} A^{(n)} \alpha_i^{(n)} e^{ik_3^{(n)} x_3} \tag{3.14}$$

where $A^{(n)}$ are three coefficients of the linear combination of three wave components. They are the only unknowns.

The boundary conditions are applied next to solve the coefficients $A^{(n)}$. The boundary condition at surface $x_3 = 0$ is point excitation:

$$\sigma_{l3}(\bar{x}_\parallel, x_3 = 0, t) = C_{l3pq} \frac{\partial U_p(\bar{x}_\parallel, x_3 = 0, t)}{\partial x_q} = \delta_{l3} \delta(\bar{x}_\parallel) \delta(t) \tag{3.15}$$

which can be written in Fourier space as:

$$\delta_{l3} \delta(\bar{x}_\parallel) \delta(t) = \delta_{l3} \frac{1}{(2\pi)^2} \int_{-\infty}^{\infty} d\bar{k}_\parallel \int_{-\infty}^{\infty} d\omega \, e^{i(\bar{k}_\parallel \bar{x}_\parallel - \omega t)} \tag{3.16}$$

Applying Eqs. 3.13, 3.14 and 3.16 into Eq. 3.15, we have:

$$\sum_{n=1}^{3} i C_{l3pq} k_q^{(n)} \alpha_p^{(n)} A^{(n)} = \delta_{l3} \tag{3.17a}$$

$$k_1^{(n)} = k_1, \; k_2^{(n)} = k_2 \tag{3.17b}$$

We can define the 3×3 matrix $B_l^{(n)} = i C_{l3pq} k_q^{(n)} \alpha_p^{(n)}$ and solve the equation $B_l^{(n)} A^{(n)} = \delta_{l3}$ to get all three $A^{(n)}$. Putting $A^{(n)}$ back to Eq. 3.14 gives $\bar{u}(\bar{k}_\parallel, x_3, \omega)$. $\bar{u}(\bar{k}_\parallel, x_3 = 0, \omega)$ is the third column (because the excitation applied here is only at direction 3) of the surface elastodynamic Green's function in Fourier space G_{ij}, thus $G_{33} = u_3(\bar{k}_\parallel, x_3 = 0, \omega)$ is obtained. $G_{33}(\bar{k}_\parallel, x_3 = 0, \omega)$ can be mapped in $(k_\parallel, \omega)$ space (for one particular $\bar{k}_\parallel$ direction) and its extreme points define the dispersion curve. For example, the Fig. 3.1, Fig. 6.4a and Fig. 6.4c are the color maps of G_{33}. Fig. 3.2, Fig. 3.5 is from the extreme points of G_{33}.

3.2.2 Surface acoustic wave in crystal with high symmetry propagating at high symmetry direction

Although there is no analytical solution to the problem, for crystal with certain symmetry and SAW propagating at certain direction, one can obtain a non-linear equation. This can be useful in certain cases. I refer interested readers to Ref. [6, 31].

3.2.3 Example of calculation: Si

I use half-space of Si as an example to demonstrate the result of calculation described before. These detailed calculation about Si is also used in Chapter 6.

Consider SAW on the Si (001) plane propagating at different directions. Fig 3.1 shows the color map of G_{33} in the Fourier (ω and $k_{\|}$) space. Fig. 3.2 is the extreme points read from the color map, which represents the dispersion curve. From a particular point (ω, k) on the dispersion curve, one can calculate $v_{SAW} = \omega/k$ for the particular wavevector k. This calculation is done for different directions on the (001) plane and Fig 3.3 is obtained. Fig. 3.3 shows that after a certain angle, SAW degenerates into the bulk shear acoustic wave and another mode of SAW, the so-called pseudo surface acoustic wave (PSAW) rises. Farnell [7] discussed this behavior extensively. With the coefficient of linear combination, stress, strain, and displacement at different depth can be calculated using the definition and relationship described in last section. Fig 3.4 shows the strain energy in SAW at different depth. The figure shows that SAW is mostly a shear wave. The detailed derivation of strain energy is discussed in Chapter 6.

3.3 Surface acoustic wave of multilayer structure

Calculation of SAW on a half-space is the foundation of further calculations. From last section, we can see that the calculation at its essence is solving partial differential equations with boundary conditions. As the problem becomes more complicated, the principle and general procedure don't change: find the eigenmodes (general solutions, corresponds to bulk acoustic waves)

of Cristoffel equations; the specific solution to the problem is the linear combination of the general solutions so that it satisfies the specific boundary conditions. The linear algebraic equations are formulated by the boundary conditions.

When the structure contains multilayers, material of each layer has its own Cristoffel equation, eigenmodes, and eigenvectors. The boundary is no longer just surface, but also each interface between layers. The boundary conditions at each interface are: continuity of stress and continuity of displacement. Similar to the treatment in last section, stress and strain are expressed at both side of the boundary and the linear equations are construct through the continuity.

Consider a layered structure with M layers, with layer M as the substrate and layer 1 as surface layer. The free surface of layer 1 locates at $x_3 = 0$ and the whole structure exists at the positive side of the x_3 axis. The substrate extends to $x_3 \to +\infty$. This coordinate system is not natural but it is convenient for the calculation. Keep in mind that the materials exist at the positive half of the space. Omission of this can lead to mistakes (as I did once). Next each boundary condition are considered and the notations are consistent with last section and everything is written in Fourier space.

3.3.1 Surface located at $x_3 = 0$

At top surface, only layer 1 is relevant, and the boundary condition is similar to the boundary condition of the half-space case, i.e. continuity of stress with the delta excitation:

$$i \sum_{n=1}^{6} A(1)^{(n)} C(1)_{3lpq} u(1)_p^{(n)} k(1)_q^{(n)} = \delta_{l3} \tag{3.18}$$

where $A(1)$, $C(1)$, $u(1)$, and $k(1)$ are the coefficient, elastic constants, eigenvectors, and wave vectors of layer 1. The top coefficient (n) identifies each eigensolution of the Cristoffel equation in layer 1. This boundary condition can be written in the form of dot product between matrix and linear

coefficient as:

$$\begin{pmatrix} Stress(1)Down \end{pmatrix}_{3\times 6} \cdot \begin{pmatrix} A(1) \end{pmatrix}_{6\times 1} = \begin{pmatrix} 0 \\ 0 \\ 1 \end{pmatrix}$$

with the matrix $Stress(1)Down$ as $C(1)_{3lpq}u(1)_p^{(n)}k(1)_q^{(n)}$. Note both p and q are summed over and the index left is l which ranges from 1 to 3, and n which ranges from 1 to 6. The footnote of each matrix is the size of the matrix. This matrix form helps the implementation later in `MatLab` or `Python` (using `Numpy` which is optimized for linear algebraic calculation).

3.3.2 Interface located at $x_3 = d_1$ between layer 1 and layer 2

The continuity of stress can be written as:

$$\begin{aligned} & i\sum_{n=1}^{6} A(1)^{(n)}C(1)_{3lpq}u(1)_p^{(n)}k(1)_q^{(n)}\exp(ik(1)_3^{(n)}d_1) \\ = & i\sum_{n=1}^{6} A(2)^{(n)}C(2)_{3lpq}u(2)_p^{(n)}k(2)_q^{(n)}\exp(ik(2)_3^{(n)}d_1) \end{aligned} \tag{3.19}$$

Notice that the difference with the boundary condition at surface is that the phase term $\exp(ik_3x_3)$ is no longer 1 at finite depth. The continuity of displacement at direction i can be written as:

$$\sum_{n=1}^{6} A(1)^{(n)}u(1)_i^{(n)}\exp(ik(1)_3^{(n)}d_1) = \sum_{n=1}^{6} A(2)^{(n)}u(2)_i^{(n)}\exp(ik(2)_3^{(n)}d_1) \tag{3.20}$$

These two can be written in matrix form as:

$$\begin{pmatrix} Stress(1)Up \end{pmatrix}_{3\times 6} \cdot \begin{pmatrix} A(1) \end{pmatrix}_{6\times 1} = \begin{pmatrix} Stress(2)Down \end{pmatrix}_{3\times 6} \cdot \begin{pmatrix} A(2) \end{pmatrix}_{6\times 1}$$

$$\begin{pmatrix} U(1)Up \end{pmatrix}_{3\times 6} \cdot \begin{pmatrix} A(1) \end{pmatrix}_{6\times 1} = \begin{pmatrix} U(2)Down \end{pmatrix}_{3\times 6} \cdot \begin{pmatrix} A(2) \end{pmatrix}_{6\times 1}$$

3.3.3 Interface located at $x_3 = d_m$ between layer m and $m+1$

Generalize the equation between layer 1 and 2, one can obtain the matrix form for interface located at $x_3 = d_m$:

$$\begin{pmatrix} Stress(\alpha)Up \end{pmatrix}_{3\times 6} \cdot \begin{pmatrix} A(\alpha) \end{pmatrix}_{6\times 1} = \begin{pmatrix} Stress(\alpha+1)Down \end{pmatrix}_{3\times 6} \cdot \begin{pmatrix} A(\alpha+1) \end{pmatrix}_{6\times 1}$$

$$\begin{pmatrix} U(\alpha)Up \end{pmatrix}_{3\times 6} \cdot \begin{pmatrix} A(\alpha) \end{pmatrix}_{6\times 1} = \begin{pmatrix} U(\alpha+1)Down \end{pmatrix}_{3\times 6} \cdot \begin{pmatrix} A(\alpha+1) \end{pmatrix}_{6\times 1}$$

with:

$$Stress(\alpha)Up_{(l,n)} = C(\alpha)_{3lpq} u(\alpha)_p^{(n)} \exp[ik(\alpha)_3^{(n)} d_\alpha] \tag{3.21}$$

$$Stress(\alpha+1)Up_{(l,n)} = C(\alpha+1)_{3lpq} u(\alpha+1)_p^{(n)} \exp[ik(\alpha+1)_3^{(n)} d_\alpha] \tag{3.22}$$

$$U(\alpha)Up_{(i,n)} = u(\alpha)_i^{(n)} \exp[ik(\alpha)_3^{(n)} d_\alpha] \tag{3.23}$$

$$U(\alpha+1)Up_{(i,n)} = u(\alpha+1)_i^{(n)} \exp[ik(\alpha+1)_3^{(n)} d_\alpha] \tag{3.24}$$

3.3.4 Interface located at $x_3 = d_{M-1}$ between layer $M-1$ and substrate layer M

Recall that at substrate layer M, only three eigenvalues and eigenvectors are picked to form the general solution (This can also be viewed as a kind of boundary condition). So the last boundary condition can be written as:

$$\begin{pmatrix} Stress(M-1)Up \end{pmatrix}_{3\times 6} \cdot \begin{pmatrix} A(M-1) \end{pmatrix}_{6\times 1} = \begin{pmatrix} Stress(M)Down \end{pmatrix}_{3\times 3} \cdot \begin{pmatrix} A(M) \end{pmatrix}_{3\times 1}$$

$$\begin{pmatrix} U(M-1)Up \end{pmatrix}_{3\times 6} \cdot \begin{pmatrix} A(M-1) \end{pmatrix}_{6\times 1} = \begin{pmatrix} U(M)Down \end{pmatrix}_{3\times 3} \cdot \begin{pmatrix} A(M) \end{pmatrix}_{3\times 1}$$

3.3.5 Summary

The matrix formation can be simplified by defining:

$$Down_1 = Stress(1)Down_{(3\times6)}$$

$$UP_\alpha = \begin{pmatrix} Stress(\alpha)Up \\ U(\alpha)Up \end{pmatrix}_{6\times6}$$

$$Down_\alpha = \begin{pmatrix} Stress(\alpha)Down \\ U(\alpha)Down \end{pmatrix}_{6\times6}$$

So we can list all the boundary conditions:

$$UP_{M-1} \cdot A_{M-1} = DOWN_M \cdot A_M$$

$$UP_{M-2} \cdot A_{M-2} = DOWN_{M-1} \cdot A_{M-1}$$

$$...$$

$$UP_1 \cdot A_1 = DOWN_2 \cdot A_2$$

$$DOWN_1 \cdot A_1 = (0, 0, 1)^T$$

This is a set of linear algebraic equations and all coefficient A_α can be solved. With all coefficient, everything about SAW, such as stress, strain, and energy, can be calculated.

3.4 Surface acoustic wave with thin grating on surface

The existence of thin metal grating complicates the problem by changing the boundary condition at top surface. It introduces structures that are potentially impossible to calculate through analytically formulation. That's why many of the literatures calculate this case using finite element simulation. But if an assumption is posed: the metal grating is very thin in the sense that it only perturb the system as mass loading, an analytically treatment can be applied. This concept can be found in Ref. [32]. I use the same idea and applied it in the Green's function method. I start with the case when the mass loading is uniform.

3.4.1 Surface acoustic wave of half-space with uniform mass loading

Although we can calculate SAW of layered structure rigorously, considering the cases of uniform mass loading does have its own value. It mimics the situations when there is small amount of materials (such as molecules) deposited on the top surface. These materials may not apply stress and deformation to the substrate but they do pose a mass loading to the system. This is the cases when SAW devices are used as sensors. My estimation of thickness of condensation layer [33] uses exactly this calculation. Problem of uniform mass loading also provides foundation for the calculation of periodic mass loading.

If there is an uniform layer on top of the substrate, the boundary condition becomes:

$$\begin{aligned}\sigma_{l3}(x_\parallel, x_3=0,t) &= C_{l3pq}\frac{\partial U_p(x_\parallel, x_3=0,t)}{\partial x_q} \\ &= \delta_{l3}\delta(x_\parallel)\delta(t) + \mu\frac{\partial^2 U_l(x_\parallel, x_3=0,t)}{\partial t^2} \qquad (3.25)\end{aligned}$$

Here μ is the mass per unit area. The mass loading term in Fourier space is:

$$\begin{aligned}\mu\frac{\partial^2 U_l(x_\parallel, x_3=0,t)}{\partial t^2} &= \frac{1}{(2\pi)^2}\int_{-\infty}^{\infty} dk_\parallel \int_{-\infty}^{\infty} d\omega\, e^{i(k_\parallel x_\parallel - \omega t)}(-\mu\omega^2) \\ &\times \sum_{n=1}^{3} A^{(n)}\alpha_l^{(n)} e^{ik_3^{(n)}(\bar{k}_\parallel,\omega)x_3} \qquad (3.26) \\ k_1^{(n)} &= k_1,\ k_2^{(n)} = k_2,\ k_3^{(n)} = k_3^{(n)} \qquad (3.27)\end{aligned}$$

So the boundary condition at $x_3 = 0$ is:

$$\begin{aligned}\delta_{l3} &= \sum_{n=1}^{3} A^{(n)} iC_{l3pq}\alpha_p^{(n)}k_q^{(n)} e^{ik_3^{(n)}(\bar{k}_\parallel,\omega)x_3} - (-\mu\omega^2)\sum_{n=1}^{3} A^{(n)}\alpha_l^{(n)} e^{ik_3^{(n)}(\bar{k}_\parallel,\omega)x_3} \\ &= \sum_{n=1}^{3} A^{(n)}[iC_{l3pq}\alpha_p^{(n)}k_q^{(n)} + \mu\omega^2\alpha_l^{(n)}] \qquad (3.28)\end{aligned}$$

Using this boundary condition together with solution of Eq. 3.12, $A^{(n)}$ can be solved.

3.4.2 SAW of Substrate with Periodic Grating

Similarly, the periodic mass loading from metal grating changes the boundary condition into:

$$\begin{aligned}\sigma_{l3}(x_\parallel, x_3=0,t) &= C_{l3pq}\frac{\partial U_p(x_\parallel, x_3=0,t)}{\partial x_q} \\ &= \delta_{l3}\delta(x_\parallel)\delta(t) + \mu(x_\parallel)\frac{\partial^2 U_l(x_\parallel, x_3=0,t)}{\partial t^2} \end{aligned} \quad (3.29)$$

If $\mu(x_\parallel)$ has a periodic rectangular dependence on position (rectangular grating), its Fourier transform is:

$$\mu(x_\parallel) = \sum_{m=-\infty}^{\infty} \mu_m e^{imGx_\parallel}, \quad |\bar{G}| = \frac{2\pi}{\lambda} \quad \bar{G} = (g_1, g_2) \quad (3.30)$$

where λ is the periodicity of the grating. When $\mu(x)$ is involved in boundary conditions, it causes the mixing between components $u_i(k_\parallel + nG, x_3, \omega)$, with integer n from $-\infty$ to ∞. So we rewrite the expression of surface displacement:

$$\begin{aligned} U_i(\bar{x},t) &= \int_{-\infty}^{\infty} dk_\parallel \int_{-\infty}^{\infty} d\omega\, u_i(\bar{k}_\parallel, x_3, \omega) e^{i(k_\parallel x_\parallel - \omega t)} \\ &= \sum_{m=-\infty}^{\infty} \int_{-G/2}^{G/2} dk_\parallel \int_{-\infty}^{\infty} d\omega\, u_i(\bar{k}_\parallel + m\bar{G}, x_3, \omega) e^{i((k_\parallel + mG)x_\parallel - \omega t)} \\ &= \int_{-G/2}^{G/2} dk_\parallel \int_{-\infty}^{\infty} d\omega \sum_{m=-\infty}^{\infty} u_i(\bar{k}_\parallel + m\bar{G}, x_3, \omega) e^{i((k_\parallel + mG)x_\parallel - \omega t)} \\ &= \int_{-G/2}^{G/2} dk_\parallel \int_{-\infty}^{\infty} d\omega \sum_{m=-\infty}^{\infty} \sum_{n=1}^{3} A^{(n)(m)} \alpha_i^{(n)(m)} e^{ik_3^{(n)(m)} x_3} e^{i((k_\parallel + mG)x_\parallel - \omega t)} \end{aligned} \quad (3.31)$$

$k_3^{(n)(m)}$ and $\alpha_i^{(n)(m)}$ correspond to the $(k_\parallel + mG_\parallel)$ term of the solutions of the Cristoffel equation. Actually $\alpha_i^{(n)(m)}$ is independent with the size of $k_\parallel$; it only depends on the direction. But I still assign it to each m for the sake of programming the calculation. The similar process can be applied for the stress:

$$\begin{aligned}\delta_{l3}\delta(x_\parallel)\delta(t) &= \delta_{l3}\frac{1}{(2\pi)^2}\int_{-\infty}^{\infty}dk_\parallel\int_{-\infty}^{\infty}d\omega\, e^{i(k_\parallel x_\parallel-\omega t)} \\ &= \delta_{l3}\frac{1}{(2\pi)^2}\int_{-G/2}^{G/2}dk_\parallel\int_{-\infty}^{\infty}d\omega\ \sum_{m=-\infty}^{\infty}e^{i((k_\parallel+mG)x_\parallel-\omega t)} \quad (3.32)\end{aligned}$$

and if the excitation has Gaussian shape, it can be written in a similar form:

$$\begin{aligned}e^{-2x_\parallel^2/L^2} &= A\int_{-\infty}^{\infty}e^{-\frac{1}{8}k^2L^2}e^{ikx_\parallel}dk = A\int_{-G/2}^{G/2}dk\sum_{m=-\infty}^{\infty}e^{-\frac{1}{8}(k+mG)^2L^2}e^{i(k+mG)x_\parallel} \\ &= A\int_{-G/2}^{G/2}dk\sum_{m=-\infty}^{\infty}e^{-\frac{1}{8}(k+mG)^2L^2}e^{imGx_\parallel}e^{ikx_\parallel} \quad (3.33)\end{aligned}$$

In these integral I require $\|k_\parallel\| < G/2$. Putting all the expression into boundary condition Eq. 3.31, we have:

$$\begin{aligned}&i\sum_{m=-\infty}^{\infty}\sum_{n=1}^{3}A^{(n)(m)}C_{3lpq}\alpha_p^{(n)(m)}k_q^{(n)(m)}e^{ik_3^{(n)(m)}x_3}e^{imGx_\parallel} \\ &= \delta_{l3}\sum_{m=-\infty}^{\infty}e^{imGx_\parallel}-(\sum_{M=-\infty}^{\infty}\mu_M e^{iMGx_\parallel})(\sum_{m=-\infty}^{\infty}\sum_{n=1}^{3}\omega^2A^{(n)(m)}\alpha_l^{(n)(m)}e^{ik_3^{(n)(m)}x_3}e^{imGx_\parallel})\end{aligned} \quad (3.34)$$

Here we define $k_1^{(n)(m)} = k_1 + mg_1$, $k_2^{(n)(m)} = k_2 + mg_2$. Rearrange the index and apply $x_3 = 0$:

$$\begin{aligned}&i\sum_{m=-\infty}^{\infty}\sum_{n=1}^{3}A^{(n)(m)}C_{3lpq}\alpha_p^{(n)(m)}k_q^{(n)(m)}e^{imGx_\parallel} \\ &= \delta_{l3}\sum_{m=-\infty}^{\infty}e^{imGx_\parallel}-\sum_{m=-\infty}^{\infty}\sum_{n=1}^{3}\omega^2\sum_{M=-\infty}^{\infty}\mu_M A^{(n)(m-M)}\alpha_l^{(n)(m-M)}e^{imGx_\parallel}\end{aligned} \quad (3.35)$$

which will give the final relationship between all the coefficients of linear

combination:

$$\sum_{m=-\infty}^{\infty} e^{imGx_\parallel} \sum_{n=1}^{3} [iA^{(n)(m)} C_{3lpq} \alpha_p^{(n)(m)} k_q^{(n)(m)} + \omega^2 \sum_{M=-\infty}^{\infty} \mu_M A^{(n)(m-M)} \alpha_l^{(n)(m-M)}]$$
$$= \delta_{l3} \sum_{m=-\infty}^{\infty} e^{imGx_\parallel} \tag{3.36}$$

It is clear that the harmonic terms in periodic mass loading cause the mixing between different eigenmodes. This is a linear algebra equation for all $A^{(n)(m)}$. It is impractical to consider all the harmonic terms. In my calculation I only consider up to the 5th harmonics, i.e. we treat $A^{(n)(m)} = 0$ if $|m| > 5$. Solving all $A^{(n)(m)}$ can give $u_3(\bar{k}_\parallel, x_3 = 0, \omega)$.

Using this method, I calculate SAW on Si (001) plane with 20 nm Al grating on top. The physics involved is discussed in Chapter 6. Fig. 3.5 is the dispersion curve of SAW with the presence of metal grating. $\mathrm{Re}(G_{33})$ shows the dispersion curve of SAW. Fig. 3.5a shows that metal grating creates band structure. $\mathrm{Im}(G_{33})$ represents the damping of SAW. Fig. 3.5b shows the attenuation of SAW by metal grating is due to the coupling between SAW and bulk acoustic wave.

3.5 Generalization of the calculation technique to other acoustic modes

From a general point of view, any acoustic behavior can be calculated using the same procedure detailed before: find specific solutions using general solutions, excitations, and boundary conditions. The following examples demonstrate the generality and versatility of Green's function method I implemented.

I calculated Stoneley wave, or the interface wave located at the interface between two half-space. In this case, there are two infinite half-space so both materials have only three appropriate eigensolutions. The boundary condition at interface is continuity of stress and displacement. To excite this wave, a δ excitation is placed right at the interface. Then the Stoneley wave can be observed, if there exists one. I have calculated the Stoneley wave at the interface of amorphous Al (c_{11} = 111.3 GPa, c_{44} = 26.1 GPa) and

amorphous W (c_{11} = 512 GPa and c_{44} = 153 GPa) and obtained velocity of Stoneley wave to be 2.73 nm/ps, comparing with the result in reference 2.77 nm/ps. There were a lot of theoretical researches about Stoneley wave regarding whether it exists or not for different materials combination.

Similar to Stoneley wave, in optical pump-probe system one can excite acoustic mode at the interface between layers (not necessarily interface between two half-spaces). For example a back incidence through a transparent substrate on an opaque film is this situation. To calculate this acoustic mode, the delta excitation in the multilayer case is moved from the free surface to the interface of chosen. The result is the mode excited by this particular excitation.

Another widely studied acoustic mode is the Lamb mode. It's the vibration of a suspended film with two free surfaces. To calculate Lamb mode, two free surface boundary conditions are applied at each surface which means all six eigensolutions are used. A delta excitation is applied on either side of the surface. Fig. 3.6 shows the color mapping of the Green's function of Lamb mode of a suspended Si layer of 2 μm thickness. There exist many different modes. Green's function method can conveniently show all of them and their relative amplitudes.

3.6 Implementation of calculation

At the early stage of my work, I was surprised to find that there isn't a calculation software for SAW calculation in the public domain. Most commercial calculation tools are finite element analysis, which are too complicated for my applications. They are also not helpful to build physical intuition about the acoustic behaviors.

Peng Zhao, a former group member in Professor Ji-Cheng Zhao's group at Ohio State University, wrote a code to calculate SAW of a "one layer on substrate" structure. He generously shared with me the code, which was very helpful for my following development of the calculation described in this chapter, to calculate SAW of multilayer structure and layered structure with thin metal grating.

I have put the implementation of most of the calculation described in this chapter in public domain: `https://github.com/dongyaoli/SAW` with

the hope of helping any fellow researchers. The software is implemented using MatLab right now. I am still working on a Python version. In this section I briefly describe the structure of the software.

What stated mostly in this chapter is how to formulate the linear algebraic equations. Once they are formed efficiently, the calculation software (`MatLab` or `Numpy` of `Python`) tailored for linear algebra can handle the calculation efficiently. However there is another non-linear equations, which is to solve the six eigenvalues and eigenvectors of the Cristoffel equation. There are two ways to solve the problem. The first one is to explicitly write down the sixth order equation and solve it using a non-linear equation solver. When it is implemented in `MatLab`, I found the accuracy of the solution is not high enough. A problem, for example, is that it cannot get degenerate eigenvalues since there is always small numerical difference. The solution to this right now in my implementation is to use the second method to solve the eigenvalues: the symbolic calculation package in `MatLab`. This is much more slower but the accuracy is satisfying. In the current implementation, the mapping of the dispersion curve in the Fourier domain is based on the solutions of non-linear equation solver, while the accurate calculation of the v_{SAW} uses the symbolic calculation.

The implementation is written under the concept of objective oriented programming (OOP) in order to conveniently add or remove layers without modifying the internal code. There is a simple interface for the users to just calculate the dispersion curve and v_{SAW}. There is another more complete interface to calculate detail properties of SAW, such as stress, strain, and energy over depth. The implementation also try to serve as a dictionary for mechanical properties of different materials to make the calculation more convenient.

3.7 Figures

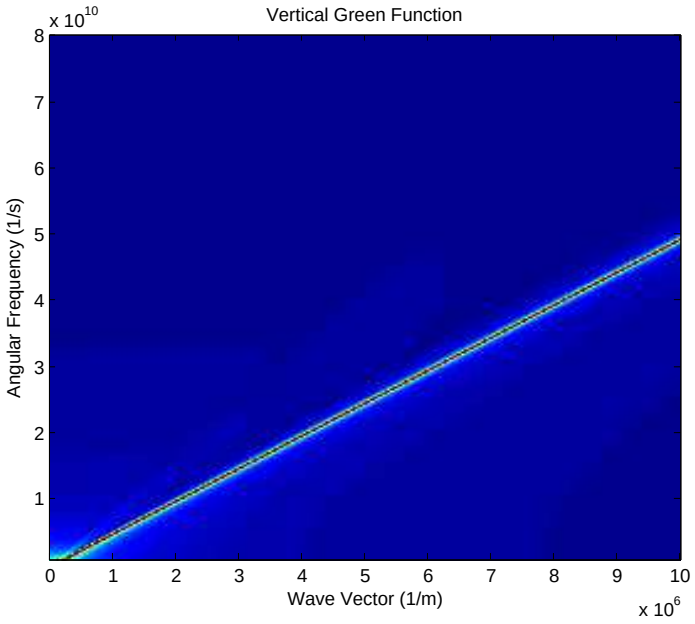

Figure 3.1: The color map of surface Green's function of SAW propagating on Si(001) plane at $\langle 100 \rangle$ direction, in the Fourier domain.

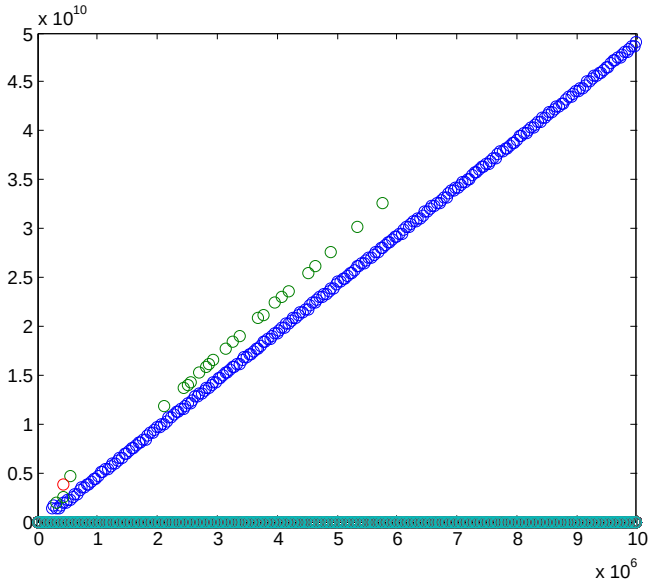

Figure 3.2: The extreme points extracted from the color map of Fig. 3.1. Certain modes that are not strong enough can also be picked up, like the green points. So the two plots should be used together to identify the blue points are the SAW and they form the dispersion curve.

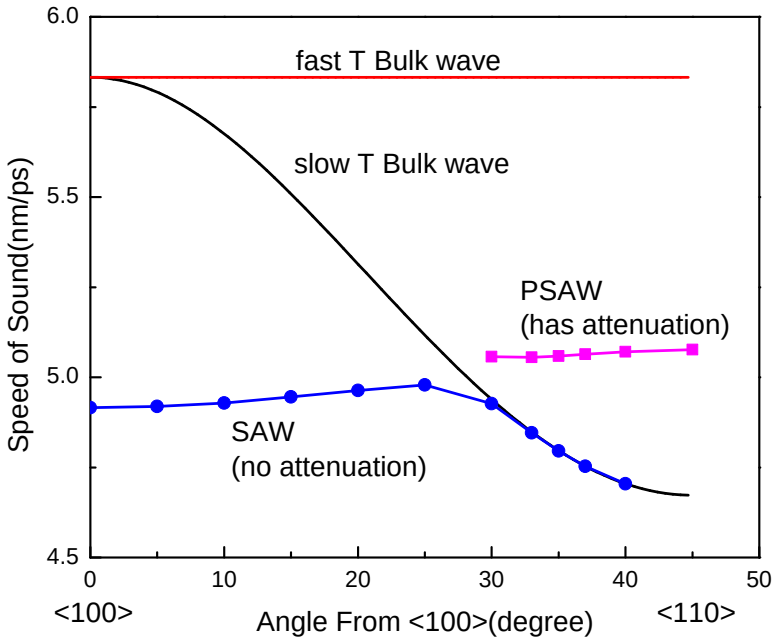

Figure 3.3: Comparison of velocity of different acoustic waves at different direction in Si. Both SAW and PSAW are propagating on the Si (001) plane. Line of bulk acoustic waves are from calculation. Points of PSAW and SAW are from calculation. The blue lines and pink lines are merely guides of eyes.

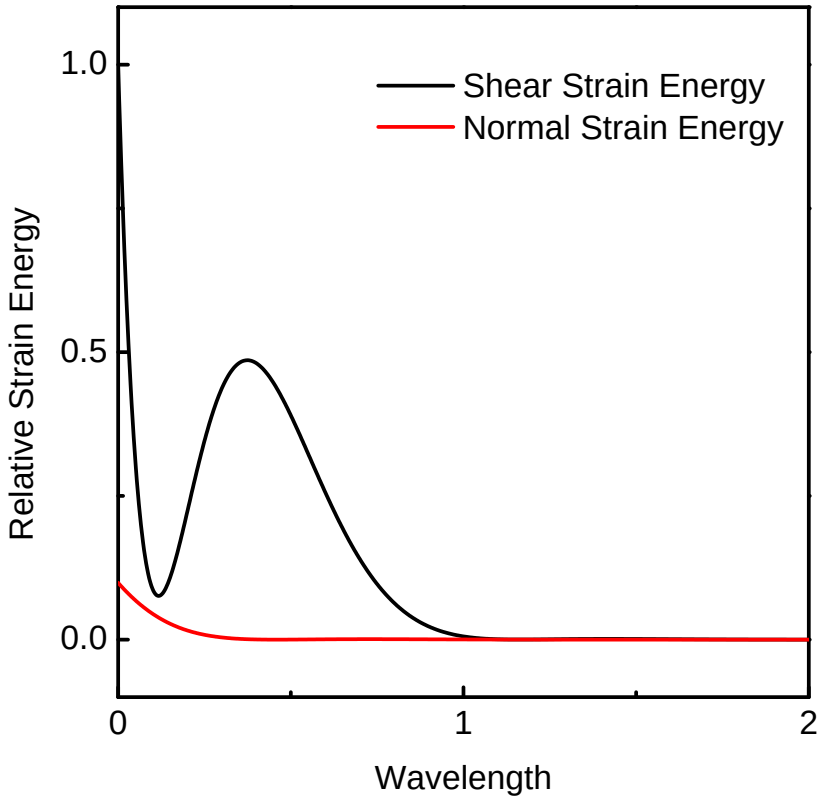

Figure 3.4: Relative strain energy at different depth of SAW propagating on Si (001) plane and ⟨110⟩ direction. The plot shows the majority of the strain energy is the shear strain energy. The detailed description of how to calculate each energy can be found in Chapter 6.

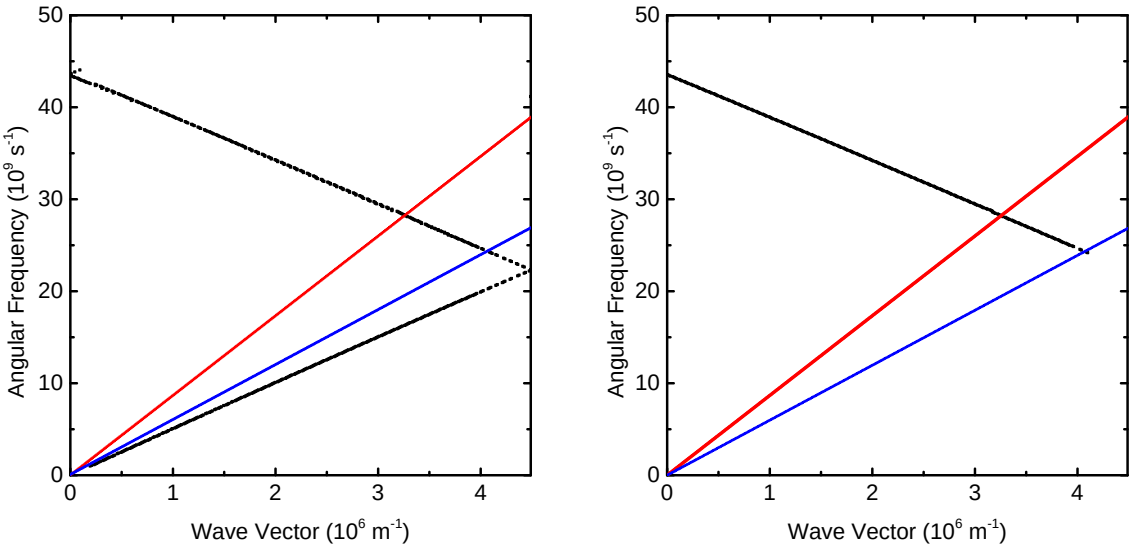

(a) (b)

Figure 3.5: Dispersion curve of SAW from 0 to π/λ with metal grating, drawn by plotting extreme points of $G_{33}(k_\parallel, x_3 = 0, \omega)$. In both figures, the blue line is the dispersion curve of bulk fast transverse acoustic waves and the red line is the dispersion curve of bulk longitudinal acoustic waves at Si $\langle 110 \rangle$ direction, and they are not from $G_{33}(k_\parallel, x_3 = 0, \omega)$ calculation but plotted separately. (a): Black line is $\mathrm{Re}(G_{33}(k_\parallel, \omega, x_3 = 0))$, which shows the mode folding and band structure in first Brillouin zone. (b): Black line is $\mathrm{Im}(G_{33}(k_\parallel, \omega, x_3 = 0))$. Imaginary part of Green's function appears only after SAW couples with bulk acoustic waves. The acoustic band gap is too small to be visible on this plot.

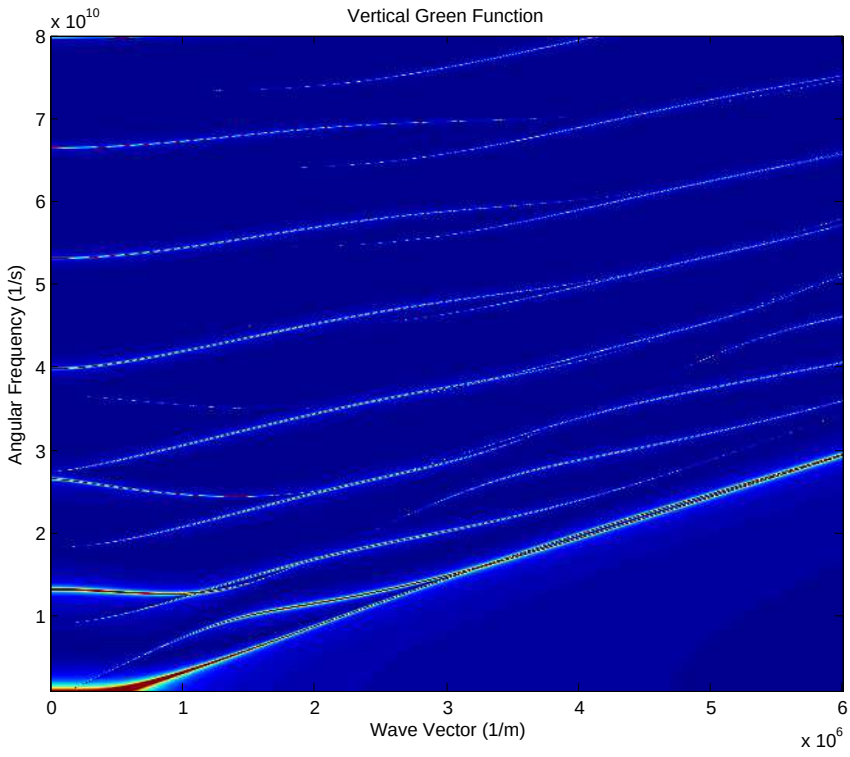

Figure 3.6: Map of surface Green's function of acoustic modes of a suspended Si film with thickness of 2 µm. Multiple modes can be identified as the Lamb mode of different orders.

CHAPTER 4

SURFACE ACOUSTIC WAVE TECHNIQUE USING ELASTOMERIC PHASE-SHIFT MASK

Longitudinal acoustic echo measurement is a successful technique to characterize thin film materials. It is used to measure film thickness if the speed of sound is known; or it is used to measure longitudinal elastic constant of opaque films if film thickness is known. High frequency SAW has the potential to be used as a general probe for measuring thin film materials, since it only exists in the surface region. But as discussed in Chapter 1, the existing methods, i.e. the transient grating method and patterned metal grating method, have certain limitations that restrict them to be used as general techniques. We are in needs of a convenient and compatible SAW technique to study shear mechanical properties of various kinds of thin film materials.

The technique I developed is to measure SAW in optical pump-probe system using a phase-shift mask. I briefly describe the concept of phase-shift methodology in next section.

4.1 The concept of phase-shift methodology

Photolithography has long been the dominate lithography method in semiconductor industry due to its high stability and high yield. The feature size in photolithography is limited by the wavelength of the laser. Laser with small wavelength but high enough power is difficult to make. In order to increase the resolution of photolithography, in the past decades, the so-called phase-shift lithography has been developed and successfully applied in photolithography in semiconductor industry.

In the phase-shift lithography, certain transparent region of the photomask is designed to be thicker or thinner in order to tune the phase of light arriving at the photoresist, so the light is designed to be constructively or destructively interfere with each other at different position of the pho-

toresist. Thus the feature size can break through the limitation of the laser wavelength [34, 35].

Although the concept of phase-shift looks simple and straightforward, the design cannot be based on simple phase estimation. This is because the feature size in phase-shift mask is almost always below the wavelength of the laser. To calculate the effect of the structure to the electromagnetic wave requires carefully solving the Maxwell equations. Whether it's a near field effect or far field effect also matters greatly. So a finite element numerical calculation of electromagnetic wave is almost always necessary. In fact there is usually a whole team in big semiconductor company to design the phase-shift mask to suit specific needs. It's typically a very heavy computation. Fortunately the phase-shift mask I utilize is a simple binary phase-shift mask with only a few geometry variables. A commercial finite element software is enough for the mask design, which I describe in Sec. 4.3.

4.2 Experimental design

As discussed in Chapter 1, one of the limitation of the transient grating technique is that the wavelength of SAW is limited by both laser wavelength and separation angle. High frequency SAW with sub-micron wavelength is difficult to achieve. The concept of phase-shift is clearly a good solution. Actually back in 2002, the Maris group at Brown University has already tried a similar approach [36]. They put a diffraction grating very close to the sample surface and did the measurement in standard pump-probe system. Later in 2015 (after our technique is published in 2013), Maris group published another paper [37] which refined their technique by carefully controlling the distance between the hard optical grating and perform the measurement in a cleanroom environment.

The problem of the approach of Maris group is the contact between the hard glass grating and the sample surface, i.e., it's difficult to guarantee a good contact even in a cleanroom environment. Any small particles between the hard grating and sample can cause a gap between grating and sample surface, which directly changes the phase-shift behavior. So the signal is not consistent and stable. If conformal contact between grating and sample is needed, the hard grating requires the sample to be perfectly flat and clean.

These requirements greatly limit the application of the technique.

4.2.1 Binary elastomeric phase-shift mask

To solve the contact problem, I use a soft phase-shift mask instead of a hard mask. The fabrication of the elastomeric phase-shift mask is a simpler version of how to make PDMS stamp described in Chapter 2. The prepolymer of PDMS (Sylgard 184, Dow Corning) was cast and cured (80 °C, >2h) on a silicon grating mold (LightSmyth Technology). Degassing is need before the curing to remove any visible bubbles.

In the experiments, I usually use two silicon molds. One has 700 nm periodicity, $\approx$ 50% duty cycle, and 350 nm groove depth. The second mold has 500 nm periodicity, $\approx$ 50% duty cycle, and 350 nm groove depth. I choose these groove depth because the calculation, described in Sec. 4.3, shows these groove depths give relatively strong signal. A significant drawback of the 500 nm period PDMS mask is that the grating can be easily deformed into domains of shorter and longer periods. This is because the aspect ratio of the pitch of the PDMS grating is too high so it "collapses". To solve this problem, I incorporate a layer of PDMS with higher elastic constants on the grating side of the mask, the so-called "hard PDMS" same as the one used in nano-imprint lithography. So the process to make a "hard PDMS" mask is the exact same as the process of making a PDMS stamp described in Chapter 2, except the phase-shift mask is usually thinner (a few mm). This "molding" process doesn't cause any observable damage to the silicon master. I have been using the same silicon master for years.

It seems to me that PDMS is the go-to material in nano-fabrication as a handling material. It has very stable property and is very easy to work with. There is no restrict requirement in neither the recipe nor curing process. As a phase-shift mask, it completely solve the contact problem. PDMS is relatively sticky, so it can adhere to the sample well enough to support its own weight without any external force. It is also soft, so it can bend to tolerate small particles and roughness, as long as the particle won't cause a complete delamination of the mask from the sample. One can just avoid the region with particles or high roughness in the measurement. Since PDMS is sticky, it is very easy to get dirty, especially if the sample itself doesn't

have a clean surface. Also I found the PDMS grating, after curing for a few hours, can degrade after it is peeled off and exposed in air. One can easily observe the degradation by looking at the sample with PDMS mask through the CCD camera and objective length in the pump-probe system. The degradation is the visible straight lines appeared. This problem can be mitigated to some level by curing the PDMS mask for much longer time. But it's not very effective. So what I do is to make a new mask every time I need to the measurement so I can be sure that the mask is clean and defect free. The hard PDMS feature can be preserved much much longer. I don't observe any damage to it by just exposing it to air for years. The imprint process in nano-imprint lithography can cause some damage to the hard PDMS stamp. One needs to make a new stamp after about tens to hundreds of imprinting. The disadvantage of hard PDMS phase-shift mask is that it is much less sticky than the conventional PDMS so it is more difficult to form a good contact with the sample.

4.2.2 Measurement mechanism

The schematic of the sample configuration is shown in Fig. 4.1, which is a elastomeric binary mask attached on the surface of the sample. As in the standard optical pump-probe system, if the sample does not have a short optical absorption depth, i.e., the sample is a dielectric or semiconductor, then it must be first coated with a metal film as transducer: I usually use Al. To measure SAW, the PDMS phase-shift mask is physically attached to the sample surface by tweezer, with the grating side towards the sample surface. For a very clean and smooth surface, the phase-shift mask can immediately form a conformal contact with the sample. If this is not the case, one can gently tap the top of the mask to get rid of the air in between. One can easily notice when the air is pushed out from the contact. One can also easily tell if the contact is good or not by looking at the image of CCD camera with sample illumination: area with good contact usually shows homogeneous bluish color (color depends on the setting in camera and the illumination) while an air gap between mask and sample has no color (black).

When the pump pulse goes through the phase-shift mask, it forms a periodic intensity pattern on the metal transducer surface as shown in Fig 4.4,

due to the design of phase-shift. The periodic intensity creates a spatially periodic temperature profile along the surface, a corresponding thermoelastic strain, and excitation of narrow band SAW.

The SAW is detected through time-dependent changes in the intensity of the back-reflected probe beam. As discussed in Chapter 2, there are two classes of effects that could conceivably contribute to the change in reflectivity: i) the dependence of the refractive index of the meterials on strain; and ii) the displacement of the metal surface as is typically the case in the longitudinal acoustic echo measurement. The metal transducer in our measurement is highly textured (deposited by sputtering). Due to symmetry of the transducer film, a normal incidence probe beam is not sensitive to shear strain perpendicular to the sample surface. Therefore I conclude that the detection comes predominately from surface displacements. The change in reflectivity created by a surface displacement is spatially modulated by the PDMS mask. Experiments on a variety of metal films deposited on Si, which is discussed in Sec. 4.4, support this conclusion.

I find that the pump and probe polarization relative to the orientation of the grating of the mask strongly affects the signal intensity. In our pump-probe system, pump and probe pulses have orthogonal linear polarization, so that the scattered pump beam can be better separated from the reflected probe. The maximum signal in the SAW measurement by phase-shift mask is created when the electric-field polarization of the pump is perpendicular to grating vector and, therefore, the polarization of the probe is parallel to the grating vector. Prior work [36] using a metal-patterned polymeric mask to generate SAW has also demonstrated the dependence of SAW intensity on polarization of light relative to the grating orientation. I discuss the polarization effects in Sec. 4.3 where I conclude that the change of signal intensity for different configurations of polarization is mainly due to changes in the sensitivity of the probe to surface displacements and not due to changes in the absorption of the pump.

The attached PDMS phase-shift mask produces a strong periodic perturbation to the optical response. Since it is attached with the sample surface, it also pose a periodic perturbation to the elastic response of the material. The effect of a periodic perturbation to the properties of SAW is closely examined in Chapter 6. The experimental validation described in Sec. 4.4 suggests that the effect of the PDMS mask on the SAW velocity is negligible.

This aspect is brought up again in Sec. 4.5 and Chapter 5.

The example data are shown in Fig. 4.2, which is acquired with the 700 nm period PDMS mask and an Al-coated Si sample. The slowly decaying background is caused by the relaxation of the temperature of the Al transducer. After background subtraction, I analyze the frequency f of the oscillations using Fourier transforms and fitting of the data to a damped sinusoidal function. An example of the fitting is shown in Fig. 4.11. The fitting doesn't need to be perfect, since the thermal background cannot be fully removed and there can be some weaker acoustic modes and higher harmonics. The fitting result for frequency is good enough and better than result of Fourier transform. The SAW wavelength is the same as the period of the mask. The SAW velocity is $v_{SAW} = \lambda f$

4.3 Design of optimal phase-shift mask geometry

To explore the optimal geometry for the phase-shift mask, I use a commercial software (FDTD Solution, Lumerical) to estimate how efficiently the phase-shift mask generates SAW by the pump beam and enables detection of SAW by the probe beam. The calculations involve only the optics of the problem; i.e., I consider only the spatial modulation of the absorption of the pump beam and the change in the reflectivity of probe beam created by different configurations of surface displacements. The calculations do not include the thermoelastic mechanisms for generating SAWs by a laser pulse. I vary the grating period and groove depth to determine which grating geometry creates the highest spatial modulation of the absorption of the pump; and which grating geometry creates the largest change in the reflectivity of the probe when the acoustic wave has a phase of 0 or 180°relative to the grating.

The calculation is standard finite element calculation. The lateral dimension of the computational cell, see Fig. 4.3, is one grating period with periodic boundary conditions to the left and right. The top and bottom boundaries fully absorb incident light (perfect matching layer, PML). The sample layer is modeled using the optical index of refraction of Al and is optically opaque. I used $n = 1.43$ for the PDMS optical index of refraction. A planar Gaussian wave-packet with a center wavelength of 785 nm (center wavelength of our pump-probe system) and a full-width-at-half-maximum of

600 nm was launched toward the Al layer through the PDMS mask. I use a 1 nm mesh size for the Al layer and the region near the Al/PDMS interface, and used gradually larger mesh sizes ($\approx$ 10 nm) in the majority of the area of the computational cell to reduce the calculation time. Al requires finer mesh because it has very short absorption depth, in another word, the electromagnetic wave can change very quickly spatially within the metal. A "monitor" is placed over all Al to record the absorbed electromagnetic wave. The intensity pattern in Fig. 4.4 is from the result of the calculation. A "monitor" is placed on the path of the reflection to record the intensity of reflected probe beam. The grating structure at the interface indeed behavior like a grating in the far field. To record the reflected probe beam, the calculation needs to be performed long enough until all the reflected probe passes through the "monitor". There is a obvious front of the reflected pulse. But there is also a "tail", which should be from the diffraction of the light from the region outside of the calculation cell (recall the periodic boundary condition is applied). The intensity of the reflected pulse should be the sum of two parts. Fig. 4.5 shows the clear front of the reflected pulse and the tail.

I calculate the spatial modulation of optical absorption in the Al layer to gain insight into the efficiency of the mask for generating SAW. Pump pulses have perpendicular polarization relative to the grating vector. I sum the absorbed energy over depth at each lateral position. Fig. 4.6 shows the optical absorption density of the pump beam in one unit cell for different geometries of the phase-shift mask. To make these comparisons, I set the integral of the incident plane wave energy over a 700 nm interval to unity. The lateral position, i.e., the x-axis of the plot, is normalized by the mask period. In the left half of the computation cell, the Al film is in contact with the PDMS mask; in the right half of the cell, the Al film is exposed to the air gap. As the period becomes smaller, the contrast between the maximum and minimum absorption decreases rapidly. I use the difference between the mean absorption density of the left and right region to estimate the relative amplitude of thermoelastically-generated SAW.

For detection, I simulate two configurations of the surface displacement: displacing the left half of the Al surface versus displacing the right half of the Al surface. A probe pulse with electric-field polarized parallel to the grating vector of the mask is launched at the mask and Al film. I analyze the back reflected intensity in the far-field and define the efficiency of detection as the

difference between the reflected intensity in these two configurations of the surface displacements.

The signal detected in the experiment is proportional to the product of the acoustic wave amplitude generated by the pump pulse and the detection efficiency of the probe. The calculated variation of signal intensity with groove depth for the 700 nm period mask is shown in Fig. 4.7. The detection efficiency and signal intensity show a peak near a groove depth of ≈ 300 nm, close to the groove depth I use in the experiments, ≈ 350 nm.

The calculated signal intensities for a selection of mask periods and groove depths is summarized in Fig. 4.8. I use a groove depth of 350 nm for the 500 nm and 700 nm periods because the Si molds needed to fabricate these masks are commercially available and these are the structures we studied experimentally. I have not studied grating periods smaller than 500 nm experimentally. For the calculations for the 300 nm and 200 nm period gratings, I assume that it will be impractical to create groove depths that are larger than the period and therefore set the groove depth equal to the period. The signal intensity decreases rapidly with decreasing grating period. The calculations predict a factor of ≈ 8 suppression of the signal for the 500 nm mask relative to the 700 nm mask. In experiment, I observe a similar decrease in the signal intensity, a factor of ≈ 6, see Fig. 4.8.

I also consider the polarization dependence of the signal intensity. The calculations described above use the optimal polarization with the polarization of the probe parallel to the grating vector and the polarization of the pump perpendicular to the grating vector. Rotating the polarization of pump and probe by 90 degree, a configuration I refer to as "P2", strongly suppresses the signal intensity, by a factor of ≈ 100 in the calculation and by a factor of ≈ 10 in the experiment, see Fig. 4.8. Most of the reduction in predicted signal intensity comes from the reduction of the detection efficiency. I speculate that with the P2 polarization, the surface displacement of the sample does not dominate the detection efficiency and other phenomena come into play. For example, the calculations do not take into account the change in the optical index of refraction of the PDMS with strain or deformations of the PDMS mask in the lateral directions.

4.4 Experiment validation

I perform two sets of experiments to validate this approach. First, I measured the SAW velocity v_{SAW} on several materials with well-known elastic constants, see Fig. 4.9. All of these materials are single crystals except for Au; the Au sample is a polycrystalline film ($\approx$ 1 µm thick) deposited by sputtering with strong (111) texture; the grains are randomly oriented about the [111] axis. All of the samples were coated by a 20 nm thick layer of Al to serve as a transducer. The elastic constants, the surface orientation, the direction along which we measured v_{SAW}, and the measured and predicted values are very similar.

In the second set of experiments, I measure v_{SAW} for a wide range of thicknesses of V films deposited on a Si substrate. The result is shown in Fig. 4.10. The Si substrate affects the SAW velocity significantly when the V film is thin. When the thickness exceeds $\approx$ 300 nm, the substrate effect is quenched. For a layered structure, the SAW is dispersive. When the film thickness is small compared to the wavelength, the wave extends further into the substrate and v_{SAW} approaches the value of the substrate. When the film thickness is large compared to the wavelength, the wave is concentrated in the film and v_{SAW} approaches the value of the film.

In both cases, see Fig. 4.10, I compare the measured velocities to the predicted velocities using SAW calculation described in Chapter 3 and previously published values of the elastic constants of each material. The relative rms errors for these two sets of experiments are 0.036 and 0.017, respectively. The data shows that the presence of PDMS grating does not affect the SAW velocity significantly and the method can be used to reliably measure v_{SAW}.

Finally, I measure the signal intensity created by different metal transducers to test the assertion that the detection efficiency is mainly determined by surface displacements and not by the strain dependence of optical index of refraction of the metal film transducer. I sputtered different metal transducers with thickness of $\approx$ 40 nm on (100) Si substrates and measured the SAW signal intensity. The data is summarized in Fig. 4.12. I normalize the signal intensity by the reflectivity and plot the result as the y axis. I do not attempt to fully model the generation of the SAW but argue that the thermoelastic stress should scale with the product of the optical absorption $1 - R$, the biaxial modulus M and the coefficient of thermal expansion α_T;

and inversely with the heat capacity per unit volume C. In Fig. 4.12, the x axis is chosen to reflect this expected scaling. Interestingly, variations in the normalized signal intensities $\Delta R/R$ and variations in $(1-R)M\alpha_T/C$ are relatively modest, spanning less than a factor of 2, but show a trend of increasing signal $\Delta R/R$ with increasing $(1-R)M\alpha_T/C$. Since the dependence of the optical index of refractions of the metals with stress is expected to vary significantly, the relatively small variations in $\Delta R/R$ that are mostly accounted for by variations in $(1-R)M\alpha_T/C$ supports the assertion that the detection is mostly determined by surface displacements. The detailed data used can be found in Ref. [38].

4.5 Possible modification to the elastomeric phase-shift mask

As mentioned before, the PDMS mask poses a mechanical perturbation to the system. The experimental validation in Sec. 4.4 demonstrate that this effect is very small for hard material. But as is discussed in next chapter, if the film of interest is a soft material, the mask can have clear effect to the measurement in some cases. Also the mask poses substantial damping to the SAW generated. One can barely measure the propagating SAW by offsetting the pump and probe beam. This strong damping should be due to the contact between the mask and the sample surface.

I propose a method to try to separate the mask and sample surface by small amount so there won't be direct contact for the purpose of easy attenuation measurement. My idea is to suspend part (several μm wide) of the mask through nano-fabrication. The structure can be successfully fabricated. However the PDMS is not stiff enough to maintain that huge aspect ratio and the suspended part would collapse on the sample surface. Even the hard PDMS is not good enough. I spent appreciable amount of time try to find a proper material but failed. The best candidate I can find to have enough stiffness and is relatively convenient to fabricate is the Norland optical adhesive of various kinds. But they still didn't work. So either better material or better design is needed to achieve this.

Since I wasn't able to separate the mask with the sample, I tried to quantify the effect of mask on v_{SAW}. What I did is to use a second phase-

shift mask, no longer binary but with a square pattern. This can also be purchased from the company LightSmyth. The mask with square pattern can also create SAW following the same phase-shift philosophy but the signal is weaker. I measured v_{SAW} of an exfoliated graphite flake using two masks. And I found the difference between the two results are much smaller than the experimental error.

4.6 Figures

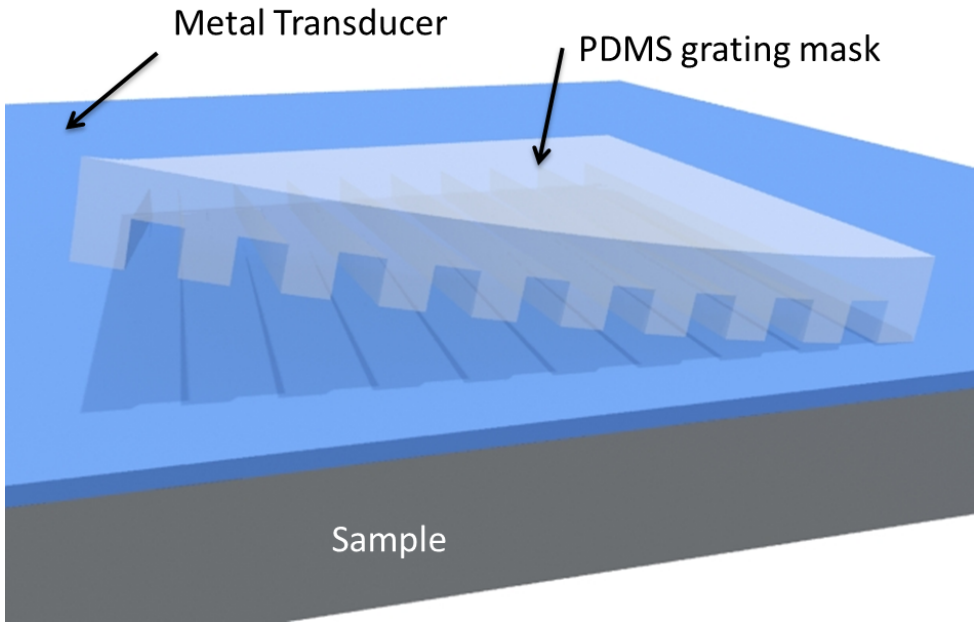

Figure 4.1: Schematic of the sample geometry in SAW measurement with phase-shift mask. The size of the mask is about 1×1 cm^2. The mask is physically attached to the sample by hand or tweezer without any external pressure or glue.

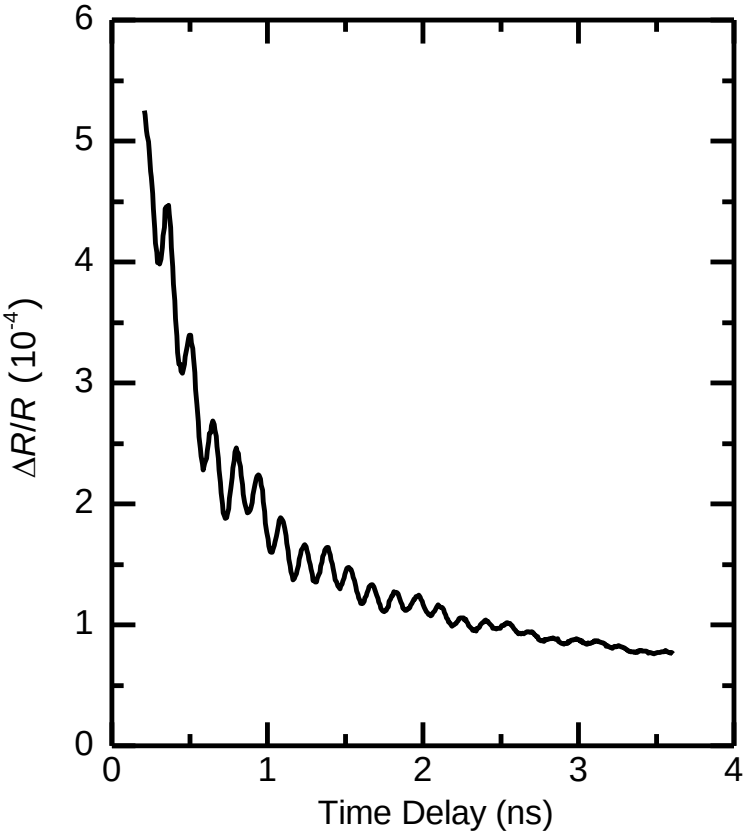

Figure 4.2: Typical data for the change in reflectivity as a function of delay time between the pump and probe using the 700 nm period PDMS mask. The sample is a 20 nm thick film of Al deposited on a Si (001) wafer..

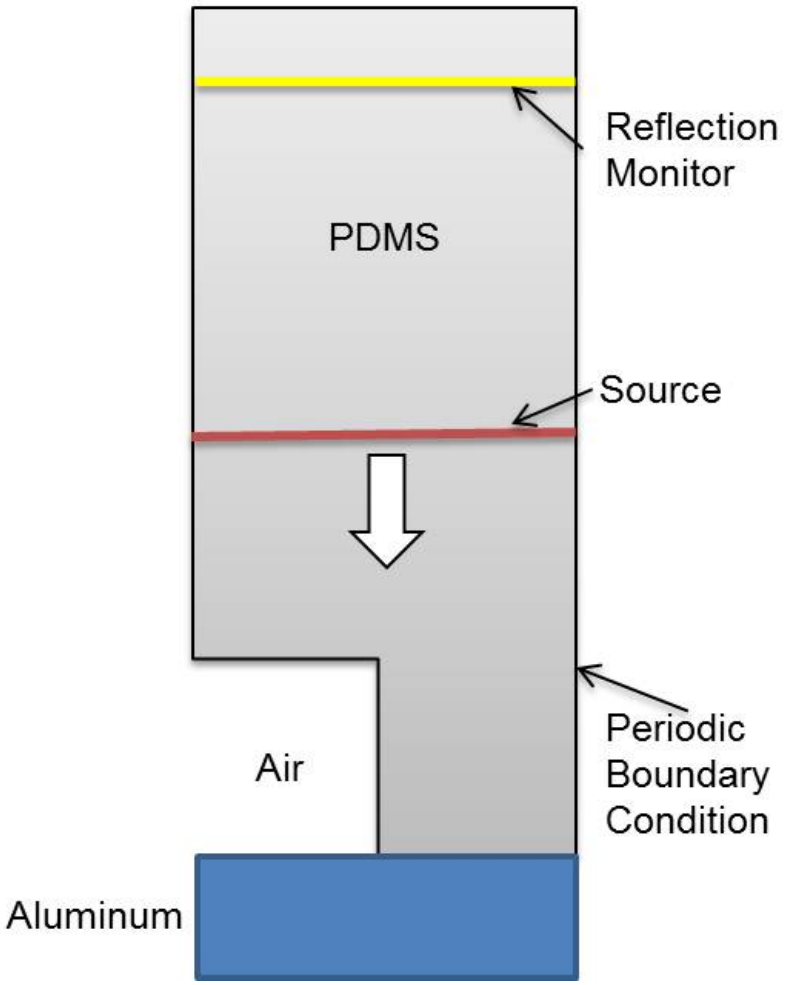

Figure 4.3: The computational cell (not to scale) for electromagnetic calculation by finite-difference time-domain method. I use periodic boundary conditions in lateral direction. The Al layer is 20 nm thick and therefore optically opaque. The reflected intensity is monitored at the location labelled "reflection monitor" > 40 µm from the Al surface.

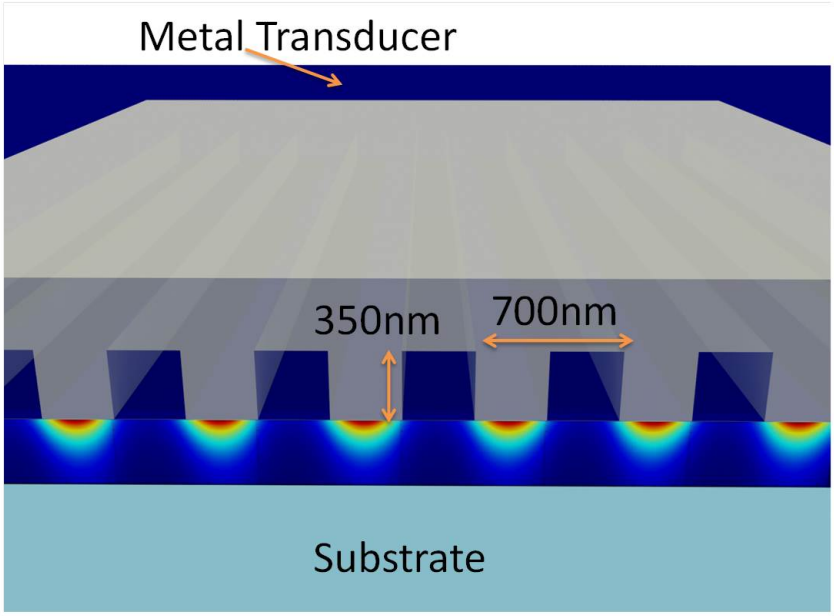

Figure 4.4: Surface heating after a pump pulse goes through the phase-shift mask. The heating profile is from the FDTD calculation. The dark blue region right beneath the mask is the Al layer.

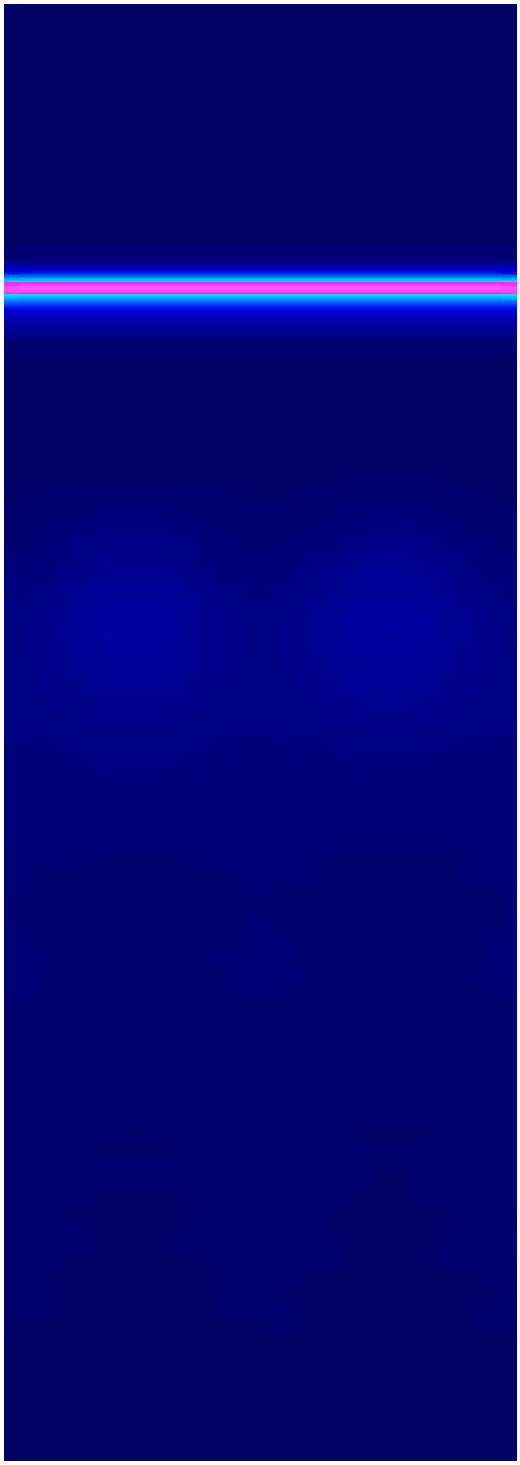

Figure 4.5: Profile of the reflected probe pulse. The strong front can be identified. But there are clearly wave behind the front, which should be from the diffraction due to the grating feature.

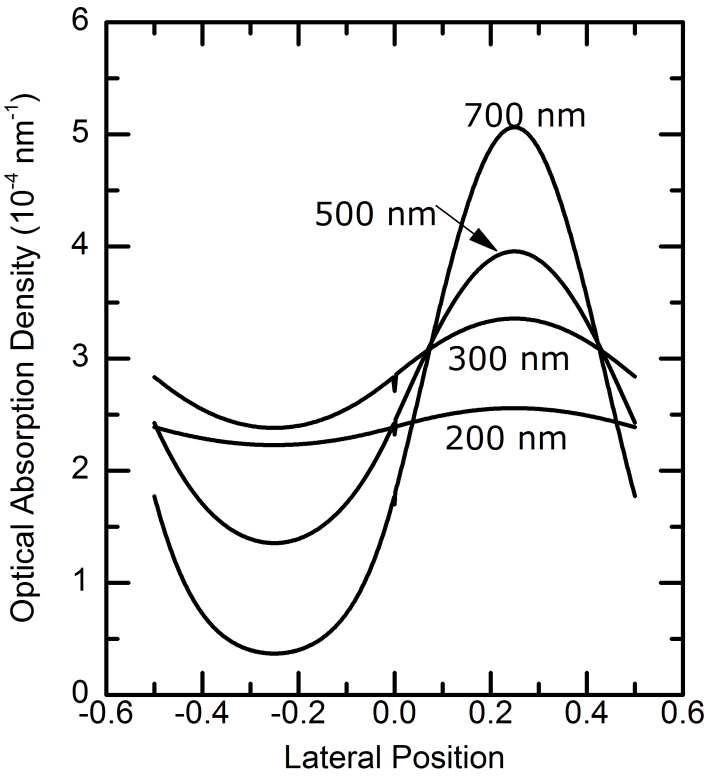

Figure 4.6: The calculated optical absorption energy as a function of lateral position in the Al layer for one unit cell of the grating. The x-axis of the plot is scaled by the mask period and is therefore dimensionless. The absorption density is calculated by setting the incident plane wave energy integrated over a 700nm region to unity. For 700 nm and 500nm period masks, the groove depth is 350 nm; for the 300 nm and 200 nm period masks, the groove depth is the same as the period. The optical wavelength is 785 nm.

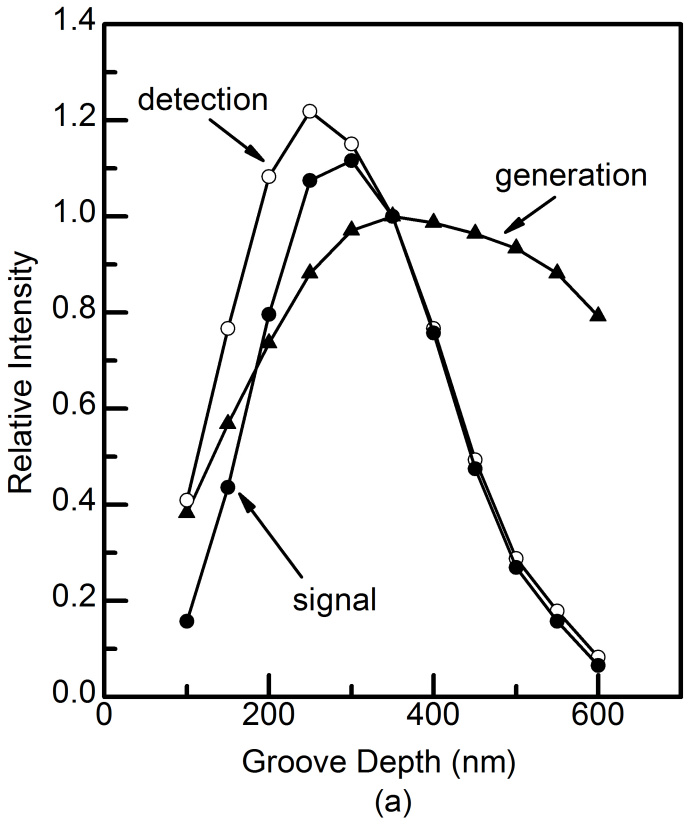

Figure 4.7: Calculated generation (filled triangles), detection (open circles), and signal efficiency (filled circles) variation with groove depth for the 700nm period mask. The plotted intensities are scaled by the value for the 350 nm groove depth that was used in the experiment.

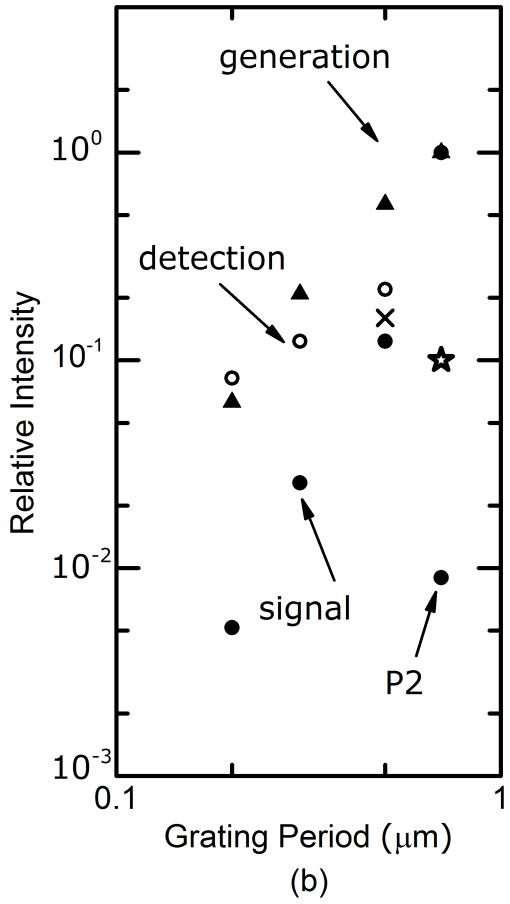

Figure 4.8: Calculated signal intensity of selected mask configuration. For 700 nm, and 500nm period phase-shift masks, the groove depth is 350 nm, as used in the experiments. For the 300nm and 200 nm period masks, the groove depth is the same as the period. Each set of data is scaled by the value of 700nm period mask. The cross shows the experiment signal intensity of the 500nm period mask. The star-shaped symbol shows the experiment signal intensity of the P2 polarization using the 700nm period mask.

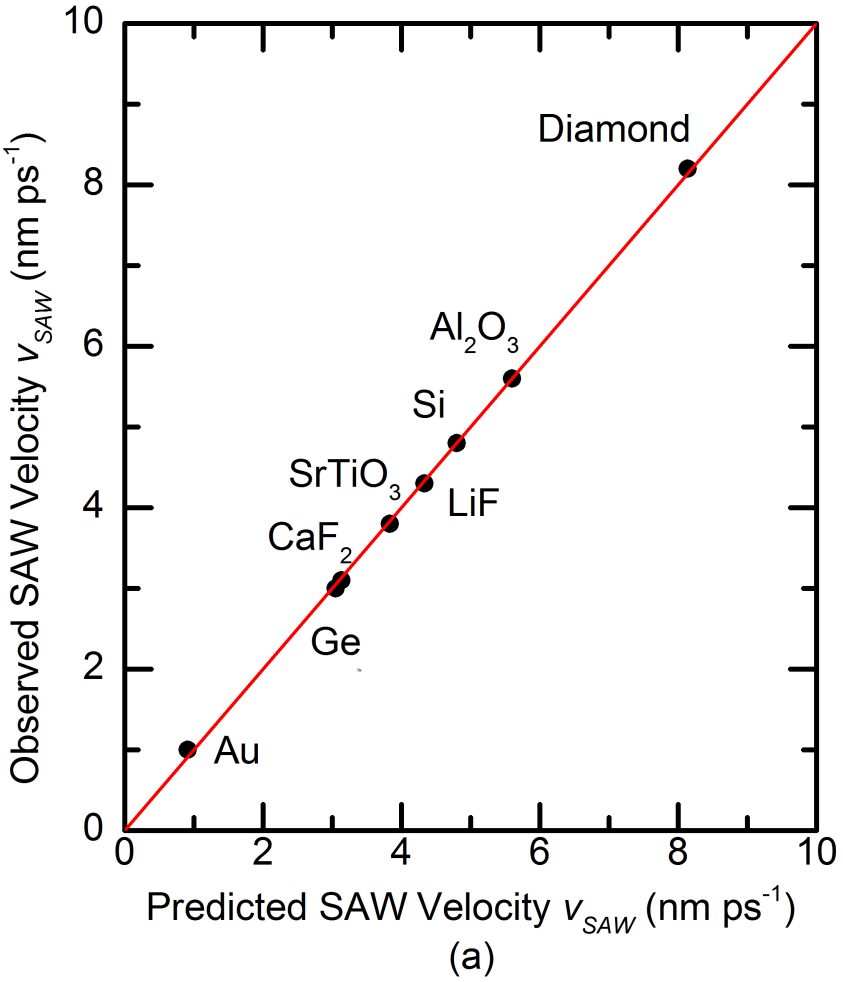

Figure 4.9: Measured v_{SAW} for variety of materials plotted as a function of the predicted v_{SAW} based on previously published values of the elastic constants. The solid line denotes perfect agreement. In this set of data, the relative RMS error is 0.036.

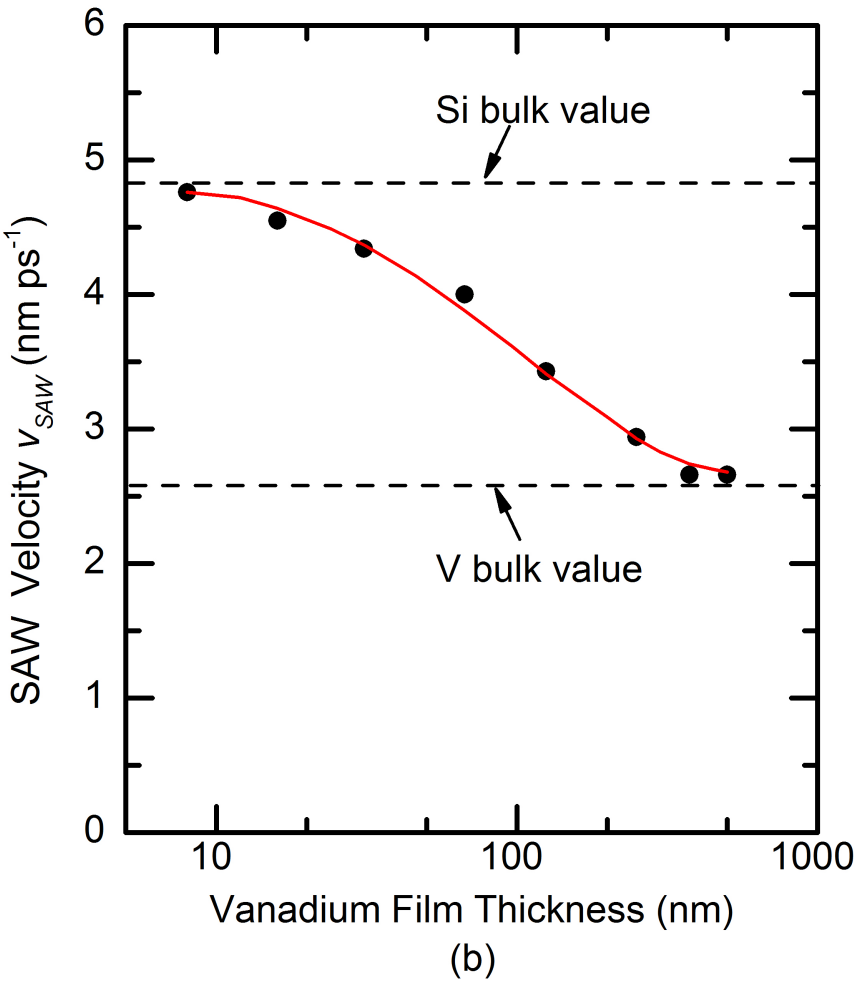

Figure 4.10: Measured v_{SAW} for V thin films deposited on a Si (001) wafer. The V films are polycrystalline with a strong (110) texture. The measurement is along the Si $\langle 110 \rangle$ direction. The solid line shows the predicted v_{SAW} which is averaged of all the combination between the crystal orientation of (110) plane of V and the $\langle 110 \rangle$ direction of (100) Si plane. The relative RMS error is 0.017.

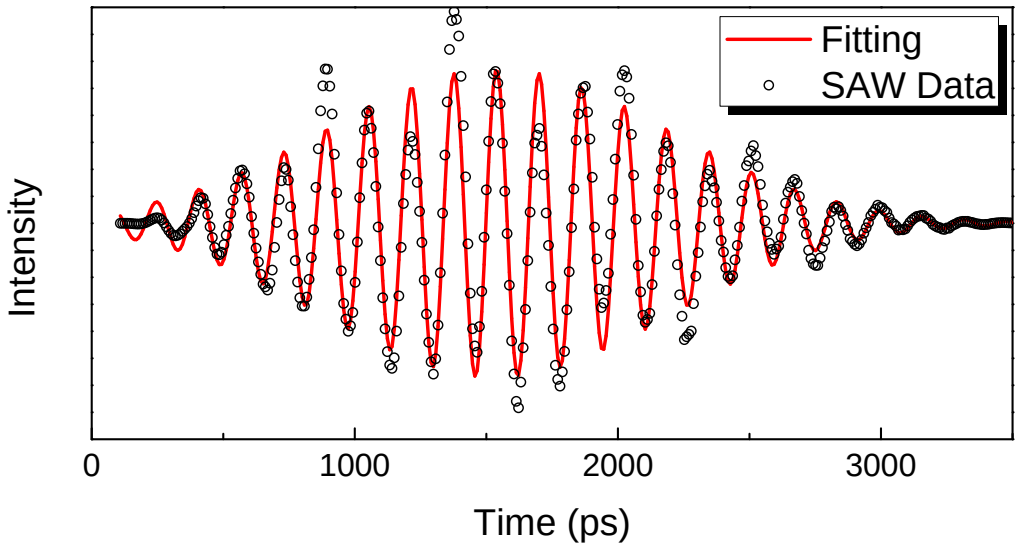

Figure 4.11: Fitting of the measured oscillation (after background is subtracted and a Gaussian window is applied) with a Gaussian modulated sine wave, in order to obtain the frequency of the signal. Both the center position and the width of the Gaussian window are the fitting parameters. So the total fitting parameters are five: frequency, phase, and amplitude of the sine wave, and the width and center of the Gaussian window.

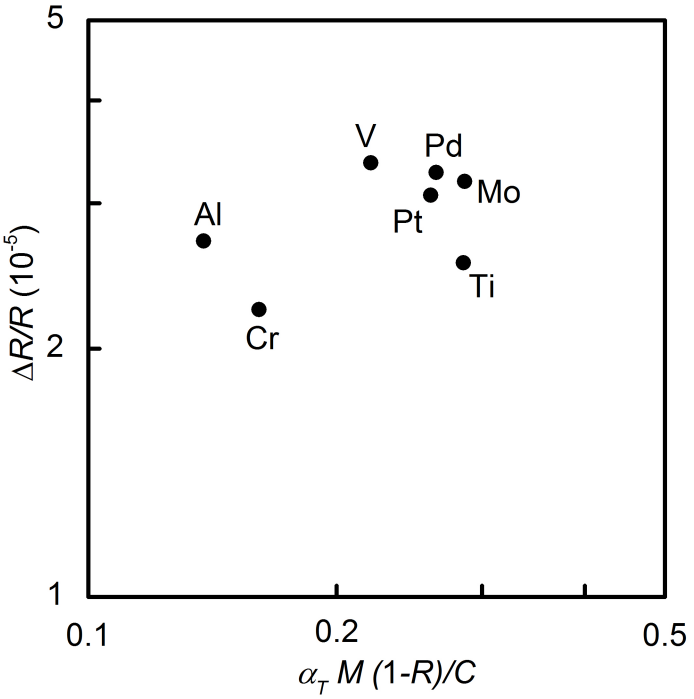

Figure 4.12: Relationship between normalized signal intensity $\Delta R/R$ and scaling factor for SAW generation $(1-R)M\alpha_T/C$ for different transducers. R is reflectivity, α_T is coefficient of thermal expansion, C is volumetric heat capacity, M is biaxial modulus.

CHAPTER 5

MEASUREMENT OF SHEAR ELASTIC CONSTANT OF THIN FILM MATERIAL BY SURFACE ACOUSTIC WAVE

The purpose of the SAW technique developed in last chapter is to find a convenient and compatible method for measuring shear elastic constant of thin films. The advantages of using elastomeric phase-shift mask over other methods, such as transient grating or metal grating method, is that it can be conveniently applied to any materials as long as the surface is smooth enough for the optical pump-probe experiment. One can physically attach the phase-shift mask on the surface of the sample and peel it off from the sample without any damage to it. No complicated nano-fabrication method is required. Also the wavelength of the SAW I usually use is 700 nm, which means v_{SAW} is sensitive to films of thickness on the level of 100 nm. This would satisfy most of our current needs. In this chapter I demonstrate the capability and applicability of the technique by measuring shear elastic constant of various different films. I also describe analysis and modifications of many aspects of the method to suit for different kinds of materials.

5.1 General procedure of measuring shear elastic constants of half-space and thin layers

5.1.1 Experiments detail

In a typical SAW measurement, after the phase-shift mask is attached to the sample surface, the optical system is aligned the same way as in a front side TDTR measurements. The typical measurement is done with overlapping pump and probe beams. I find that offsetting the pump and probe beam by a few micron to measure a propagating SAW doesn't contribute much to the quality of the signal and the signal can be too weak. To measure SAW or any acoustic behavior in the optical pump-probe system, although the thermal

signal is not of concern, I still set the phase of the signal to be in-phase with the reference. I set the phase by making the out-of-phase signal flat across the zero time delay which is the same method as in TDTR measurement. Setting the phase correctly helps the identification of any abnormal behavior. The SAW measured by one probe pulse is excited by the pump pulse accompanied to this probe pulse. If the phase of the Lock-in amplifier is set to compensate the phase changes caused by the other components of the system, then the acoustic signal should be completely in-phase relative to the reference. Because after 12.5 ns the SAW has already propagated out of the measurement region or attenuated. So all the SAW signal is in the in-phase channel. An longitudinal acoustic echo measurement is also performed to measure the Al thickness and longitudinal elastic constant of the material.

After collecting the oscillation signal from the in-phase channel, the next step is to analyze the frequency of SAW. The easiest way is to apply a fast Fourier transform (FFT) to the signal and identify the peak in frequency domain corresponding to the SAW. This require that the data points collected in pump-probe system to be equally spaced (requirement of the FFT algorithm). The time window of the measurement is ≈ 4 ns, which is limited by the length of the delay stage. The time window limits the resolution of Fourier transform to be around 0.4 GHz in our current case. The SAW frequency is usually around a few GHz. So this resolution of frequency is typically not good enough. An alternative is to fit the SAW oscillating signal with a sine wave. What I usually do is to first subtract the thermal background using polynomial or any function that can fit the background relatively well (note not to introduce any new frequencies or change the frequencies of interest); then I apply a Gaussian window on top of the signal with the center of the Gaussian at the center of the total signal; the last step is to fit the processed signal with a Gaussian modulated sine wave. The fitting involves five parameters: amplitude, frequency, and phase of the sine wave and the center and width of the Gaussian window. In my experience, this fitting is not difficult if the initial parameter is set close enough to the optimal value. The initial values can be easily estimated. The initial frequency is from Fourier transform and the center and width of the packet can be estimated using local maxims of the signal. The fitting only works if the signal is dominated by one frequency. If there are strong interference between frequencies, I find it is difficult to fit two frequencies out of the signal. There

are too many variables.

In practice, I can always measure a weak component with frequency at $1 \sim 2$ GHz in any SAW measurement. It poses a small background. Sometime it can interfere with the SAW component at early delay time. I can also observe possibly second harmonic of the SAW. It is damped greatly in the early hundreds of picoseconds. So usually I can fit the signal with no problem. The early signal can be omitted or damped by the edge of Gaussian window.

v_{SAW} can be directly calculated by SAW frequency. Then I model the whole layered structure using the calculation software described in Chapter 3. I can fit the shear elastic constants of the film of interest, by comparing the calculated v_{SAW} and measured v_{SAW}. The accuracy of the obtained v_{SAW} is determined by the sensitivity.

5.1.2 Sensitivity of v_{SAW}

Since the purpose of the measurement is to fit the shear elastic constant (usually c_{44}) using the measured v_{SAW}, the sensitivity of the measurement can be defined as:

$$S = \frac{\partial \ln v_{SAW}}{\partial \ln c_{44}} = \frac{c_{44}}{v_{SAW}} \frac{\Delta v_{SAW}}{\Delta c_{44}} \tag{5.1}$$

which means the ratio between relative change of c_{44} and relative change of v_{SAW}. Higher sensitivity means relative small changes in elastic constant can lead relative big changes in v_{SAW}. With higher sensitivity, v_{SAW} is more sensitive to c_{44} and fitting of c_{44} is more accurate, given the error of v_{SAW} stays constant.

v_{SAW} is sensitive to the material on the surface within a fraction of wavelength deep. The wavelength I typically use is 300 nm. Fig. 4.10 indicates that the v_{SAW} of 700 nm SAW is mostly sensitive to the top ≈ 350 nm of the material. So when the material of interest is beyond several hundreds nanometer, v_{SAW} has the maximum sensitivity to the shear elastic constant of the material. In this case, the film is almost like bulk materials for SAW. If an Al transducer is necessary, for example when the material is transparent, the thickness of the Al thickness should be minimal (I typically use 20 nm) so v_{SAW} is mostly sensitive to the material under study instead of the Al layer.

When the film thickness is less than 300 nm, the measurement is not able to reach the maximum sensitivity, the sensitivity when the material is bulk like. In this case, one can achieve highest possible sensitivity by tuning the thickness of top Al transducer. I use the sample structure of $Al/SiO_2/Si$ to demonstrate it. The SiO_2 is a layer of thermal oxides act as the material under study. The Si is the substrate layer. Fig. 5.4 shows the sensitivity of different thickness of SiO_2 layer with different thickness of Al transducer layer on top. It shows that when the SiO_2 layer is thin, a thicker Al layer gives higher sensitivity to the shear elastic constant of SiO_2. This phenomenon can be understand qualitatively: the peak of strain energy within a SAW is not located at the top surface but slightly beneath the top surface. If the film of interest is located at where the strain energy is the highest, the highest possible sensitivity can be achieved. In Chapter 6, I plot the distribution of stress, strain, and strain energy over depth of SAW on Si. Although the distribution varies for different materials and different structures, the general phenomenon doesn't change. So the thickness of the transducer layer is decided for different cases to maximize the sensitivity.

For thin film materials with thickness much less than the SAW wavelength (100 nm or less), I find that v_{SAW} can have appreciable sensitivity to the longitudinal elastic constant which corresponds to the longitudinal acoustic wave perpendicular to the surface (usually c_{11} or c_{33}). The sensitivity is high especially when the film has small shear elastic constant. This is reasonable because for thin films the strain of SAW penetrates through the film into the layers underneath. This involves the longitudinal elastic constant.

5.1.3 Measurement of shear elastic constant of hard material

The typical thin films of hard materials or half-space with high symmetry is relatively easy to measure. In this section I use two measurements as examples. One is the measurement of shear elastic constant of VN single crystal films and the other is AlN films. Mechanical properties, especially elastic constants, serve as important indicator in thin films growth research, regarding whether the materials have good quality and how far the properties deviate from bulk values.

Materials under study [39] are signal-crystal stoichiometric VN films, grown by reactive magnetron sputtering deposition by members in Professor A. Rockett's group. The structural information is obtained by various standard instrumentation. VN has cubic symmetry with three independent elastic constants, c_{11}, c_{12}, and c_{44}. c_{11} is directly measured by longitudinal acoustic echo measurements. In this case, VN films are made with [001], [011], and [111] top surface orientations. Using the information at Table 3.1, all three elastic constants can be solved from the three measurements. However if there are concerns that different orientations can have different film properties, or more generally, not all orientations can be grown, then this method cannot give all three elastic constants. I use SAW measurement with phase-shift mask to measure v_{SAW} and further fit c_{44} of the VN films. c_{11} in the fitting process is obtained from longitudinal acoustic echo measurements. v_{SAW} has very small sensitivity to c_{12}. So c_{44} can be fitted from v_{SAW}.

I have also measured shear elastic constant of VN_x film with different x. But due to poor material characterizations, the results are not reliable. This has happened to me several times during my collaborations with other groups. For the SAW technique to accurately fit the shear elastic constants, one must have accurate characterizations of the structure, thickness, and density of the films.

In order to improve the acoustic wave filter techniques in wireless communication, it's necessary to know accurately the elastic constants of the materials involved. At the last few months of my Ph.D. I measured elastic constant of AlN film for a company developing better materials for acoustic filters. Since the materials are from the company, I cannot list detailed information. The oscillation signal looks weaker in comparison with other materials. This is possibly because that the AlN film is stiffer than most materials so the surface displacement of SAW is smaller comparing to others. Possible solutions to weak SAW signal in stiff material is to use higher power (since materials with high elastic constants usually have high thermal conductivity and steady state heating won't be an issue), or use metal transducers with low thermoreflectance coefficients so the thermal background is smaller.

AlN has hexagonal symmetry and five independent elastic constants. For thick AlN film (over 500 nm, which is the current case), v_{SAW} is mostly

sensitive to c_{44}. c_{33} can be measured using longitudinal acoustic echo technique. For other three elastic constants c_{11}, c_{12}, and c_{13}, I use bulk values as a good enough estimation in the fitting of c_{44}.

5.2 Measuring shear elastic constants of polymers

Another kind of material that is in need of elastic constant measurement is polymer. Elastic constants of polymers are difficult to measure using traditional techniques even for bulk polymers, let along polymer thin films. Elastic constants of polymers are indication of the bonding strength within polymers. For example, they can help to understand the thermal conductivity of polymers. Since polymers are usually insulators, the thermal conductance is dominated by phonon contribution. Thermal properties of various of polymers are important for their engineering applications. TDTR can be used to measure the thermal properties. Elastic constants are useful as a good estimation and understanding of the thermal properties according to Debye model. In this section I discuss several studies I have done regarding the elastic constants of spin-cast polymer films, to assist the thermal measurement performed by TDTR.

Polymers are typically treated as isotropic, although it may not be accurate especially for spin-cast polymers. It has two independent elastic constants: c_{11} and c_{44}. The longitudinal elastic constant c_{11} can be measured using longitudinal acoustic echo measurement. After obtaining c_{11}, c_{44} can be determined using SAW measurement. In the case of isotropic materials such as polymers, we have enough experimental methods to measure the full set of elastic constants.

Although in theory, a bulk like material for SAW would have the maximum measurement sensitivity to c_{44}. In reality, I find that the SAW measurement using a soft phase-shift mask is not suited for measuring SAW of bulk polymer materials. It can be understand like this: if the polymer film is very thick to be treated as bulk for SAW, then the structure looks like two soft materials that sandwich a hard Al layer. The wave is no longer generated at a surface but more like within this complicated structure.

The implication of the above observation is that there is a limitation for film thickness in the case of polymers. For hard material, there is no

limitation to the material thickness, in the sense that it won't cause the SAW measurement to fail, or in another word, SAW can always be measured. The difference is whether the sensitivity is high or low. But in the case of polymer, the thickness of the polymer needs to be carefully designed to make sure we understand the modes that are measured. Fig. 5.3 shows an example of a "failed" SAW measurement of polymer films. The very high frequency component is clearly not SAW mode of the sample structure Al/polymer/substrate. I suspect it to be some kind of vibration modes of the Al film. And it may be developed in the future to measure certain properties of hard thin films. Fortunately, most of the polymers have similar mechanical properties. So by testing on one polymer, I can obtain a guideline for other polymers.

The polymer I chose as an example is PMMA. PMMA is a well studied polymer. Fig. 5.2 is a SAW measurement map in the space of "Al thickness" and "polymer thickness", which marks the region when the SAW can be successfully measured using a phase-shift mask. The plot shows that the proper polymer thickness for the measurement is related with the Al thickness. The typical combination I use for most of the polymer studies is $100 \sim 150$ nm polymer with ≈ 120 nm Al on top. The relatively thick Al layer can also improve the sensitivity of the thin polymer film.

Another important factor in SAW measurements of polymers is how to determine the density of the polymer films. The density can be the major source of the measurement error. The density of polymers in our studies are measured by two methods: Rutherford backscattering spectrometry or quartz crystal microbalance. Note that in Rutherford backscattering spectromety (RBS), the polymer film can be easily damaged by the incoming alpha particle flux. Keep measuring the damaged spot can cause huge error in the density estimation. One way to mitigate the damaging effect is to constantly move the same during the process of RBS and don't expose one point of the polymer film to the flux longer than necessary.

Following the above mentioned guideline, shear elastic constants of various polymers [40, 41] and macromolecules [42] have been measured. In these studies, the measured elastic constants are used to understand the thermal properties of the polymer films. They also mark a very narrow region of Poisson's ratio for all kinds of polymers.

5.3 Measuring shear elastic constant of layered material

Layered materials, such as graphite and MoS_2, have received tremendous attentions in recent decades. Unique physics phenomenon can happen in a truly 2D material. Another interesting properties of the layered structure is the Van der Waals force between atomic layers. An example is that the layered materials with turbostratic disorder [43] and incommensurate interfaces [44] have been shown to have significantly small thermal conductivity. They are candidates for potential thermoelectric application [45].

The origin of the ultralow through-plane thermal conductivity is not fully understood. One explanation is that the strong anisotropy of the elastic constants causes most of the transverse acoustic phonon travel in the in-plane direction rather than the through-plane direction, which is called the phonon focusing effect [46, 47]. The strong anisotropy is due to the weak interplanar Van der Waals bonding, i.e. the small shear elastic constant c_{44} comparing with others. Quantifying c_{44} of the disordered layered materials is needed to evaluate the effect of phonon focusing.

From a different perspective, the shear elastic constant c_{44} of layered materials represents the the strength of the static friction between atomic layers without loading. The state of ultralow friction sliding is expected between atomically flat surfaces with structural incommensurability, which is referred to as "structural lubricity". However the experimental analysis of the phenomenon is challenging. c_{44} of incommensurate layered structure provides an unique tool to understand how low the friction can be between atomic interfaces due to lattice mismatch. This understanding is essential to the development of viable nanoelectromechanical systems (NEMS) using layered material, such as carbon nanotube [48, 49].

Layered materials have huge mechanical anisotropy. Using graphite as an example, c_{11} of single crystal graphite is on the order of 1000 GPa, while c_{44} is measured to be around 5 GPa. This huge anisotropy poses difficulties in the traditional experiment techniques for shear elastic constants measurement. In this section, I first describe the measurements of shear elastic constant of common layered materials, graphite and MoS_2, to demonstrate the capability of the SAW technique with phase-shift mask. Then I describe the measured ultrasmall shear elastic constant of misfit layered compound.

5.3.1 Shear elastic constant measurement of graphite and MoS_2

The graphite and MoS_2 flakes are exfoliated from the highly ordered pyroliytic graphite and natural single crystal MoS_2, respectively. They are exfoliated on top of SiO_2/Si wafer with 300 nm SiO_2 layer. The exfoliation process is standard and relatively easy since I am not looking for single layer or few layer flakes. The flakes only need to be bigger than the spot size of the laser. The length scale of the flake I typically use is on the order of 100 µm. The thicknesses of the flakes are measured by AFM.

Due to the weak bounding between layers, if SAW measurements are done on the layered materials with conventional PDMS phase-shift mask, the sticky PDMS can easily peel off some atomic layers together with the sputtered Al film on top. To solve this problem, one can use a hard PDMS phase-shift mask just like the hard PDMS stamp described in nano-imprint lithography. The hard PDMS is much less sticky than the conventional PDMS so it does not peel off the atomic layers. The downside of hard PDMS mask is the mask does not easily attach to the sample surface. One may need to push the hard PDMS mask with a tweezer to establish a good contact between the mask and the sample.

Following the thin film measurements that discussed before, for exfoliated flakes with thickness on the order of 100 nm, I sputter relatively thick Al (around 120 nm) on top to increase the sensitivity. The longitudinal acoustic echo measurement is performed at the same time to measure c_{33}. For layered structure, v_{SAW} can be very sensitive to c_{33} so an accurate measurement of film thickness and c_{33} is necessary. There are five independent elastic constant in a hexagonal crystal. v_{SAW} is typically not sensitive to c_{11}, c_{12}, and c_{13}. One can use a good estimation or result from density functional theory, as I did in the following measurement, to fit c_{44}.

$\approx$ 170 nm thick MoS_2 flake is exfoliated on SiO_2-on-Si substrate with 300 nm SiO_2. The thickness of MoS_2 is measured by AFM. Al layer of $\approx$ 135 nm is sputtered on top of MoS_2. The measured and calculated elastic constants are compared with prior results in Table 5.1. Both calculation and experiment agrees quite well with prior results.

Table 7.1 lists my measurement result for HOPG graphite and Table 7.2 is a more complete comparison between results of MoS_2 single crystal. These

Table 5.1: Measured and calculated elastic constants of MoS_2 and comparison with prior calculation and experiment.

	a(Å)	c(Å)	c_{11}(GPa)	c_{12}(GPa)	c_{13}(GPa)	c_{33}(GPa)	c_{44}(GPa)
DFT Calculation	3.16	12.05	223	49.9	6.52	51.8	16.9
Measurement						54.1	15.4
Volkova Cal [50]	3.18	12.35	214	58		56	18
Feldman Exp [51]			238	-54	23	52	18.6

measurements on the small exfoliated flakes further demonstrate the capability of SAW technique with phase-shift mask.

5.3.2 Shear elastic constant measurement of misfit layered compound $[SnSe]_n[MoSe_2]_n$

In this section, I present experimental studies of the incommensurate layered material (misfit layered compound, MLC) $[SnSe]_n[MoSe_2]_n$, $n = 1 \sim 4$ to quantify its shear elastic constant c_{44}.

The $[SnSe]_n[MoSe_2]_n$ thin films is prepared by collaborators in Professor David C. Johnson's group at University of Oregon. They did the structural characterizations of the film. I did elastic constants measurements and DFT calculation. The films are synthesized on Si (100) substrate using the modulated elemental reactants (MER) method described previously [52]. n bilayers of Sn and Se with 1:1 atomic ratio is deposited onto Si (001) substrate followed by n bilayers of Mo and Se with 1:2 atomic ratio. This sequence is repeated to reach the desired thickness ($\sim$ 60 nm). After the deposition, the precursor film is annealed for 20 minutes on a hot plate at 400 ℃ in a N_2 environment ($<$ 1 ppm O_2) to form the MLC of $[SnSe]_n[MoSe_2]_n$. For comparison, single component $MoSe_2$ thin film with disordered layered structure is also synthesized by the same approach.

The thickness of the film is measured by specular X-ray reflectivity (XRR). The average film compositions are obtained from X-ray fluorescence (XRF). The in-plane lattice constant and grain size is measured by in-plane X-ray diffraction (XRD). The c axis lattice constant in through plane direction is measured by XRD. High-angle annular dark field scanning transmission electron microscopy (HAADF STEM) is used to verify the quality of the film.

The measured in-plane and through-plane structural information of

Table 5.2: Structural information of $[SnSe]_n[MoSe_2]_n$ with $n = 1 \sim 4$

n	Film Thickness (nm)	SnSe a (nm)	MoSe2 a (nm)	c (nm)	Misfit Coefficient	Sn/Mo Ratio
1	59.8(10)	0.6014(1)	0.331(1)	1.251(1)	1.06(1)	1.09(1)
2	58.9(7)	0.6057(3)	0.3334(3)	2.497(2)	1.06(1)	1.10(1)
3	57.6(7)	0.605(1)	0.3329(2)	3.752(3)	1.05(1)	1.11(1)
4	57.0(6)	0.607(1)	0.3322(4)	4.951(5)	1.04(1)	1.13(3)

$[SnSe]_n[MoSe_2]_n$ is listed in Table 5.2. The XRD scan suggests the precursor crystallized into a layered film with strong crystallographic alignment to the substrate. Both the c-axis and the in-plane lattice parameters of repeating unit of each sample are consistent with previously reported values [52]. The XRR scans indicate the samples are high quality with low interface roughness. Based on derivation of Wainfan and Parratt [53], the film roughness is less than 0.6 nm. The incommensurate in-plane lattice parameters suggests that there is no epitaxial relationship between layers. The ratio of the in-plane areas for the two constituents provides the structural misfit ratio. We also obtain crystallite sizes from the peak width of in-plane XRD scan. Neglecting strain effects, which are usually negligible in MER-prepared compounds [52, 54], Scherrer analysis indicates that the SnSe grain size increases from 3.5 nm for $n = 1$ to 7.5 nm for $n = 4$ and the $MoSe_2$ grain size increases from 3.3 nm for $n = 1$ to 3.9 nm for $n = 4$.

HAADF STEM is performed to verify structural information. HAADF STEM images of $n = 1$ and $n = 4$ samples are shown in Fig. 5.5. It supports that the samples are crystallographically aligned to the substrate and consist of alternating n layers of SnSe interleaved with n layers of $MoSe_2$. The total film thickness is confirmed to be the same as determined from analysis of XRR. There is no apparent relationship between the alignment of grains within one layer and the alignment of grains within an adjacent layer, showing the turbostratic disorder characteristic. The $MoSe_2$ layers are disordered even within each block. The turbostratic disordering of adjacent dichalcogenide layers prepared by MER was observed previously and is correlated with the ability of the dichalcogenide to form multiple stacking arrangement [55, 56].

The $[SnSe]_n[MoSe_2]_n$ thin film is treated as an effective medium with textured symmetry in the measurement length scale ($0.7 \sim 20$ µm). It has five independent elastic constants: c_{11}, c_{12}, c_{13}, c_{33}, and c_{44}. I measure c_{33} using longitudinal acoustic echo [24] and c_{44} using SAW technique [38].

v_{SAW} is generally sensitivity to the shear elastic constant. I calculate

v_{SAW} of layered structure using the calculation methods described in Chapter 3 to extract the shear elastic constants by fitting the calculated v_{SAW} to the measured v_{SAW}. The sensitivity of v_{SAW} to elastic constant c is defined as: $(\partial v_{SAW}/\partial c)(c/v_{SAW})$, in current sample structure Al($\approx$ 145 nm)/MLC($\approx$ 60 nm)/Si, the sensitivity of v_{SAW} to c_{33} of MLC is about 0.11; the sensitivity to c_{44} is about 0.03; the sensitivity to c_{11} is about 0.01, while the sensitivities to c_{12}, and c_{13} are less than 0.001. c_{33} can be measured independently in longitudinal acoustic echo measurement. c_{44} has the highest sensitivity other than c_{33} so I can use v_{SAW} to extract c_{44}. In order to do it, the estimates of c_{11}, c_{12}, and c_{13} are needed as input parameters. In Chapter 7, I describe how I use density functional theory (DFT) calculation to compute c_{11}, c_{12}, and c_{13} of a hexagonal crystal.

Since $[SnSe]_n[MoSe_2]_n$ is incommensurate with misfit coefficient slightly larger than 1, it is impractical to perform DFT calculation for the true supperlattice. For cases of $n > 1$, there are two many atoms in the cell and the calculation is too time demanding. So I only calculate $[SnSe]_1[MoSe_2]_1$ using a supercell consisting of 1 atomic layer of 3 $MoSe_2$ unit cell and 1 atomic layer of 4 SnSe unit cell. Comparing with the lattice constants measured in XRD, the relaxed supercell has $\sim 1\%$ in-plane strain in $MoSe_2$ layer and $\sim 5\%$ in-plain strain in SnSe layer. We assume the strain is small enough that the result of c_{11}, c_{12}, and c_{13} are good enough estimations. The results of DFT calculation are listed in Table 5.3. To extract c_{44} of MLC of different n from SAW experimental results, I use measured c_{33} with corresponding n and calculated c_{11}, c_{12}, and c_{13} with $n = 1$.

In the measurement of elastic constants, I discovered that the measured v_{SAW} of $n = 4$ sample is too small that I cannot fit a c_{44} from it. Later I collected XRD signal from the samples that I use to measure SAW. The results show that many XRD peaks in the $n = 4$ samples disappeared while the XRD signal for $n = 1 \sim 3$ are similar to the one collected immediately after synthesis at University of Oregon. This lead us to believe that the quality of $n = 4$ sample is no longer as good as when it was synthesized and we can no longer trust its structural information and we can no longer fit c_{44} from v_{SAW}. The cause of the degradation and resulting structure of the $n = 4$ sample is currently unclear. It is possibly caused by the fact that the storage environment is not always under good vacuum. It also shows that the samples with bigger n are easier to degrade. The measured c_{33} and c_{44}

Table 5.3: Calculated and measured elastic constants of $[SnSe]_1[MoSe_2]_1$. c is measured by XRD; c_{33} is measured by longitudinal acoustic echo measurement; c_{44} is measured by SAW measurement.

	c(Å)	c_{11}(GPa)	c_{12}(GPa)	c_{13}(GPa)	c_{33}(GPa)	c_{44}(GPa)
DFT Calculation	12.458	109.4	40.5	4.5	48.3	4.1
Measurement	12.425				38.8	1.0

Table 5.4: Comparison of measured elastic constants of turbostratic $MoSe_2$ synthesized by MER method and calculated elastic constant of bulk $MoSe_2$.

	c_{11}(GPa)	c_{12}(GPa)	c_{13}(GPa)	c_{33}(GPa)	c_{44}(GPa)
Turbostratic, Exp.				33	3
Bulk crystal, Cal. [57]	196.1	44.7	9.8	44.7	32.9

of other three samples are plotted in Fig. 5.6.

The 2% error of c_{33} is dominated by error in echo measurement, since both layer thickness and density are relatively accurate. The total error in c_{44} is $\approx 30\%$, which is dominated by the error in c_{33} and measured frequency of SAW. Since the sensitivity to c_{33} is ≈ 4 times of the sensitivity to c_{44}, $\approx 2\%$ error in c_{33} leads to $\approx 8\%$ error in c_{44}. We assume the uncertainty of c_{11} is about 5% from the comparison of calculation and experiment of MoS_2, it contributes to $\approx 2\%$ error in measurement of c_{44}. So the error from c_{11} is dominated by error from other sources. The relatively large error in c_{44} comparing with our other measurements using the same technique is because the c_{44} of $[SnSe]_n[MoSe_2]_n$ is extremely small so the v_{SAW} is more sensitive to c_{33} than to c_{44} and the overall sensitivity to the film is small because of the relatively small thickness.

The results show that c_{44} of $[SnSe]_n[MoSe_2]_n$ decreases with increasing n. At $n = 1$, there is no turbostratic disorder in $MoSe_2$ layer since there is only 1 atomic layer, and only incommensurate interfaces exist. As n increases, more turbostratic disorder is introduced in $MoSe_2$. To evaluate the how much c_{44} can decrease due to turbostratic disorder, we measured c_{33} and c_{44} of turbostratic $MoSe_2$ synthesized by MER method. Table 5.4 compares the measured elastic constants of turbostratic $MoSe_2$ and calculated elastic constants of single crystal $MoSe_2$. It shows c_{44} of $MoSe_2$ with turbostratic disorder decreased by about 90% from its bulk value. Savini *et al.* [58] calculated the elastic constants of graphite with turbostratic disorder and show that c_{44} can drop to the order of 0.1 GPa, which is on the same order of

magnitude of our measurements.

Also when $n = 1$, I suspect it is easier for the SnSe layer to arrange itself so that the Sn atoms are nested between Se atoms in the $MoSe_2$ layer. When n is larger, the SnSe layer is better crystallized and the nesting effect is less than before. The fact that grain size of SnSe is doubled from $n = 1$ to $n = 4$ is an evidence of it.

5.4 Figures

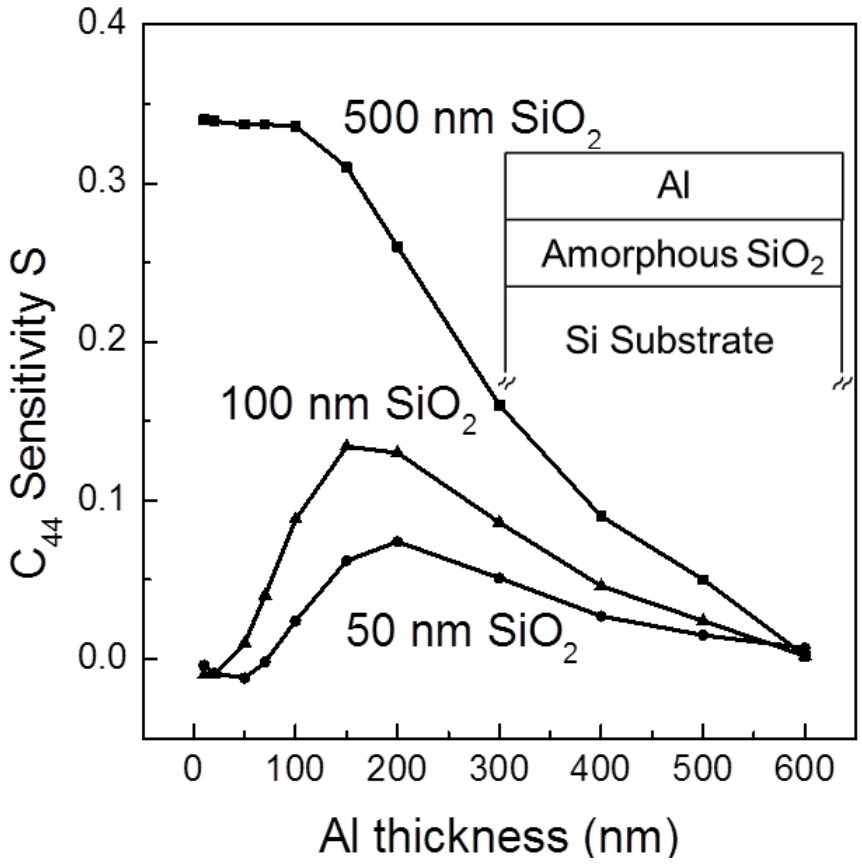

Figure 5.1: Sensitivity of shear elastic constant c_{44} of the SiO_2 with different thickness of SiO_2 layer. For thin films, a thicker Al layer on top can increase the sensitivity.

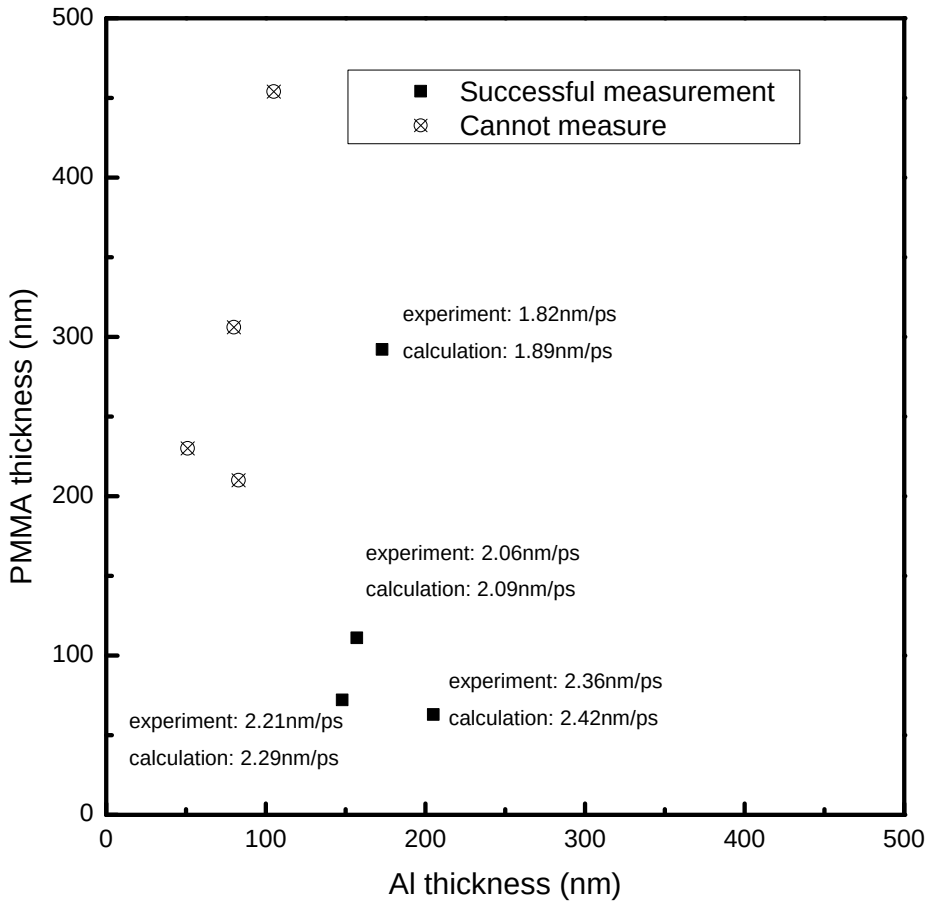

Figure 5.2: Map of successful and unsuccessful measurement of Al/PMMA/Si sample structure with different Al thickness and PMMA thickness. The elastic constants of PMMA can be found in Ref. [40]

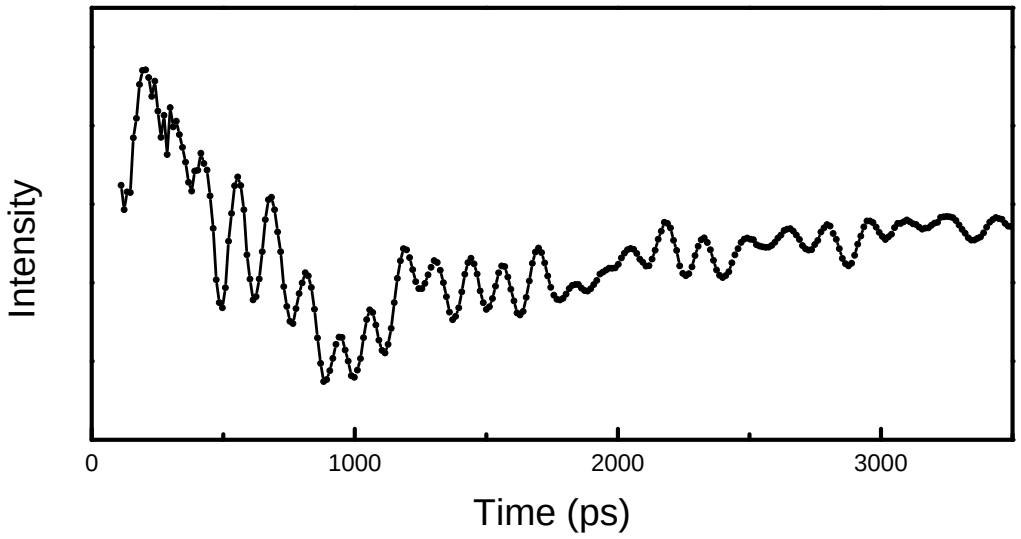

Figure 5.3: Signal of the structure Al(80nm)/PMMA(306nm)/Si with the phase-shift mask. The high frequency component is clearly not the SAW mode of the layered structure. It's possibly the oscillation mode of a "suspended" Al film.

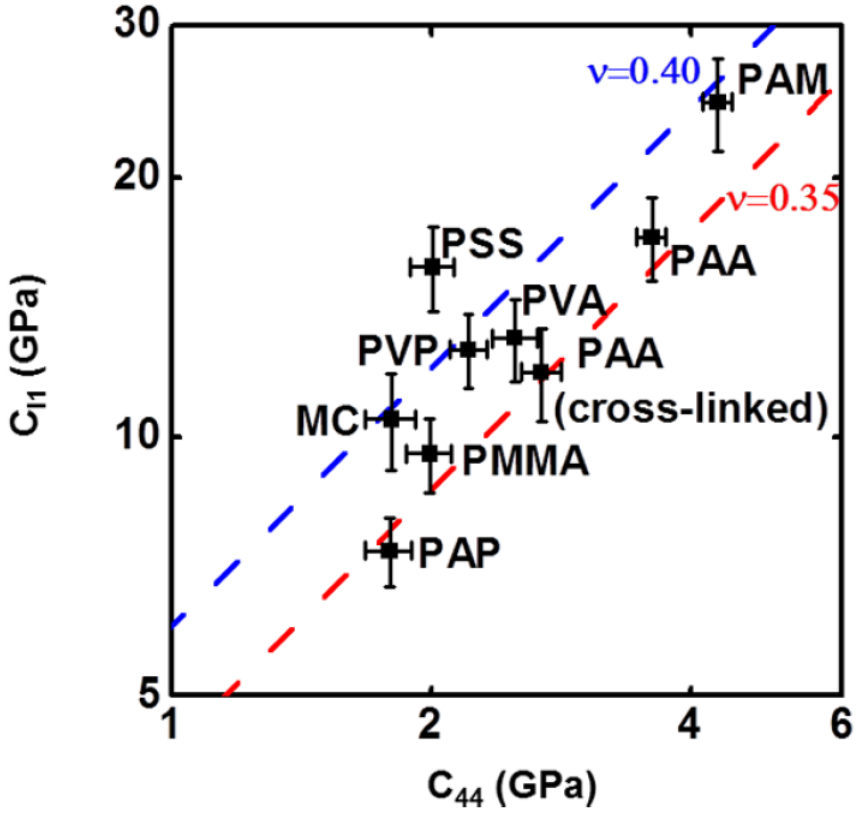

Figure 5.4: Measured c_{11} and c_{44} of various polymers. The blue and red lines mark the narrow region of their Poisson's ratio.

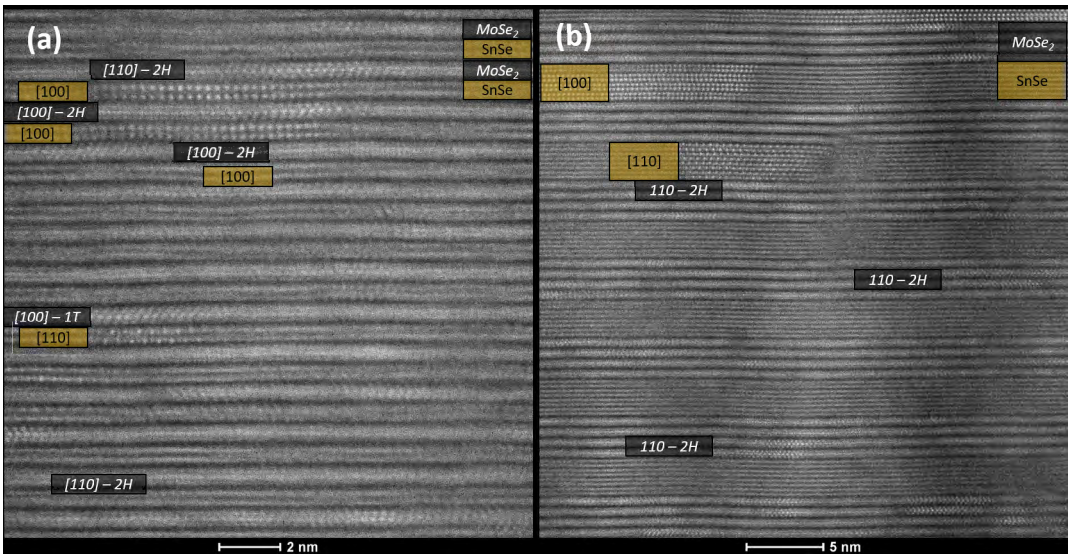

Figure 5.5: STEM image of $[SnSe]_n[MoSe_2]_n$ with $n = 1$ (figure (a)) and $n = 4$ (figure (b)).

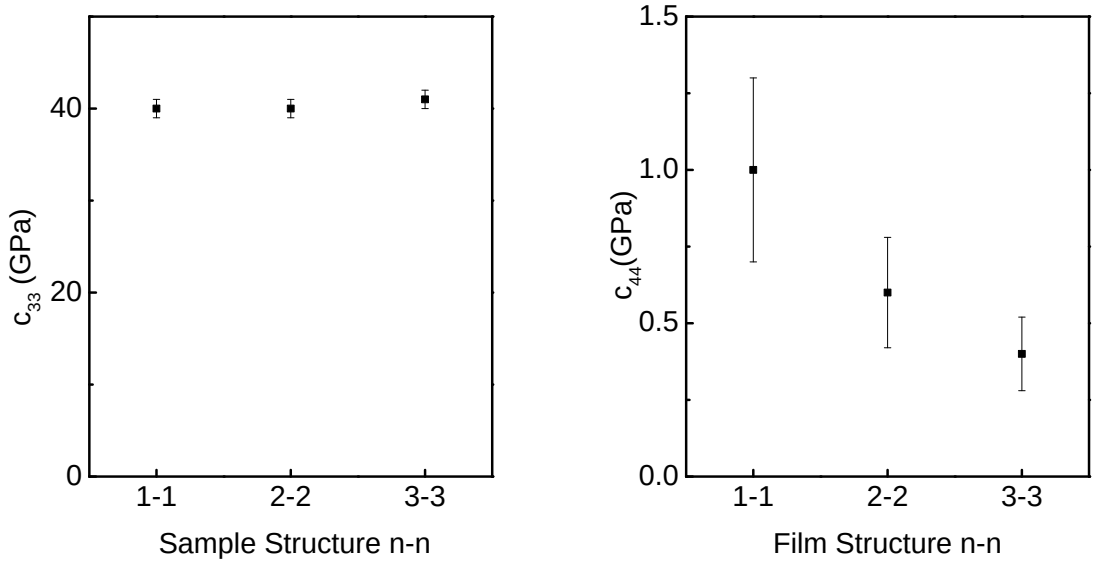

(a) (b)

Figure 5.6: (a) Measured c_{33} of $[SnSe]_n[MoSe_2]_n$ with different n by longitudinal acoustic echo method. (b) Measured c_{44} of $[SnSe]_n[MoSe_2]_n$ with different n by SAW measurement.

CHAPTER 6

ATTENUATION OF 7 GHZ SURFACE ACOUSTIC WAVE ON SILICON

Most of this chapter was published in Ref. [59].

6.1 Acoustic attenuation in non-metallic crystals

In non-metallic crystals, the intrinsic attenuation of acoustic waves is governed by the interactions with thermally excited phonons mediated by the anharmonicity of the interatomic potentials [60]. This intrinsic attenuation imposes an upper limit to the quality factor Q of mechanical oscillators, where Q is defined as 2π times the ratio between total stored energy and energy dissipated per cycle of oscillation. The widely used mechanical oscillators like microelectromechanical systems (MEMS) and nanoelectromechanical systems (NEMS) can now operate at GHz frequencies. High Q factors are needed for their applications as filters and sensors [61, 62, 63]. Near room temperature, the Q is typically limited by multi-phonon relaxation process where the strain of the acoustic wave disturbs the distribution of thermally excited phonons and the relaxation of the distribution to an equilibrium requires an increase of entropy and therefore causes dissipation of energy from the acoustic wave.

Acoustic attenuation by the relaxation of the thermal phonon distribution was first proposed by Akhiezer [64] under the constraint $\omega\tau \ll 1$, where ω is the angular frequency of acoustic wave and τ is the time scale over which the distribution of thermally excited phonons relaxes to a local equilibrium, i.e., the average phonon relaxation time. The theory was later extended using Boltzmann theory [65, 66, 60] to higher acoustic wave frequencies, $\omega\tau > 1$. Maris [60] pointed out that the Akhiezer theory, or the Boltzmann theory, should be applicable when $\omega \ll k_B T/\hbar$ and $\omega\tau \not\gg 1$ is satisfied. Throughout the paper we will call the attenuation from relaxation

of thermally excited phonon at this frequency regime "Akhiezer damping". This definition of the range of applicability of Akheizer theory is less restrictive than the limit $\omega\tau \ll 1$ which is referred to as the Akhiezer regime in much of the scientific literature on this topic.

A simplified expression for the acoustic attenuation α due to Akhiezer damping is [67, 68, 69, 70]:

$$\alpha = \frac{CT}{2\rho v^3}\frac{\omega^2\tau}{1+\omega^2\tau^2}(\langle\gamma^2\rangle - \langle\gamma\rangle^2) \tag{6.1}$$

where C is the volumetric heat capacity, ρ is density, v is the speed of acoustic wave, and γ is the mode Grüneisen parameter of the thermally excited phonons; γ depends on frequency and polarization of the phonon and the mode of the strain. The brackets in Eq. 6.1 denote an average over the entire population of thermally excited phonons. In Sec. 6.4 we discuss the condition when Eq. 6.1 is a good approximation to Boltzmann theory.

At low frequencies, $\omega^2\tau^2 \ll 1$, Eq. 6.1 has a simple quadratic dependence on the frequency of the acoustic wave [60, 65]:

$$\alpha = \frac{CT}{2\rho v^3}\omega^2\tau(\langle\gamma^2\rangle - \langle\gamma\rangle^2) \tag{6.2}$$

This relationship can also be described by a phenomenological equation [71, 72]:

$$\alpha = \omega^2\eta/2\rho v^3 \tag{6.3}$$

where η is the effective phonon viscosity. For bulk acoustic wave, η can be calculated by the phonon viscosity tensor [72], which has the same symmetry as the elastic constant tensor of the material. Comparing Eq. 6.2 and Eq. 6.3, η contains information of both τ and mode Grüneisen parameters and depends on the mode (normal or shear), polarization, and direction of propagation of the acoustic wave. The ideal quality factor Q of an acoustic wave is $Q = \omega/(2\alpha v)$. Therefore, based on Eq. 6.3, the fQ product is independent of frequency; fQ is often used as a figure of merit [73] for mechanical oscillators.

The highest frequencies achieved in previous studies [74, 75, 76, 67, 77, 78] of attenuation of acoustic wave in Si at room temperature is ≈ 2

GHz. If we estimate $\tau \sim 20$ ps [25], then $\omega\tau \sim 0.2$ and it adequately satisfies the condition $\omega^2\tau^2 \ll 1$. Therefore, in the previous work, Eq. 6.3 is a good approximation, α has a quadratic dependence on frequency, and the effective phonon viscosity can be obtained from the proportionality between attenuation and ω^2. As I discuss below, previous results for the attenuation of acoustic waves in Si show significant discrepancies. Similarly, data for the phonon viscosity tensor also have large discrepancies [72, 75].

None of the previous studies of Si near RT are at frequencies high enough to separate τ and the mean-square variations in the mode Grüneisen parameters that appear in Eq. 6.1. When acoustic wave in Si is at several hundreds MHz and experiment is done at temperature much lower than Debye temperature, $\omega\tau \sim 1$ is satisfied [67, 68] and Eq. 6.1 has been used to describe the low temperature measurements. At low temperatures, only a small fraction of the phonon modes in acoustic branches are thermally excited. Since the majority of phonon modes of Si are thermally excited at RT, the low temperature measurements cannot be reliably extrapolated to RT.

Daly *et al.* [25] recently used Eq. 6.1 to characterize the attenuation of longitudinal acoustic wave in Si when $\omega\tau \sim 1$. At RT, the measured attenuation at 50 GHz and 100 GHz is consistent with the assumption of $\langle\gamma^2\rangle - \langle\gamma\rangle^2 = 1$ and fitting of the data with $\tau \approx 20$ ps. Since both the relaxation of thermal phonon and the Grüneisen parameters are dependent on the acoustic mode, the purpose of the present study is to better understand the Akhiezer damping of acoustic modes with predominately *transverse* polarization when $\omega\tau \sim 1$ at RT. When Eq. 6.1 is applicable, Q reaches minimum at $\omega\tau = 1$. I use the temperature dependence of the attenuation in the regime $\omega\tau \sim 1$ to derive estimates of both the thermal phonon lifetime τ and the mean-squared variation of the Grüneisen parameters.

An elastically aniostropic metal film can be used to generate high frequency transverse acoustic wave through heating by a short duration optical pulse but the efficiency is relatively low [79]. So I have chosen instead to use a more experimentally convenient approach of measuring the attenuation of surface acoustic waves (SAWs). I show in Sec. 6.3.1 that the attenuation of SAWs can be connected to Akhiezer damping of bulk transverse acoustic waves. Since pure shear strain in cubic crystal like Si does not suffer from thermoelastic damping, I can safely ignore thermoelastic damping in our analysis.

Together with the phase-shift mask technique, I have described three technique to measure SAW in optical pump-probe system. As discussed before, to detect propagating SAW in a transient grating experiment involves mixing the scattered wavefront with a carrier, i.e., heterodyne detection [80]. This require complicated optical setup, especially if one wants to measure SAW traveling far away. SAW measurement using a elastomeric phase-shift mask is a convenient method for measurement of elastic constants of thin layers. Unfortunately, however, the elastomeric mask in contact with the sample produces strong damping and an attenuation length on the order of 10μ m. It leaves with only one option: measure SAW with patterned metal grating. Typically, the pattern of metal bars attenuates the SAW significantly by coupling the SAW to bulk acoustic modes, as we discuss in Sec. 6.3. By spatially separating the gratings used to generate and detect the SAW, I can minimize and quantify damping created by the grating and probe the intrinsic acoustic attenuation.

The attenuation of SAWs in the context of SAW devices has been discussed previously by Slobodnik *et al.* [81, 82]. This study provides additional analysis of the intrinsic and extrinsic damping of SAWs.

6.2 Generation and Detection of SAWs Using a Metal Grating

6.2.1 Sample Fabrication

The sample structure is shown in Fig. 6.1. I will discuss later the reason for this geometry. Mircofabrication of the structure consists of two main steps. First, I define the gap region by standard liftoff techniques. AZ-5214E photoresist is used in image reversal mode to cover the gap region and form a negative wall profile. Then, a thin Al layer ($\sim$ 15 nm) is sputtered onto the sample surface. After deposition, the photoresist pattern together with the Al film is lifted off by acetone, leaving the gap region uncovered by Al. Second, I define the Al grating by nano-imprint lithography described in Chapter 2.

6.2.2 Generation and detection scheme

Generation and detection of SAWs by optical pump-probe techniques has been discussed previously [83]. When the pump optical pulse arrives at the sample surface, the temperature of Al bars rises quickly while the temperature of Si substrate remains relatively unchanged. The expansion of Al causes spatially modulated stress and generates SAWs. The amplitude of SAWs is therefore proportional to the temperature rise of the Al, which is proportional to the average power of the pump beam.

In many experiments that probe SAWs optically, SAWs scatter light due to surface displacements rather than elasto-optic coupling [84]. For the specific case of the Al grating structure, the electric field reflected by the Al regions of the sample are larger than the electric field reflected from the bare Si regions of the sample. The perpendicular displacements of the Al bars are in phase with each other when the wavelength of SAW is equal to the periodicity of the Al grating. The modulation of the reflected electric field is therefore linear in the displacements and the modulation of the reflectivity is proportional to the SAW amplitude. By contrast, the scattering cross section of SAWs on a grating-free surface is quadratic in the SAW amplitude [84]. In the experiments, the amplitude of the detected signal scales linearly with the pump power, as expected.

In our pump-probe system, the laser has repetition rate of ≈ 74 MHz. Each pump pulse excites a SAW wavepacket. The probe can be delayed relative to the pump by up to ≈ 4 ns. Each probe pulse can detect SAW wavepackets generated by any previous pump pulse; for example if the delay line is set to 2 ns, then the probe pulses can detect SAW that have propagated for 2 ns, 16 ns, 30 ns, 44 ns, etc. This is the "accumulation" effect that I briefly mentioned in Chapter 2. I use spatially separated pump and probe optical pulses to detect SAW that have propagated relatively long distances to increase the sensitivity of the experiment to the intrinsic SAW attenuation.

I label the pump pulse that is split off from the given probe pulse as pump pulse $n = 0$, the prior pump pulse to be $n = -1$, the pulse before that to be $n = -2$, etc. We modulate the pump beam at ≈ 9.3 MHz (1/8 of the laser repetition rate) and synchronously detect the modulation of the reflected probe intensity with a fast photodiode and rf lock-in amplifier. Detection of the SAW wavepacket generated by pump pulse n has a $\approx -n\pi/4$

phase difference with respect to the reference signal.

Sec. 6.3.3 discusses how the grating structure with non 50% filling factor creates a band gap at Brillouin zone center. Since I cannot make the grating with exactly 50% filling factor, there is always a small band gap at the Brillouin zone center. This band gap produces components with small group velocity. These minor components of the signal will trail behind the wave packet. Each response to a pump optical pulse is overlapped by the trailing part of the response to the previous pump pulse because the current response can catch up with the low group velocity component of the previous response.

To measure attenuation, we need to separate the responses; the phase shifts described above help accomplish that task. When the spatial offset between the pump and probe beam is set at ≈ 150 µm, which corresponds to the position of SAW packets generated by pump pulse $n = -2$. The signal has a $\pi/2$ phase shift and appears only in the out-of-phase channel. The response from pump $n = -3$ will appear in both the in-phase and out-of-phase channel. Since we observe that the in-phase signal is negligible compared to the out-of-phase signal, we conclude that the out-of-phase signal is not significantly contaminated by a contribution from pump $n = -3$.

Fig. 6.3a shows the typical signal for a small offset between pump and probe and Fig. 6.3b shows the typical signal for a large offset. By comparing the amplitude of the Gaussian wave packet as a function of beam offset, we can determine the attenuation.

6.3 Properties of SAW on Silicon with metal grating

The difficulty of this attenuation measurement is that the intrinsic attenuation is very small comparing to other possible factors that can cause wave intensity change. A reliable measurement requires consideration and correction for additional mechanisms that cause the wave amplitude to change with distance of propagation. In the following sections I will discuss the effect of the mass of the Al grating and diffraction of the acoustic wave.

6.3.1 SAW on Si (100) plane

Using a Green's function method described in Chapter 3, I calculate the dispersion of SAWs of the bare substrate and the substrate patterned with a thin metal grating. I define Cartesian axis where axis $\hat{a}_1$ and $\hat{a}_2$ are in the plane of surface and axes $\hat{a}_3$ is perpendicular to the surface. $G_{ij}(k, \omega, x_3)$ is the elastodynamic Green's function tensor in Fourier space (angular frequency and wave vector) evaluated at depth x_3. $G_{33}(k, \omega, x_3 = 0)$ is its $(3, 3)$ component, which is at surface $x_3 = 0$ and represents the perpendicular displacement (in the $\hat{a}_3$ direction) with excitation force at $\hat{a}_3$ direction. $G_{33}(k, \omega, x_3 = 0)$ has the information of dispersion relation of SAW, which can be used to calculate SAW velocity.

The measurements are on the Si (100) surface. For a cubic crystal, SAWs propagating along the $\langle 100 \rangle$ or $\langle 110 \rangle$ direction are Rayleigh surface acoustic waves (RSAW); i.e., the sagittal plane of SAWs is perpendicular to the surface [6]. For Si(001), as the propagation direction of the SAW rotates from $\langle 100 \rangle$ to $\langle 110 \rangle$, the SAW is a Rayleigh-like wave and it gradually converts into the bulk transverse wave with polarization parallel to the surface. The sagittal plane is no longer perpendicular to the surface but there is no wave energy radiating into substrate. At directions close to $\langle 110 \rangle$, there is very small or no displacement perpendicular to the surface in the Rayleigh-like wave and it can no longer be measured in our experimental set up. Beyond $\approx 37^\circ$ from $\langle 100 \rangle$, another mode called pseudo surface acoustic wave (PSAW) [7] arises. The PSAW has a wave component that radiates into the bulk. At $\langle 110 \rangle$ direction, the radiating component disappears and the wave becomes RSAW again. What we measured is at $\langle 110 \rangle$ and it belongs to the PSAW branch. To simplify the terminology in what follows, I use the term SAW to describe both PSAWs and SAWs. Fig. 3.3 shows the the different SAW modes propagating at different direction on Si (001) surface.

I calculate the SAW velocity (v_{SAW}) using elastic constants of Si [85]: $c_{11} = 167.4$ GPa, $c_{12} = 65.2$ GPa $c_{44} = 79.6$ GPa, and density $\rho = 2.33$ g/cm^3. At $\langle 110 \rangle$ direction where the measurement are carried out, $v_{\mathrm{SAW}} = 5.09$ nm/ps. SAW in our experiment has 700 nm wavelength. Thus, the predicted frequency is $f = 7.27$ GHz or, equivalently, an angular frequency of $\omega = 45.7$ s^{-1}. Experimentally, I observe $f = 7.17$ GHz. I attribute the 1.3% difference to the mass of the patterned Al grating. From linear

response theory, $\mathrm{Im}(G_{33}(k_\parallel, \omega, x_3 = 0))$ arises because of dissipation. The width of $\mathrm{Im}(G_{33}(k, \omega, x_3 = 0))$ in the frequency coordinate can be used to infer the quality factor Q of the SAW created by coupling to bulk acoustic waves. From the calculations, I find that for a propagation direction within 5° of $\langle 110 \rangle$ direction, the Q factor is $> 3 \times 10^4$ due to radiation of acoustic energy into the bulk and therefore I can neglect this mechanisms for attenuation of the PSAW.

I calculate the symmetric strain tensor ϵ_{ij} with $i, j = 1, 2, 3$ in SAW at the (100) plane and propagating in the $\langle 110 \rangle$ direction. The amplitude of the density of elastic energy is $E_{el} = \frac{1}{2} c_{ijkl} \epsilon_{ij} \epsilon^*_{kl}$. The strain is represented by complex number and * stands for complex conjugate. For cubic crystals, the nine components of the symmetric strain tensor can be viewed as the basis of the representation of the group which is the symmetrized product of the point group of the cubic crystal [86, 87, 88]. The resulting group is reducible; therefore, the six independent components of strain tensor can be recombined to form the new basis of the three irreducible representations. The volumetric strain mode $\epsilon_v = \epsilon_{11} + \epsilon_{22} + \epsilon_{33}$ corresponds to the the bulk modulus $c_B = (c_{11} + 2c_{12})/3$; The two equivalent stretch modes $\epsilon_2 = \epsilon_{11} - \epsilon_{22}$ and $\epsilon_3 = (2\epsilon_{33} - \epsilon_{11} - \epsilon_{22})/\sqrt{3}$ correspond to tetragonal shear modulus $(c_{11} - c_{12})/2$; and three equivalent shear modes ϵ_{12}, ϵ_{13}, and ϵ_{23} correspond to shear modulus c_{44}. The density of elastic energy in a cubic crystal is then [89, 88]:

$$E_{el} = \frac{1}{2} c_B |\epsilon_v|^2 + \frac{c_{11} - c_{12}}{4} (|\epsilon_2|^2 + |\epsilon_3|^2) + 2c_{44} (|\epsilon_{12}|^2 + |\epsilon_{13}|^2 + |\epsilon_{23}|^2) \quad (6.4)$$

When $\omega^2 \tau^2 \ll 1$ is satisfied, the concept of phonon viscosity can be applied to calculate the Akhiezer damping of SAW as described by Maris [90]. I adopt part of Maris's approach and provide a brief derivation of the effective viscosity of SAW in the following. The average rate of energy loss P_v due to phonon viscosity is [90]:

$$P_v = \frac{1}{2} \omega^2 \int \eta_{ijkl} \epsilon_{ij} \epsilon^*_{kl} \, \mathrm{d}V \quad (6.5)$$

where η_{ijkl} is the phonon viscosity tensor and the integral is over volume. The total energy of the SAW is the same as the amplitude of the elastic energy, since the time average of elastic energy and kinetic energy is the

same. Therefore, the total energy of the system is:

$$W = \int E_{el}\,\mathrm{d}V \tag{6.6}$$

Since the phonon viscosity tensor η_{ijkl} has the same symmetry as elastic constants tensor c_{ijkl}, the average rate of energy loss by Akhiezer damping in Si is:

$$P_v = \int \omega^2 \left[\frac{1}{2}\eta_B|\epsilon_v|^2 + \frac{\eta_{11}-\eta_{12}}{4}(|\epsilon_2|^2+|\epsilon_3|^2) + 2\eta_{44}(|\epsilon_{12}|^2+|\epsilon_{13}|^2+|\epsilon_{23}|^2)\right]\mathrm{d}V \tag{6.7}$$

where $\eta_B = (\eta_{11}+2\eta_{12})/3$. By writing the attenuation coefficient as:

$$\alpha_{\mathrm{SAW}} = \frac{P_v}{2W v_{\mathrm{SAW}}} = \frac{\omega^2\eta_{\mathrm{SAW}}}{2\rho v_{\mathrm{SAW}}^3} \tag{6.8}$$

the effective viscosity of SAW can be defined as:

$$\eta_{\mathrm{SAW}} = \frac{\rho v_{\mathrm{SAW}}^2}{2W}\int \left[\eta_B|\epsilon_v|^2 + \frac{\eta_{11}-\eta_{12}}{2}(|\epsilon_2|^2+|\epsilon_3|^2) + 4\eta_{44}(|\epsilon_{12}|^2+|\epsilon_{13}|^2+|\epsilon_{23}|^2)\right]\mathrm{d}V \tag{6.9}$$

For SAW on the Si (100) surface along the $\langle 110\rangle$ direction, the effective viscosity is:

$$\eta_{\mathrm{SAW}} = 0.059\eta_B + 0.269\left(\frac{\eta_{11}-\eta_{12}}{2}\right) + 0.545\eta_{44} \tag{6.10}$$

η_{44} is the effective viscosity of fast transverse (FT) bulk acoustic wave in the $\langle 110\rangle$ direction; $(\eta_{11}-\eta_{12})/2$ is the effective viscosity of slow transverse (ST) bulk acoustic wave in the $\langle 110\rangle$ direction. Thus, the SAW attenuation in our measurements has predominantly shear character.

6.3.2 Diffraction and phonon focusing

SAW is generated by pump laser beam with $1/e^2$ spot size of $w_0 = 5.5$ µm. The propagation distance that separates the near-field from the far-field is on the order of $\pi w_0^2/\lambda$ where λ is the acoustic wavelength. The propagation distance in our experiments (≈ 150 µm) is comparable to $\pi w_0^2/\lambda \approx 140$ µm and we must consider diffraction in our data analysis.

We start by considering diffraction of a 2D wave for an isotropic medium for a wave of wave-vector $k = 2\pi/\lambda$. The wave amplitude at an arbitrary position (x_0, y_0) is the superposition of the circular waves generated by each point of the source. For a line source centered at $x = 0, y = 0$ and extending in y direction with Gaussian intensity distribution $u_0 \equiv \exp(-2y^2/L^2)$ (L is the $1/e^2$ spot radius), the wave amplitude at (x_0, y_0) is

$$U(x_0, y_0) \propto \int_{-\infty}^{\infty} \exp\left(-2\frac{y^2}{L^2}\right) \frac{\exp\left(-ik\sqrt{x_0^2 + (y_0 - y)^2}\right)}{(x_0^2 + (y_0 - y)^2)^{1/4}} dy \qquad (6.11)$$

The exponential term in the numerator is the phase of circular waves. The amplitude of a circular wave in 2D falls off with distance r as $1/\sqrt{r}$

The Si (100) surface is not isotropic and the SAW velocity v_{SAW} varies with direction. We plot the slowness surface $1/v_{\mathrm{SAW}}$ in Fig. 6.6. From $\langle 100 \rangle$ to $\approx 37^\circ$ away from $\langle 100 \rangle$, SAW is Rayleigh-like and has relatively big perpendicular displacement (so measurable in experiment) and its slowness surface is plotted. Beyond $\approx 37^\circ$ till $\langle 110 \rangle$, PSAW has much bigger perpendicular displacement and its slowness surface is plotted. The discontinuity in Fig. 6.6 appears because the slowness surface of the two modes don't intersect. The vector normal to the slowness surface is the direction of the group velocity. For directions near $\langle 110 \rangle$, the slowness surface has smaller curvature than a circle and the vectors normal to the slowness surface tilt toward $\langle 110 \rangle$. This phonon focusing effect concentrates energy toward $\langle 110 \rangle$ and suppresses the effects of diffraction in this direction.

Taking into account phonon-focusing effects, the wave intensity at (x_0, y_0) is [91, 92]:

$$U(x_0, y_0) \propto \int_{-\infty}^{\infty} \sum_{l=1}^{N} \frac{u_0(y)}{\sqrt{|\bar{r}|} v_g^{(l)} \kappa^{(l)}} \times \exp\left(-i\bar{k}^{(l)} \cdot \bar{r}\right) dy, \qquad (6.12a)$$

$$\bar{r} = (x_0, y_0 - y), \qquad (6.12b)$$

$$u_0(y) = \exp\left(-2y^2/L^2\right), \qquad (6.12c)$$

$$\bar{n} = \frac{\bar{r}}{|r|}. \qquad (6.12d)$$

To evaluate Eq. 6.12, we first find $\bar{n}$, the direction vector from point source $(0, y)$ to field point (x_0, y_0). Then we search the slowness surface to find points

$s^{(1)}$ to $s^{(N)}$ whose group velocities have the same direction as $\bar{n}$. These N points have group velocity $\bar{v}_g^{(l)}$, phase velocity $\bar{v}_p^{(l)}$, curvature $\kappa^{(l)}$, and wave vectors $\bar{k}^{(l)} = \omega \bar{v}_p^{(l)}$, $l = 1 \ldots N$. Note that if the slowness surface is a circle, then $\bar{v}_g = \bar{v}_p = \bar{v}$ and only one point would satisfy the requirement.

I experimentally verify this calculation by measuring the wave amplitude as a function of probe position displaced perpendicular to the wave propagation direction, i.e., the transverse direction, at ≈ 150 µm from the source, see Fig. 6.2. The calculation for the isotropic case, Eq. 6.11 (blue line), gives a wider distribution along the transverse direction than experiment. The calculation for the phonon-focusing case, Eq. 6.12 (red line), is narrower and fits the measurement well.

6.3.3 Effect of metal grating

The effect of a thin metal grating on SAWs has been described previously [93, 32]. We numerically model the perturbation of SAWs created by the metal grating using the mass loading approximation [32] and the surface Green's function method. (Details of our calculations are given in Appendix 3.2). The grating creates changes in dispersion, i.e., band structure, and attenuation, i.e., reduced lifetimes.

Without the grating, the dispersion is a straight line with equal group and phase velocity. When a periodic array of metal bars are added to the surface, these bars are displaced together with the surface by the SAW. The surface must provide sufficient force to drive the displacement of the bars and therefore the boundary condition at the surface is a periodic force field. Similar to an electron wave function in a periodic potential, the dispersion curves of SAWs are folded into the first Brillouin zone: $-\pi/\lambda$ to π/λ, where λ is the periodicity of the grating.

Because of the folding in k-space, the SAW dispersion curve intersects the dispersion curve of fast bulk transverse acoustic waves and bulk longitudinal acoustic waves. The figure in Appendix 3.4.2 shows the dispersion in first Brillouin zone and coupling between SAW and bulk acoustic wave. Al has relatively low density and produces less attenuation than a high density metal such as Au [93].

Zone folding can create a band gap at the Brillouin zone center if the

filling factor of the grating deviates from 0.5. Fig. 6.4 plots $\mathrm{Im}(G_{33}(k_{\|}, \omega, x_3 = 0))$ near the Brillouin zone center with delta excitation. Fig. 6.4a shows if the filling factor is 0.5, there is no band gap at Brillouin zone center. However, if the filling factor is not 0.5, for example 0.35 as shown in Fig. 6.4c, there is a significant band gap at Brillouin zone center from $\approx -0.04 \times 10^6$ m^{-1} to $\approx 0.04 \times 10^6$ m^{-1}.

For a filling factor that deviates from 0.5, the $k = 0$ modes of the two branches are standing waves with a $\pi/2$ phase difference. Because of this phase difference, the two standing waves drive the metal bars with different magnitudes displacements and accelerations and the energies of the two waves are different, opening a gap. If the grating has a 0.5 filling factor, standing waves with $\pi/2$ phase difference have the same magnitude of displacement and hence the same energy, and the energy gap at $k = 0$ is zero.

Deviations from 0.5 filling factor and the opening of a gap at zone center is important in our measurements. A SAW excited by a finite size pump beam is composed of wave components over a range of wave vectors k of $-2\pi/L < k < 2\pi/L$ near the Brillouin zone center, where $L \approx 5.5$ µm is the $1/e^2$ radius of the focused pump. So the range of excited wave vector is from $\approx -0.18 \times 10^6$ m^{-1} to $\approx 0.18 \times 10^6$ m^{-1}. These components combine to form a Gaussian wave packet. If a band gap exists at zone center, then the wave components close to zone center have suppressed group velocity. After propagating a long distance, these slower components of the wavepacket will lag behind the other components of the wavepacket with k farther away from the zone center. For grating with 0.35 filling factor, $\approx 20\%$ of the wave component has group velocity ranging from the SAW velocity v_{SAW} to zero (right at the center of band gap) as Fig. 6.4c shows. Thus, the shape of the wave packet will not be Gaussian, as Fig. 6.4d shows, and difficult to interpret. If the band gap is small, then the wave packet has a Gaussian shape, as Fig. 6.4b shows, and is simpler to analyze.

6.4 Experimental results and discussion

We define the wave amplitude measured with closely separated (l_{close}) pump and probe as R_{close} and the wave amplitude with widely separated (l_{far}) pump and probe as R_{far}; the total attenuation of SAW after it travels $l =$

$l_{close} - l_{far}$ is $A = R_{far}/R_{close}$. As discussed in Sec. 6.3, A contains effects from diffraction, damping created by the metal grating, and the intrinsic attenuation of Si:

$$A \equiv \frac{R_{far}}{R_{close}} = f(l)D(l)\exp\left(-\alpha_g l_g\right)\exp\left(-\alpha_{Si} l\right) \tag{6.13}$$

α_{Si} is the intrinsic attenuation coefficient; α_g is the attenuation coefficient of the Al grating; and l_g is the width of Al grating region. $D(l)$ is the contribution of diffraction and phonon focusing. $f(l)$ is sum of all other effects that we are not considering, for example the effect of surface roughness and the presence of the native oxide of Si.

As described in Sec. 6.2, for R_{far} we want to measure SAW generated by pump pulse $n = -2$ and place the signal in the out-of-phase channel. We therefore separate the pump and probe by $l_{far} = 147$ µm which is how far the SAW travels in ≈ 30 ns. In this way, we position the probe so that the wave packet is at the center of the measurement window. To measure R_{close}, we want to suppress the thermal signal. We choose $l_{close} = 10$ µm so that the thermal signal is small and the SAW wave-packet is in the center of the measurement window.

We first consider the amplitude change $D(l)$ caused by diffraction combined with phonon focusing. Calculation using Eq. 6.12 gives $D(l) = 0.85$.

We then consider damping created by the grating. Experimentally, we find $\alpha_g > \alpha_{Si}$. To increase the sensitivity of the experiment to α_{Si}, we must minimize l_g. Even the grating within the small distance of propagation across the width of the pump and probe optical beams creates appreciable damping and therefore we must quantify the damping created by the Al grating to improve the measurement of α_{Si}. Based on Eq. 6.13, $\ln(R_{far}/R_{close})$ changes linearly with l_g. Thus, we can fit a line to $\ln(R_{far}/R_{close})$ versus l_g and extrapolate to $l_g = 0$ to remove damping created by Al grating.

This is achieved by varying the gap width. Fig. 6.1 shows part of the sample which has three different gap widths. In experiment we change the gap size from 130 µm to 90 µm but keep l_{far} constant, i.e., the width of the grating region varies from 17 µm to 57 µm. To align the relative position of pump and probe along the transverse direction, we displace the pump beam along the transverse direction and find the position where the signal is maximized.

The inset of Fig. 6.5 shows the experimental configuration to measure R_{far}. Fig. 6.5 shows the measured attenuation with five different widths of grating region, fitting, and extrapolation to the point where attenuation from Al grating is removed. We repeat the measurement at four temperatures: 30, 100, 200 and 250°C. If $f(l)$ is assumed as 1, we can obtain: at 30°C, $\alpha_g = 152$ cm^{-1}, $\alpha_{Si} = 9$ cm^{-1}; at 100°C, $\alpha_g = 145$ cm^{-1}, $\alpha_{Si} = 14.2$ cm^{-1}; at 200°C, $\alpha_g = 140$ cm^{-1}, $\alpha_{Si} = 18.4$ cm^{-1}; at 250°C, $\alpha_g = 136$ cm^{-1} and $\alpha_{Si} = 19.4$ cm^{-1}.

In Boltzmann theory, the change in the occupation number of a mode is generated by two processes: phonon transport between regions with different strain, and localized phonon relaxation due to phonon collisions [60]. Eq. 6.1 can be viewed as a result from localized relaxation theory [68], with $Q \propto \omega\tau/(1+\omega^2\tau^2)$. Therefore, Eq. 6.1 is a good approximation when phonons relax locally before they propogate to regions with different strain, i.e. $\langle v_{phonon}\rangle\tau \ll v/f$, where $\langle v_{phonon}\rangle$ is the averaged group velocity of thermally excited phonons, $f = \omega/2\pi$ is the frequency of the acoustic wave, and v is the velocity of acoustic wave. This condition can be written as $\omega\tau < v/\langle v_{phonon}\rangle$. At temperature much lower than the Debye temperature, only a small fraction of the acoustic phonon branches are excited and $v/\langle v_{phonon}\rangle \geqslant 1$. Mason *et al.* [67, 68] show that Eq. 6.1 fits the measured acoustic attenuation of Si well at low temperature when $\omega\tau \geqslant 1$. For Si at RT, the majority of phonon modes are excited. The phonon modes with larger wave vector generally have smaller group velocity and higher density of states. In particular, the group velocity of optical phonons is much smaller than v. Thus, we conclude that $v/\langle v_{phonon}\rangle > 1$ in Si at RT. Our experiment falls into the $\omega\tau \sim 1$ and RT regime, $\omega\tau < v/\langle v_{phonon}\rangle$ is satisfied, and Eq. 6.1 is a good approximation.

I fit results for α_{Si} to Eq. 6.1, see Fig. 6.7. In Eq. 6.1, we use the heat capacity for Si from Ref. [94]. We assume that the relaxation time scales as $\tau \propto 1/T$. The fitting gives $\tau = 30$ ps and $\langle\gamma^2\rangle - \langle\gamma\rangle^2 = 0.053$. The experimental uncertainty in τ is large, approximately a factor of two. The uncertainty in $\langle\gamma^2\rangle - \langle\gamma\rangle^2$ is much smaller, on the order of ± 0.01.

The measured intrinsic attenuation coefficient and Akhiezer model using the fitted τ and $(\langle\gamma^2\rangle - \langle\gamma\rangle^2)$ are compared with previous experimental results and phonon viscosity modeling in Fig. 6.8, which also reveals discrepancies among prior experiments and the phonon viscosity models.

Based on our analysis of Sec. 6.3.1, the attenuation coefficient of SAW by theory of phonon viscosity can be calculated by Eq. 6.3 with the effective viscosity η_{SAW} calculated by Eq. 6.10. The results using phonon viscosity tensors of Lamb & Richter [72] and Helme & King [75] are labeled as "SAW-Lamb viscosity" and "SAW-Helme viscosity" respectively in Fig. 6.8. Extrapolation of our experimental results to $\omega^2\tau^2 \ll 1$ agrees better with the calculation based on Helme & King's phonon viscosity tensor. In the regime of our measurements, $\omega\tau \sim 1$, the Akhiezer damping predicted by Eq. 6.1 deviates significantly from the phonon viscosity model, Eq. 6.3.

The energy dissipation in mechanical oscillator can be from extrinsic and intrinsic mechanisms. Two important extrinsic mechanisms are air damping [95] and clamping loss [96, 97]. The intrinsic damping mechanism are thermoelastic dissipation [62, 98] and Akhiezer damping. For extrinsic damping, vacuum packaging can be used to eliminate air damping and symmetrical design of mechanical oscillator can reduce the clamp damping. For intrinsic damping, utilizing specific modes can suppress thermoelastic dissipation. For example, a pure shear strain in cubic crystal does not cause volume change and therefore no thermoelastic dissipation occurs. Akhiezer damping is created by a local strain and represents a fundamental upper limit to the Q of mechanical oscillators. Our measurements show that the mean-squared variation of Grüneissen parameters $\langle\gamma^2\rangle - \langle\gamma\rangle^2$ of shear strain is an order of magnitude smaller than the corresponding paramaters for normal strain [67, 99, 73]. Comparing with the Akhiezer damping of longitudinal acoustic wave measured by Daily *et al.* [25], the Akhiezer damping of acoustic wave at GHz with predominately shear character is ~ 6 times smaller. A silicon mechanical oscillator with vibrational mode of mostly shear character will have higher upper-limit of the Q factor than one with vibrational mode of predominately normal character.

6.5 SAW by metal grating used as sensor

The experimental design described in this chapter can also be used as sensor [33]. The exact same sample geometry such as Fig. 6.1 is put inside a vacuum chamber. Then the pressure of refrigerant vapor is gradually increased. In this process, the v_{SAW} is measured by separating pump and probe

beams far away from each other. As the refrigerant gradually condensed on top of the Si substrate, it poses as a mass layer and changes v_{SAW}. However this change is very small. That's the reason why I need to measure SAW after it propagates for 150 µm. The small shift of SAW signal in time domain is shown in Fig 6.9. This shift is indeed caused by the tiny change of v_{SAW}. The change of v_{SAW} can be interpreted as the mass loading using the calculation discussed in Chapter 3. The mass loading can then be converted to the mass of the condensation layer using the calculation introduced in Chapter 3. In the measurement I observed certain instability slightly below the saturation pressure. But I didn't further the investigation to understand it.

6.6 Figures

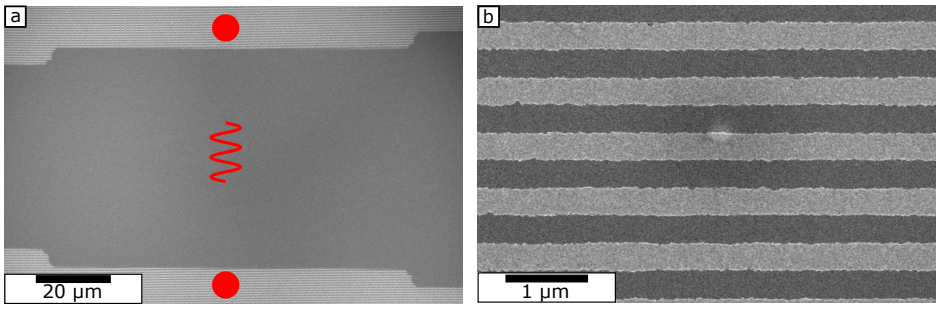

Figure 6.1: SEM image of the grating structure. In (a), the dark area is exposed Si. The bright area is the Al grating. Al metal bars are fabricated parallel to the edge of the gap region. Two red points illustrate schematically how the pump and probe beams are separated. In our experiments, the pump and probe beam are separated by 150 µm. The red wavy line indicates the wave propagation from the pump grating to probe grating. (b) Higher magnification image of the Al grating with 700 nm period, $\approx$ 15 nm thickness and $\approx$ 50% filling factor.

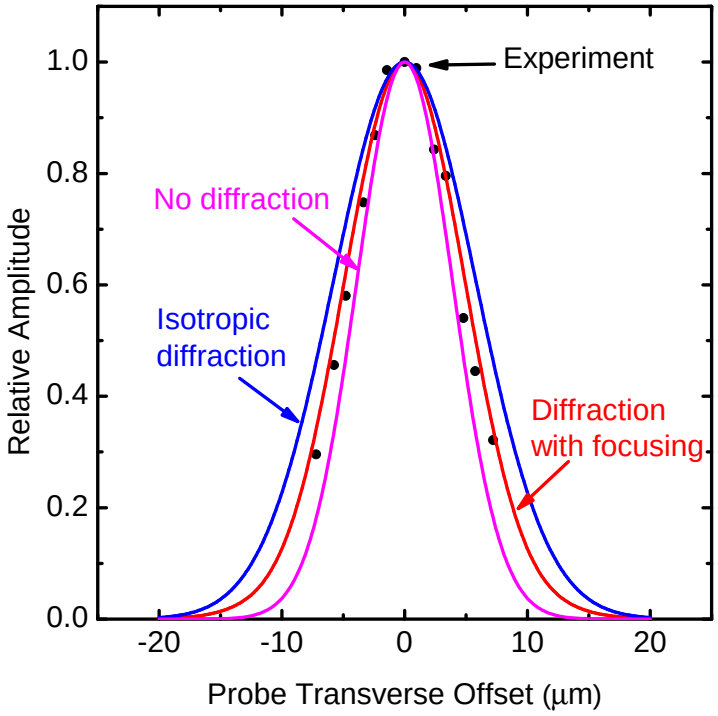

Figure 6.2: Relative signal intensity when the probe beam is offset at transverse direction at far field. Black dots are experiment result. Red line is calculation considering phonon focusing (Eq. 6.12). Blue line is calculated diffraction for an isotropic plane (Eq. 6.11). The line labeled "No diffraction" is the calculation if no diffraction is considered.

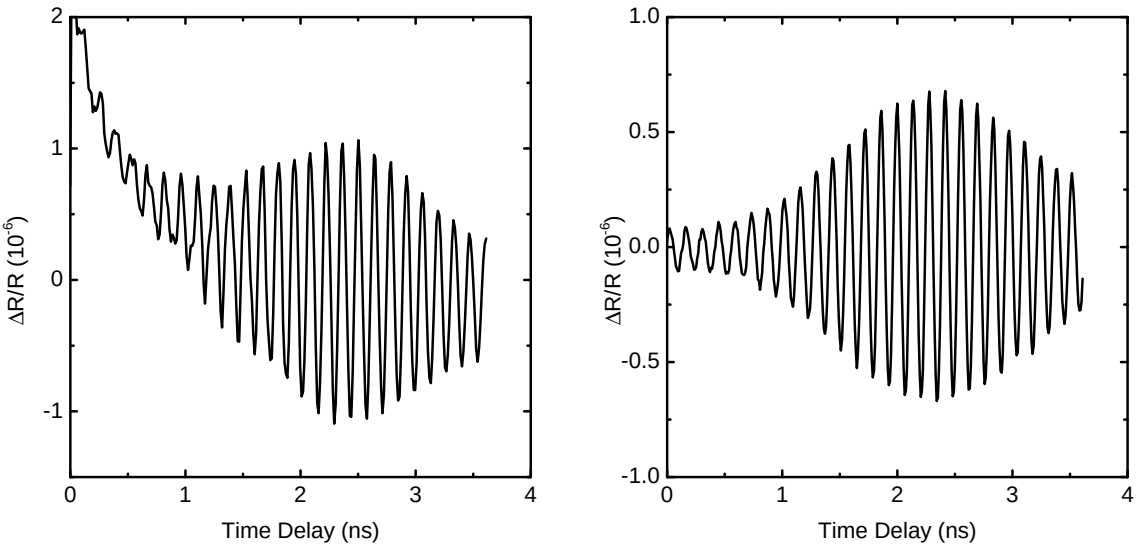

(a) (b)

Figure 6.3: (a) Typical in-phase signal for a close offset measurement. Pump and probe beam are offset by 10 µm. (b) Typical out-of-phase signal for a far offset measurement. Pump and probe beam are offset by 150 µm.

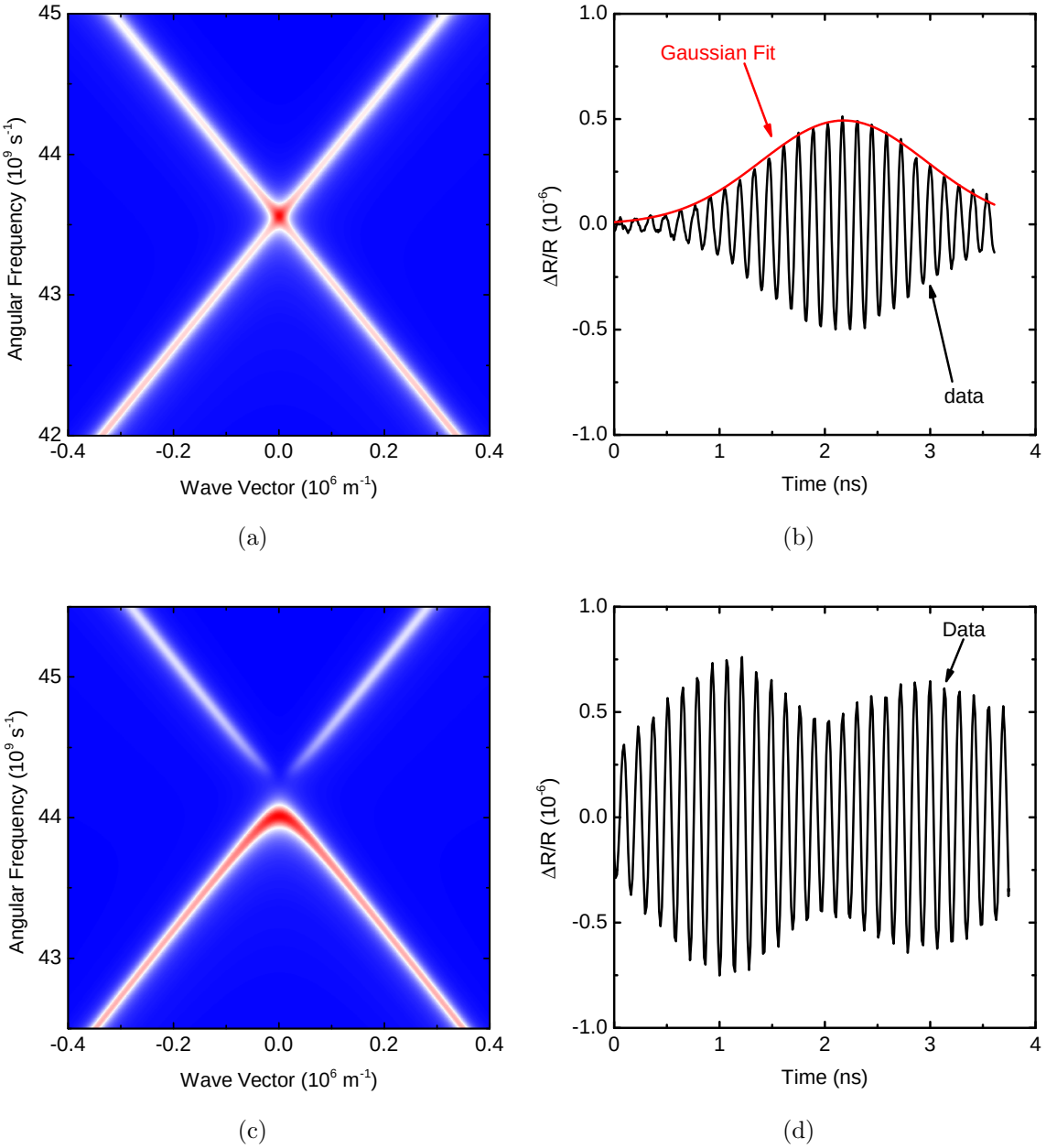

Figure 6.4: (a): $\mathrm{Im}(G_{33})$ at Brillouin zone center with 0.5 grating filling factor and delta excitation. (b) Far field signal with grating of ≈ 0.5 filling factor. (c): $\mathrm{Im}(G_{13})$ at Brillouin zone center with 0.35 grating filling factor and delta excitation. (d) Far field signal with grating of ≈ 0.35 filling factor.

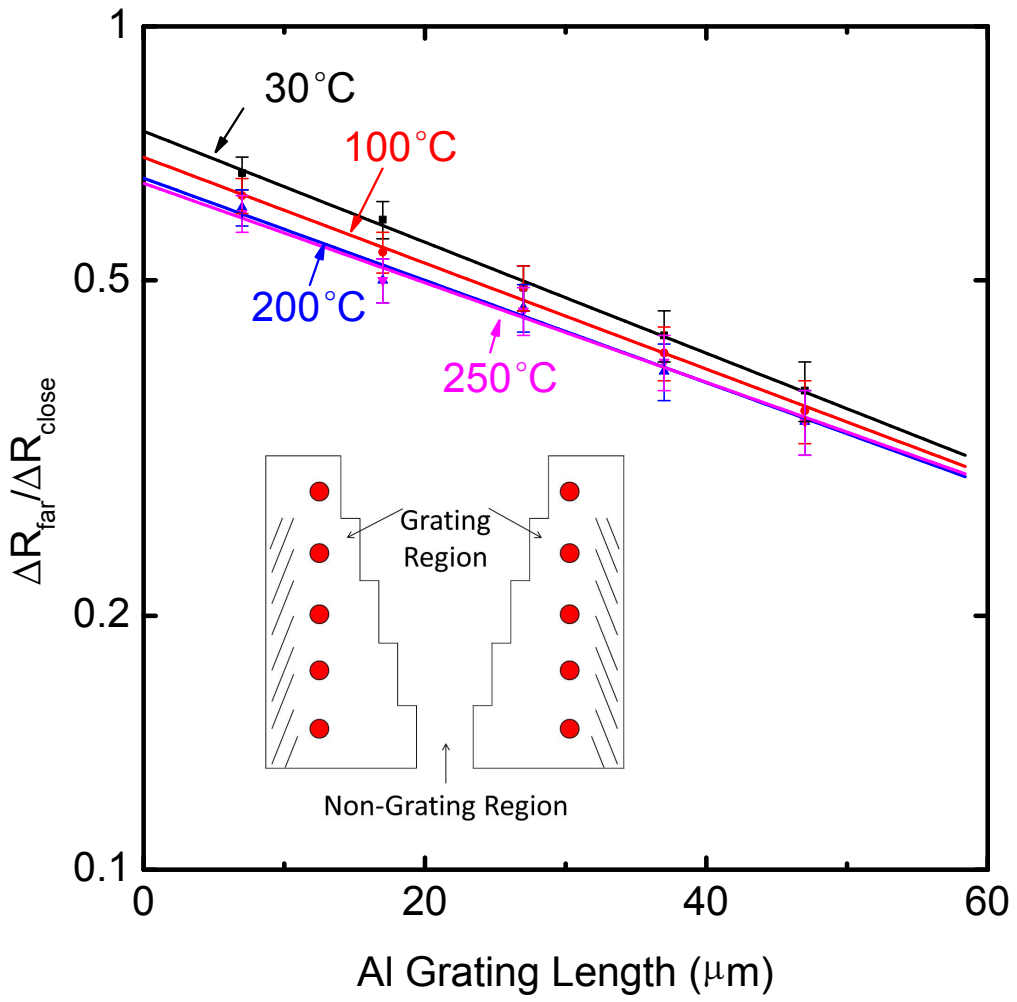

Figure 6.5: Ratio between wave amplitudes of far offset and close offset with different length of grating region. The vertical axis is plotted at log scale and data is fitted with straight lines. Each set of date is labeled by the sample temperature. The slope can be used to calculate the attenuation coefficient of the Al grating. The inset is the measurement configuration for far offset. Red dots stand for pairs of positions of pump and probe beams. Repeat the measurement for five different gap widths while keeping the distance between pump and probe beam constant introduces five different length of grating region. Comparing them with the close offset measurement gives five data points at each temperature.The results are extrapolated to zero grating length (on the vertical axis) to get intrinsic attenuation.

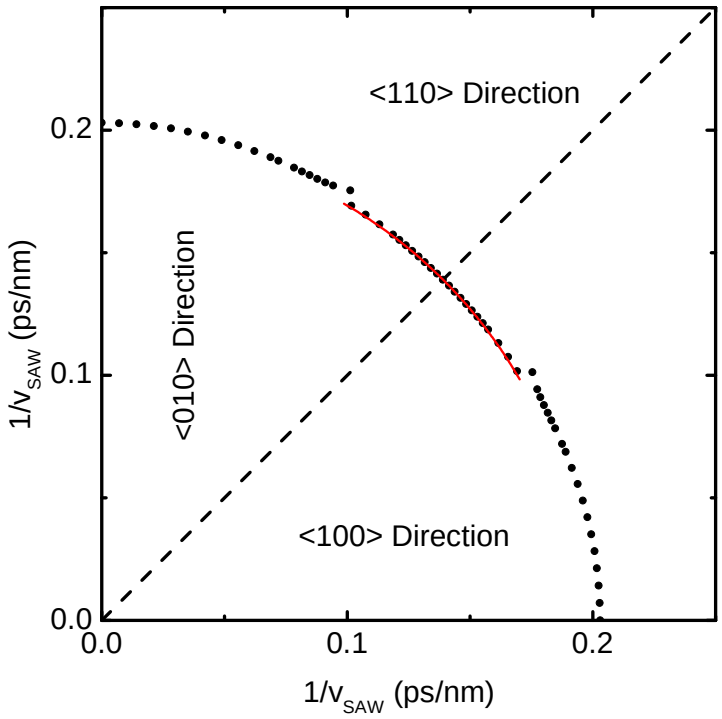

Figure 6.6: Slowness surface of Rayleigh-like SAW (from $\langle 100 \rangle$ direction to $\approx 37^{\circ}$ away, where the discontinuity is at) and the PSAW (from the discontinuity to $\langle 110 \rangle$ direction) on the Si(100) plane and comparison between slowness surface close to $\langle 110 \rangle$ direction and a circle (red line).

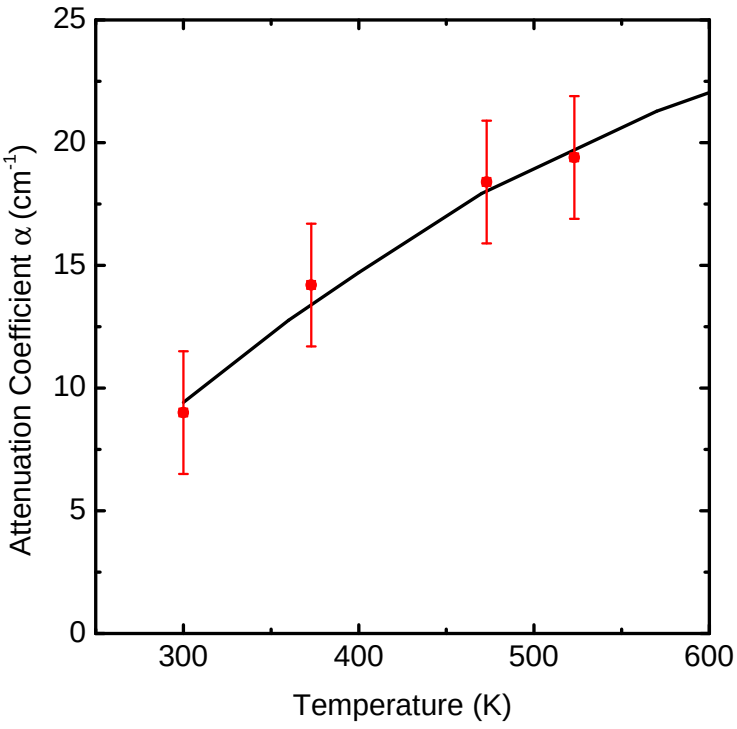

Figure 6.7: Temperature dependence of measured intrinsic attenuation coefficient. Red points are measurements. Black line is a fit to the data using Eq. 6.1 and $\tau = 30$ ps and $(\langle\gamma^2\rangle - \langle\gamma\rangle^2) = 0.053$.

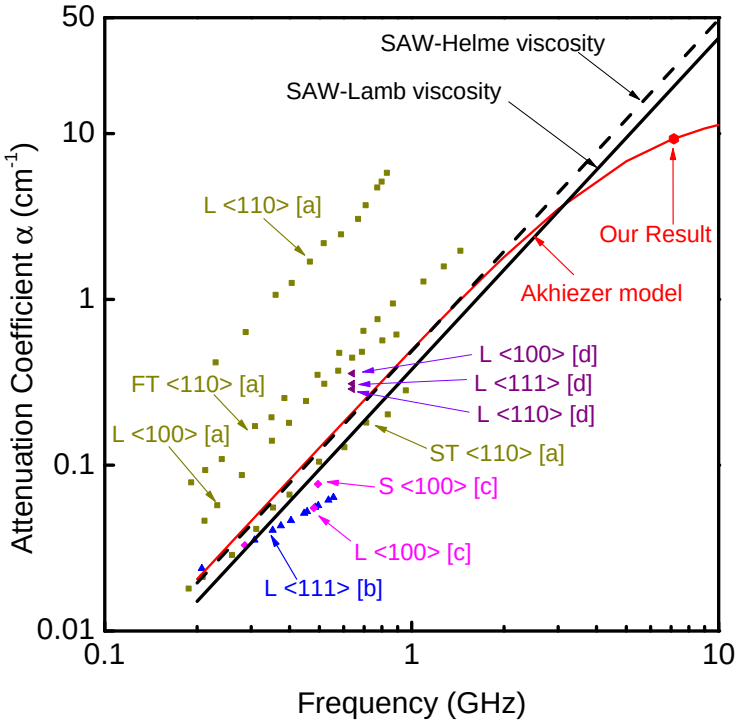

Figure 6.8: Comparison between our result and prior reports and phonon viscosity model. L denotes longitudinal bulk acoustic wave. FT and ST denotes bulk fast transverse acoustic wave and bulk slow transverse acoustic wave. Notation like $\langle 100 \rangle$ denotes the propagation direction. Data [a] is from Ref. [77]. Data [b] is from Ref. [74]. Data [c] is from Ref. [67]. Data [d] is from Ref. [78]. Straight line of "SAW-Lamb viscosity" and dash line "SAW-Helme viscosity" correspond to the attenuation coefficient of SAW calculated using Eq. 6.3 and effective viscosity of SAW from Eq. 6.10. They use phonon viscosity tensor from Lamb & Richter [72] and Helme & King [75] respectively. Akhiezer model is calculated using Eq. 6.1, where τ and $\langle \gamma^2 \rangle - \langle \gamma \rangle^2$ are from our measurement.

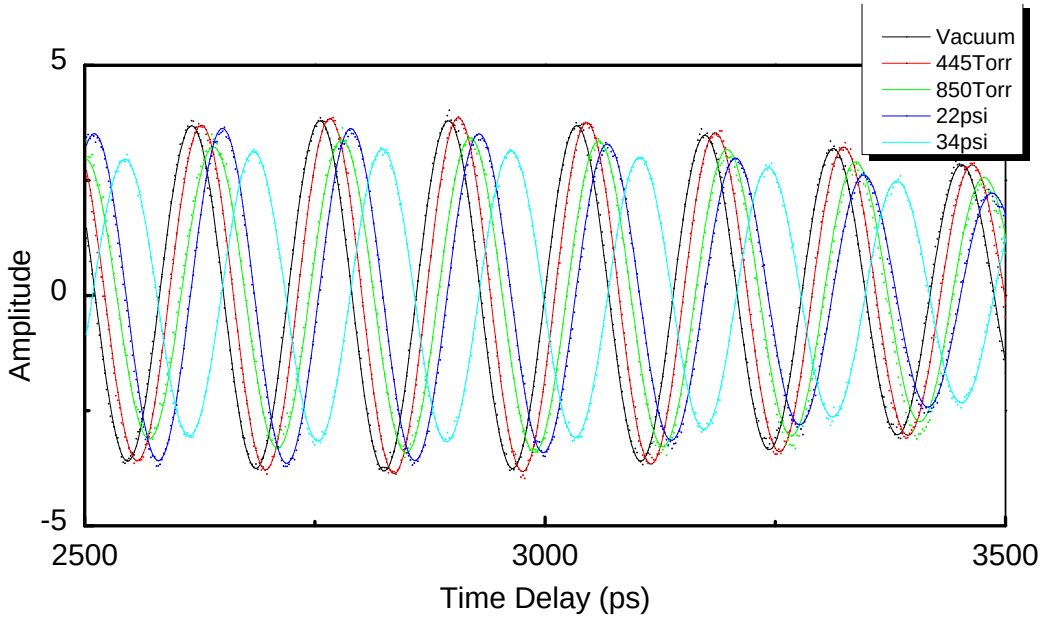

Figure 6.9: SAW signal after propagating ≈ 150 µm under different vapor pressure of refrigerant using the "gapped-grating" structure. The shift of the oscillation is because of the small change in v_{SAW} due to the condensation of refrigerant on the sample surface. The shift can be used to calculate the change in v_{SAW}

CHAPTER 7

CALCULATION OF ELASTIC CONSTANTS AND GENERALIZED GRÜNEISEN PARAMETER BY DENSITY FUNCTIONAL THEORY

7.1 Revisit some concepts of solid mechanics

In Chapter 2, I briefly define stress, strain, and introduce the equation of motion, to serve as the foundation of SAW calculation. In this chapter, the calculation of second order elastic constant and generalized mode Grüneisen parameters will be discussed. Experimentally, one can measure the mode Grüneisen parameter of phonon at Gamma point. The relevant experiments are the third order elastic constant (TOEC) measurement and the Raman spectroscopy with material under strain. In both cases, the specimen is subjected to a certain strain and the lattice deviates from its original, or fully relaxed lattice. However the material properties are usually defined for material with no deformation. So the experiments and description of material are at different coordinate system. In the beginning of this chapter, I introduce a more general and complete view of solid mechanics which is useful in understanding the calculation of second order elastic constant and comparison between TOEC and generalized mode Grüneisen parameter.

7.1.1 Lagrangian description and deformation gradient

This section is a selected combination of various online resources and Thurston's review article: *Wave propagation in fluids and normal solids*, which is the first article of the first edition of the series: *Physical Acoustics*, *Principles and Methods*. The following description is selected and rearranged by myself and serves for the purpose of better understanding of the topic discussed later.

If one lattice is strained and moved from it's original position, it can be

located by the spatial coordinates x_i:

$$\bar{r} = (x_1, x_2, x_3)$$

is the *spatial coordinates* of the material. From another point of view, every particle can be identified by the coordinates a_i when there is no strain:

$$\bar{a} = (a_1, a_2, a_3)$$

which is the *material coordinates*. $\bar{a}$ serves as a name for the particle. Coordinates $\bar{r}$ is associated with $\bar{a}$ by the rule that $\bar{r}$ is the present position vector of the particle initially at $\bar{a}$, i.e.,:

$$\bar{r} = \bar{r}(t, \bar{a})$$

This is usually called the *material description* or *Lagrangian description*.

The relationship between $\bar{r}$ and $\bar{a}$ can be written using derivative:

$$F_{ij} = \frac{\partial x_i}{\partial a_j}, \tag{7.1}$$

which is a 3×3 matrix. F_{ij} is usually called deformation gradient. This set of derivatives can also be interpreted as vector operators defining the rotation and stretch of material line element. The determinant of the deformation gradient matrix is defined:

$$J \equiv \det(F_{ij}), \tag{7.2}$$

and one can prove the properties:

$$J = \lim_{\mathrm{d}V_0 \to 0} \frac{\mathrm{d}V}{\mathrm{d}V_0}, \tag{7.3}$$

i.e. J is the relative volume element change or inverse of relative density change:

$$J = \frac{\rho_0}{\rho}, \tag{7.4}$$

where V_0 and ρ_0 are the original volume and density and V and ρ are the new volume and density after the strain.

The deformation gradient F_{ij} is the starting point of solid mechanics. The term *strain* always refers to a change in the relative position of the ma-

terial points in a body. Changes in the distance between particles distinguish strains from rigid body motions. So in the material description, the strain component η_{jk} is defined as:

$$\mathrm{d}x_i\,\mathrm{d}x_i - \mathrm{d}a_i\,\mathrm{d}a_i = 2\eta_{ij}\,\mathrm{d}a_j\,\mathrm{d}a_k, \tag{7.5}$$

Since $\mathrm{d}x_i = F_{ij}\,\mathrm{d}a_j$, in the material description we have:

$$(\frac{\partial x_i}{\partial a_j}\,\mathrm{d}a_j)(\frac{\partial x_i}{\partial a_k}\,\mathrm{d}a_k) - \mathrm{d}a_i\,\mathrm{d}a_i = 2\eta_{ij}\,\mathrm{d}a_j\,\mathrm{d}a_k, \tag{7.6}$$

which leads to:

$$\eta_{jk} = \frac{1}{2}(F_{ij}F_{ik} - \delta_{jk}), \tag{7.7}$$

So the strain η_{ij} is also called *Lagrange strain*.

We can derive the strain definition in Chapter 2 by introducing the *displacement* vector as: $\bar{u} = \bar{x} - \bar{a}$. Putting it back one can have

$$\eta_{jk} = \frac{1}{2}(\frac{\partial u_j}{\partial a_k} + \frac{\partial u_k}{\partial a_j} + \frac{\partial u_i}{\partial a_j}\frac{\partial u_i}{\partial a_k}) \tag{7.8}$$

When the displacement is small and the second order is omitted, η_{ij} is the same as the definition in Chapter 2.

A few more properties about deformation gradient that will be useful in the derivation of the TOEC and Grüneisen parameter: the derivative of J is:

$$\partial J/\partial F_{ij} = JF^{-1}_{ji} \tag{7.9}$$

The stretch rate is defined as

$$d_{ij} \equiv \frac{1}{2}(\frac{\partial v_i}{\partial x_j} + \frac{\partial v_j}{\partial x_i}) \tag{7.10}$$

d_{ij} quantifies the relative velocity of particles in the deformed solids.

The derivative of Lagrangian strain with respect to deformation tensor can be calculated based on Eq. 7.7:

$$\frac{\partial \eta_{mi}}{\partial(\partial x_k/\partial a_m)} = \frac{\partial \eta_{mi}}{\partial F_{km}} = \frac{1}{2}(F_{ki}\delta_{mm} + F_{km}\delta_{mi}) = \frac{1}{2}(F_{ki}) = \frac{1}{2}F_{ki}(1+\delta_{mi}) \tag{7.11}$$

7.1.2 Different stress measures

In Chapter 2, the Cauchy stress tensor σ_{ij} is defined. It is the best physical measure of the internal force. However when working in the deformed coordinates, the Cauchy stress tensor may not be the most convenient one to use since it is the real stress in the spatial coordinates system. So for the convenience of analysis, the *second Piola-Kirchhoff stress* is introduced as:

$$t_{ij} = JF_{ik}^{-1}\sigma_{kl}F_{jl} \tag{7.12}$$

It is also called the material stress or the thermodynamic tension. The material stress is a fictitious stress tensor. The purpose of this definition is to create a stress measure that is the work-conjugate of Lagrange strain tensor, i.e. the rate of work $\dot{W}$ done by stresses acting on a small material element with volume $\mathrm{d}V_0$ in the undeformed material is:

$$\dot{W} = \dot{\eta_{ij}} t_{ij}\,\mathrm{d}V_0.$$

Then the definition of the second and third order elastic constant should be based on the material stress:

$$c_{ijkl} = \frac{\partial t_{ij}}{\partial \eta_{kl}} = \rho_0 \frac{\partial^2 U}{\partial \eta_{ij}\partial \eta_{kl}} \tag{7.13}$$

$$c_{ijklmn} = \frac{\partial c_{ijkl}}{\partial \eta_{mn}} = \rho_0 \frac{\partial^2 U}{\partial \eta_{ij}\partial \eta_{kl}\partial \eta_{mn}} \tag{7.14}$$

In the above discussion, I intentionally omit the discussion of thermodynamics to make the argument as simple as possible. A rigorous derivation require distinguishing the "isothermal process" and "isentropic process" which corresponds to two sets of formulation. In isentropic process, elastic constants are defined by expanding the internal energy per unit mass U at constant entropy:

$$\rho_0 U(\eta_{ij}, S) = \rho_0 U(0, S) + \frac{1}{2}c^S_{ijkl}\eta_{ij}\eta_{kl} + \frac{1}{6}c^S_{ijklmn}\eta_{ij}\eta_{kl}\eta_{mn} + \dots\,, \tag{7.15}$$

while in isothermal process, the isothermal elastic constants are defined by

expanding Helmholtz free energy per unit mass at constant temperature:

$$\rho_0 F(\eta_{ij}, T) = \rho_0 F(0, T) + \frac{1}{2} c^T_{ijkl} \eta_{ij} \eta_{kl} + \frac{1}{6} c^T_{ijklmn} \eta_{ij} \eta_{kl} \eta_{mn} + \dots , \qquad (7.16)$$

DFT calculation is done at constant effective temperature of 0 K. So $F(T = 0) = U(T = 0)$. The experimental values are mostly measured under isentropic condition while the calculation is at the isothermal condition. In practice I found for material I have studied, there is little difference between the two cases, which will be briefly discussed later regarding the volume change in elastic constant calculation.

7.2 Calculation of second order elastic constant by density functional theory

In measurement of shear elastic constants described in Chapter 5, materials with relatively low symmetry have five or more independent elastic constants so we cannot directly measure all of them by acoustic methods. However it's necessary to have the full set of stiffness matrix to do SAW calculation and fitting. One way to achieve this is to calculate elastic constant using density functional theory (DFT).

The main purpose of this study is to calculate elastic constant of misfit layered compound discussed in Chapter 5. To verify the capability of the calculation, two layered materials, graphite and MoS_2 are calculated. In the following they are used as examples of materials with hexagonal structure and Van der Waals bonding between atomic layers.

Our group has limited experience of DFT calculation. I learned the calculation under the guidance of Professor André Schleife. I would like to detail the procedure using the commercial software VASP in this chapter, although some of which are basics and standard in DFT calculation. I hope this could serve as convenient references for people later that may do similar calculation.

7.2.1 Standard procedures in density functional theory calculation

DFT is such a wide and deep field that I do not intend to cover any theoretically background in this section. There are many books and review papers for that purpose. Professor Kieron Burke's tutorial: *The ABC of DFT* may be a good start. The free electronic version can be found on his group website. In this section I focus instead on the procedure part of the calculation, under the context of the DFT software `VASP`.

A standard DFT calculation starts from an initial atomic structure. The calculation searches for electronic ground states (through electronic steps) and then moves the positions of ions (ionic steps), if allowed, to search for ground state of the system.

Before any calculations, a convergence test is done for the materials under study. The purpose of convergence test is to determine the upper limit for essential calculation parameters: the energy cutoff (`ENCUT`) and mesh of k space (`KPOINTS`). Energy cutoff determines how many plane-wave basis are included in the calculation; k-mesh determines the fineness of mesh in the Brillouin zone. In convergence test, no relaxation is needed. The purpose is to determine whether changes in energy cutoff or mesh fineness would lead to significant changes in calculation results. `ENCUT` and `KPOINTS` are two of the most important factors that control the accuracy and intensity of the calculation. Choose high enough `ENCUT` and mesh in `KPOINTS` until they have minimal effect to the calculated total energy. The calculation time may also be a factor to consider to choose the proper `ENCUT` and mesh.

A basic application of the DFT calculation is to find the optimal atomic structure of material. It also serves as an evaluation of accuracy of the calculation by comparing the optimal structure with the experimental results. To find the optimal structure, the "total energy vs. volume" curve is plotted. For each volume, the structure is fully relaxed (reaches minimum energy) by changing the cell shape and ion position. If the relaxation ends with more than one ionic step, the calculation is repeated with the previous obtained ionic position (in `CONTCAR`) as the new initial position of the calculation (`POSCAR`), until the the calculation ends with only one ionic step. Then the energy vs. volume curve is fitted by the equation of state (EOS). The EOS

I use is:

$$E(V) = E_0 + \frac{9}{16} V_0 B_0 \{ [(\frac{V_0}{V})^{2/3} - 1]^3 B_0' + [(\frac{V_0}{V})^{2/3} - 1]^2 [6 - 4(\frac{V_0}{V})^{2/3}] \}, \quad (7.17)$$

from which the bulk modulus B_0 and optimal volume V_0 can be fitted. The other two fitting parameters: initial energy E_0 and derivative of bulk modulus B_0' is usually not important. B_0' usually has the value around 9, for the reasons I don't understand. Once the optimal volume is obtained, the structure is relaxed again at optimal volume to find the optimal cell shape and positions of the atoms. Further calculation is performed on the basis of the optimal structure.

7.2.2 Calculation of second order elastic constant

I use the method of homogeneous deformation to calculate elastic constants in DFT. The method is based on the Eq. 7.13. A specifically designed Lagrangian strain tensor η_{ij} is introduced to the optimal lattice structure, to calculate a specific combination of elastic constant. By changing the size of strain, I can calculate an "energy vs. strain" curve which corresponds to the energy expansion in Eq. 7.16. If the third order term is omitted, the curve is a parabola. The combination of the elastic constants can be obtained as the coefficient of the second order term in fitting of the parabola.

Consider a primitive cell with three lattice vectors: $a_i = (a_1, a_2, a_3)$, $b_i = (b_1, b_2, b_3)$, and $c_i = (c_1, c_2, c_3)$. The volume of the primitive cell is calculated from the determinant of the matrix:

$$\begin{pmatrix} a_1 & a_2 & a_3 \\ b_1 & b_2 & b_3 \\ c_1 & c_2 & c_3 \end{pmatrix}$$

If a small strain η_{ij} is applied, the new lattice vectors become $a_i' = (\delta_{ij} + \eta_{ij}) a_j$, $b_i' = (\delta_{ij} + \eta_{ij}) b_j$, and $c_i' = (\delta_{ij} + \eta_{ij}) c_j$. The new volume can be calculated with the same fashion. Using a simple strain as example:

$$\eta_{ij} = \begin{pmatrix} \delta & 0 & 0 \\ 0 & -\delta & 0 \\ 0 & 0 & \delta^2/(1-\delta^2) \end{pmatrix}$$

After the strain is applied, the total energy of the cell of a cubic crystal can be expressed as:

$$E(V, \delta) = E(V_0) + V(c_{11} - c_{12})\delta^2 + O(\delta^4) \tag{7.18}$$

By omitting the fourth order term, the E vs. δ curve is a parabola and $c_{11} - c_{12}$ can be fitted.

The η_{33} term in the above example is designed solely for the purpose to conserve the total volume after the strain. One can verify it by calculating the determinant of the matrix formed by the new lattice vector. The argument for volume conserving strain can be find in Ref. [100]. The argument is, and I quote:"First, we assure the identity of our calculated elastic constants with the stress-strain coefficients, which are appropriate for the calculation of elastic wave velocities; this identity is non-trivial for finite applied pressure. Second, the total energy depends on the volume much more strongly than on strain; by choosing volume conserving strains we obviate the separation of these two contributions to the total energy. Third, the change in the basis set associated with the applied strain is minimized, thereby minimizing computational uncertainties." I don't fully understand the first reason. For the second point, I don't see how one can distinguish the effect of strain and volume change, which also means strain (hydrostatic or others). I don't understand the third point either. However in my calculation, I found there is almost no difference between the results using a volume-conserving strain or not. The strain I used is below 1%.

Crystals with different symmetry contain different number of independent elastic constants. So strain tensors varies for different symmetries. Next I describe the calculation of two symmetries: cubic symmetry and hexagonal symmetry.

7.2.3 Elastic constant of cubic crystal

Cubic crystal has only three independent elastic constant c_{11}, c_{12}, and c_{44}. The bulk modulus B has already been obtained through EOS. For cubic symmetry,

$$B = (c_{11} + 2c_{12})/3 \tag{7.19}$$

So we need two more equations to get all three elastic constants, one of which is already given before:

$$\eta_{ij} = \begin{pmatrix} \delta & 0 & 0 \\ 0 & -\delta & 0 \\ 0 & 0 & \delta^2/(1-\delta^2) \end{pmatrix}$$

to calculate $(c_{11} - c_{12})$. In order to fit c_{44}, I introduce another strain:

$$\eta_{ij} = \begin{pmatrix} 0 & \delta/2 & 0 \\ \delta/2 & 0 & 0 \\ 0 & 0 & \delta^2/(4-\delta^2) \end{pmatrix}$$

The energy expansion under this strain is:

$$E(V, \delta) = E(V_0) + \frac{1}{2} V c_{44} \delta^2 + O(\delta^4) \tag{7.20}$$

Again the purpose of the η_{33} term is to preserve volume and it doesn't really affect the results of Si from my experience.

Following the method detailed before, I calculated elastic constants of Si. I calculate elastic constant of Si to be: $c_{11} = 161.37$ GPa, $c_{12} = 64.65$ GPa, and $c_{44} = 75.84$ GPa; comparing with the experimental values: $c_{11} = 165$ GPa, $c_{12} = 63$ GPa, and $c_{44} = 79.1$ GPa, the calculation has good quality.

7.2.4 Elastic constant of hexagonal crystal

Hexagonal crystal has a Bravais lattice vector as:

$$R = a \begin{bmatrix} 1 & 0 & 0 \\ -\frac{1}{2} & \frac{\sqrt{3}}{2} & 0 \\ 0 & 0 & \frac{c}{a} \end{bmatrix}$$

where a and c are lattice constants of a hexagonal crystal. To fit the equation of state, I change the value of a and relax the cell while preserving the volume, which means I set a constant c/a ratio in the initial structure of different volumes.

In hexagonal crystal, there are five independent elastic constants. c_{11},

c_{12}, c_{13}, c_{33}, and c_{44}. And there are two kind of bulk modulus: Voigt and Reuss. The Voigt average (assuming constant strain across the structure) of the bulk modulus of hexagonal crystal is written as:

$$B_0 = \frac{1}{9}(2c_{11} + c_{33} + 2c_{12} + 4c_{13}) \tag{7.21}$$

The Reuss average (assuming constant stress across the structure) of the bulk modulus of hexagonal crystal is:

$$B = \frac{c_{33}(c_{11} + c_{12}) - 2c_{13}^2}{c_{11} + c_{12} + 2c_{33} - 4c_{13}} \tag{7.22}$$

The difference between Voigt and Reuss average is manifest in estimating the elastic properties of the composite materials. We need to understand the bulk modulus obtained in EOS. In practise, I found Voigt average is not the proper definition of the bulk modulus of single crystal in EOS. I use Eq. 7.22 in my calculation. This can also be found in Ref. [100].

One can find several different designs of strain tensor to calculate elastic constants of hexagonal crystal in the literatures. One set of the strain is very straight forward:

$$\eta_{ij} = \begin{pmatrix} \delta & 0 & 0 \\ 0 & \delta & 0 \\ 0 & 0 & 0 \end{pmatrix}$$

which gives: $E = E_0 + V_0(c_{11} + c_{12})\delta^2$

$$\eta_{ij} = \begin{pmatrix} \delta & 0 & 0 \\ 0 & -\delta & 0 \\ 0 & 0 & 0 \end{pmatrix}$$

which gives: $E = E_0 + V_0(c_{11} - c_{12})\delta^2$

$$\eta_{ij} = \begin{pmatrix} 0 & 0 & 0 \\ 0 & 0 & 0 \\ 0 & 0 & \delta \end{pmatrix}$$

which gives: $E = E_0 + \frac{1}{2}V_0 c_{33}\delta^2$

$$\eta_{ij} = \begin{pmatrix} 0 & 0 & \delta \\ 0 & 0 & 0 \\ \delta & 0 & 0 \end{pmatrix}$$

which gives: $E = E_0 + \frac{1}{2}V_0 c_{33}\delta^2$. These four strains together with the bulk modulus can give all five elastic constants.

Another method is presented by Steinel-Neumann [100]. The authors utilize strain:

$$\eta_{ij} = \begin{pmatrix} \delta & 0 & 0 \\ 0 & \delta & 0 \\ 0 & 0 & (1+\delta)^{-2} - 1 \end{pmatrix}$$

which give: $E = E(V_0, 0) + V c_s \delta^2 + O(\delta^3)$, with $c_s = c_{11} + c_{12} + 2c_{33} - 4c_{13}$.

$$\eta_{ij} = \begin{pmatrix} \delta & 0 & 0 \\ 0 & -\delta & 0 \\ 0 & 0 & \delta^2/(1-\delta^2) \end{pmatrix}$$

which gives: $E = E(V_0, 0) + 2V c_{66}\delta^2 + O(\delta^4)$

$$\eta_{ij} = \begin{pmatrix} 0 & 0 & \delta \\ 0 & \delta^2/(1-\delta^2) & 0 \\ \delta & 0 & 0 \end{pmatrix}$$

which gives: $E = E(V_0, 0) + 2V c_{44}\delta^2 + O(\delta^4)$.

The last equation is about the dimensionless quantity R:

$$R = B(k_a - k_c) = -\frac{d\ln(c/a)}{d\ln V} = \frac{c_{33} - c_{11} - c_{12} + c_{13}}{c_{11} + c_{12} + 2c_{33} - 4c_{13}} \tag{7.23}$$

R can be fitted through the c/a-ratio vs. V curve. For graphite, the fitting can be found in Fig. 7.4d

I calculated elastic constant of graphite, MoS_2, and misfit layered compound. Using graphite as an example, Fig. 7.1 shows the convergence test using different energy cutoff and mesh in `KPOINTS`. From the convergence test I choose to use $16 \times 16 \times 8$ `KPOINT` and 1000 `ENCUT` in later calculation. The energy difference in the convergence test using this set up is 6×10^{-5}

eV/atom.

I first use local-density approximation (LDA). Figure 7.2 shows the calculated energy for each calculation. The energy points with only 1 ionic step are fitted with EOS. The fitting gives the bulk modulus of graphite and lattice constants of the unit cell. Using the fitted lattice constants, the structure is relaxed again until one ionic step. The final `CONTCAR` is used as structure of graphite (`POSCAR`) in the calculation of elastic constants.

Graphite is a special hexagonal crystal because of the Van der Waals force between atomic layers. Typically DFT cannot calculate Van der Waals interaction accurately. Several approximations have been introduced to correct this error. I chose to use Tkatchenko-Scheffler method implemented in `VASP`. However for LDA, I didn't use any van der Waals approximation. This is because the Tkatchenko-Scheffler method (`IVDW=2`) doesn't have parameters of elements for LDA potential. The final results agree superisingly well with experimental values. This behavior has also been noticed before. And people conclude that this is just a coincidence.

For GGA potential, however, the calculation won't reach to a reasonable structure without Van der Waals correction. The failure of GGA in calculation of graphite is also confirmed in several papers. I repeat the calculation using GGA potential together with Tkatchenko-Scheffler (TS) van der Waals approximation (`IVDW=2`). `VASP` has implemented default parameters of elements for TS Van der Waals approximation. The calculation follows the same procedure as the one with LDA potential.

Fig. 7.3 shows all four energy vs. strain curves under LDA and the fitting, using the first set of strains. The fitting using the second set of strain is shown in Fig. 7.4. I found the results using the two different sets of strains are almost identical.

A subtle but important behavior I observed in the calculation of graphite is that: for strain that doesn't preserve the hexagonal symmetry, the calculation shows small difference comparing with the calculation with symmetry simplification. `VASP` can determine the symmetry of the crystal with certain tolerance. But the symmetry simplification can be turned off in `VASP`. In calculation of c_{44}, since the energy change involved is very small and the strain applied doesn't conserve the symmetry of crystal, I have to remove the symmetry simplification when there is zero strain. Or otherwise the numerical error (I think) will make the energy vs. strain curve not a parabola. The

comparison can be found in Fig. 7.5.

For layered structure, the force between layers is very small comparing with the in-plain modulus. So the bulk modulus is basically c_{33}. (c_{33} is the interlayer elastic constants). This can be seen from both the calculation and the experiment result. Difference in c_{33} between my two calculations reflects the effect of Van der Waals functional used in GGA calculation. Bulk modulus (and c_{33}) deviates with experiment. The bulk modulus from LDA is closer.

I summarized my calculation of single crystal graphite, experiment on exfoliated HOPG, and results from other experiment and calculation in Table 7.1. I only include calculations done by `VASP`. For GGA potential with TS-vdW, since TS-vdW approximation is relatively new (the paper is published in 2009, and the implementation in VASP is about 2012), I didn't find paper calculating the complete set of elastic constants using TS-vdW and GGA. From the comparison of lattice constants and bulk modulus, my calculation is consistent with other calculations.

I did notice one problem in the fitting: the disagreement of energy minimum between the energy sweep and calculation with strain. It mostly happens for GGA calculation. But it also happens in c_{33} calculation using LDA. The disagreement is shown in figure 7.6

Recall that in calculation of c_{44}, I need to turn off the symmetry (`ISYM=0`) in no strain case in order to compare with the calculation with strain (doesn't conserve symmetry). I try to turn off the symmetry in both volume sweep and c_{33} calculations, but the result remain unchanged. The comparison is in Fig. 7.7. I also try to increase the accuracy in calculation of force (`EDIFFG`). I increased it from default 10^{-5} to 10^{-6} and 10^{-7}, the energy vs. strain curve is still not symmetrical around zero strain. (with such high `EDIFFG`, I cannot calculate $c_{11} - c_{12}$. The software just give errors)

However, as can be seen from Fig. 7.7, the difference is tiny: ≈ 0.00001 eV. Although I couldn't figure out what cause this difference, I think it can be ignored right now as it is very small comparing with the typically accuracy in DFT calculation.

The calculation of MoS_2 is identical with the case of graphite. The calculation and experimental results are summarized in Table 7.2.

7.3 Calculation of phonon of silicon

Since mode Grüneisen parameter is defined based on phonon, in this section I describe the procedure of phonon calculation in Si.

7.3.1 Lattice dynamics in crystal

In solid state physics, phonon is used to describe the movement of atom, not in the real space but in frequency domain. I will sketch the basic theory of lattice dynamics in this section. Consider the κ atom located at unit cell l moves around its equilibrium position $\mathbf{R}_0(l\kappa)$ with displacement $\mathbf{u}(l\kappa)$. Here l and κ are written together to identify one particular atom, which is similar to the case when i and j are written together to identify a component such as η_{ij}. The instantaneous position of this atom can be written as:

$$\mathbf{R}(l\kappa) = \mathbf{r}_l + \mathbf{r}_\kappa + \mathbf{u}(l\kappa) = \mathbf{R}_0(l\kappa) + \mathbf{u}(l\kappa) \tag{7.24}$$

where $\mathbf{r}_l$ is the position of unit cell and $\mathbf{r}_\kappa$ is the position of atom within the unit cell. The Hamiltonian of nuclear motion (since most of the atom mass is in the nucleus) is:

$$H = \sum_{l\kappa} \frac{P^2(l\kappa)}{2m_\kappa} + \Phi(\mathbf{r}_{l_1\kappa_1}, \mathbf{r}_{l_2\kappa_2}, ...) \tag{7.25}$$

The first term is the kinetic energy and the second term is the potential energy due to interaction between atoms. The crystal potential energy Φ can be written as a function of the displacement of the atoms (Taylor expansion with respect to the equilibrium position):

$$\Phi = \phi_0 + \sum_{l\kappa}\sum_{\alpha} \phi_\alpha(l\kappa)u_\alpha(l\kappa) + \frac{1}{2}\sum_{ll'\kappa\kappa'}\sum_{\alpha\beta} \phi_{\alpha\beta}(l\kappa, l'\kappa')u_\alpha(l\kappa)u_\beta(l'\kappa') + ... \tag{7.26}$$

where α and β are the Cartesian indices ranging from 1 to 3. The coefficient of this series expansion, ϕ_0, $\phi_\alpha(l\kappa)$, $\phi_{\alpha\beta}(l\kappa, l'\kappa')$, etc. are the zeros, first, and second order force constants respectively.

The zero order term is a constant energy term and can be omitted in the current situation. At equilibrium, the first order term is zero since the

net force on atoms is zero at equilibrium. If the displacement is considered small, the harmonic approximation is reached and the terms higher than the second order is omitted. The only term left is the 3×3 second order force constant $\phi_{\alpha\beta}(l\kappa, l'\kappa')$ corresponding to each atom pair $(l\kappa; l'\kappa')$. And the crystal Hamiltonian can be simplified under harmonic approximation as:

$$H = \sum_{l\kappa} \frac{P^2(l\kappa)}{2m_\kappa} + \frac{1}{2} \sum_{ll'\kappa\kappa'} \sum_{\alpha\beta} \phi_{\alpha\beta}(l\kappa, l'\kappa') u_\alpha(l\kappa) u_\beta(l'\kappa') \tag{7.27}$$

Since it's the dynamic we are interested in, the equation of motion is at the center. The equation of motion for all nuclei in the real space are (classic mechanics):

$$m_\kappa \frac{\partial^2 u_\alpha(l\kappa)}{\partial t^2} = -\sum_{l',\kappa'} \phi_{\alpha\beta}(l\kappa, l'\kappa') u_\beta(l'\kappa') \tag{7.28}$$

Following the standard method to solve partial differential equations, plane waves are used to find the general solutions (just like in Chapter 3). In another word, the problem is solved in the frequency domain and spatial frequency domain rather than the time domain and spacial domain. For plane wave with wavevector $\mathbf{q}$, angular frequency $\omega_{\mathbf{k}j}$, and "polarization" $\mathbf{e}(\mathbf{q}j\kappa)$ with j as a "branch index", the displacement can be written as supperposition of plane waves:

$$\mathbf{u}(l\kappa) = \frac{1}{\sqrt{V}} \sum_{\mathbf{q}j} U(\mathbf{q}j\kappa) \mathbf{e}(\mathbf{q}j\kappa) \exp[i(\mathbf{q}\mathbf{r}_l - \omega_{\mathbf{q}j} t])} \tag{7.29}$$

This design of supperposition is not trivial. It's based on the Bloch theorem of crystal. The Bloch theorem confines the relevant $\mathbf{q}$ to be inside the first Brillouin zone. If the periodic boundary condition is applied to the problem and each unit cell contains $\mathcal{R}$ atoms, there are total $3\mathcal{R}$ modes for each wavevector $\mathbf{q}$, $1 \leq j \leq 3\mathcal{R}$. The phase factor $\exp(i\mathbf{q}\mathbf{r}_l)$ contains the information of long-range spatial modulation across unit cell (thus using the position $\mathbf{r}_l$). The dependence with κ, i.e. within the unit cell, is contained inside the complex $\mathbf{e}(\mathbf{q}j\kappa)$. $U(\mathbf{q}j\kappa)$ is related with the energy of phonon which is not derived here. The unit vector $\mathbf{e}(\mathbf{q}j\kappa)$ contains information of the motion of each atom within the unit cell for phonon mode $\mathbf{q}j$. It gives the displacement direction (thus "polarization") and the phase of each atoms (thus it's complex). So one can distinguish acoustic phonon and optical phonon by the

phase difference between atoms within one unit cell.

The next step is to solve for phonon dispersion curve (ω vs. $\mathbf{q}$). Put Eq. 7.29 back into EOM Eq. 7.28 (Fourier transform of the original partial differential equation), the EOM becomes a set of linear algebraic equations (very similar to the case in Chapter 3). The problems becomes a standard eigenvalue problem regarding the *dynamic matrix* $D(\mathbf{q})$ with $(3\mathcal{R} \times 3\mathcal{R})$ dimensions:

$$D(\mathbf{q}) = \begin{pmatrix} D_{11} & ... & D_{1\mathcal{R}} \\ ... & ... & ... \\ D_{\mathcal{R}1} & ... & D_{\mathcal{R}\mathcal{R}} \end{pmatrix}$$

Each submatrix $D_{\kappa\kappa'}$ is the Fourier transform of the second order force constant $\phi(l\kappa, l'\kappa')$ with (3×3) dimensions:

$$D_{\kappa\kappa'}(\mathbf{q}) = \frac{1}{\sqrt{m_\kappa m_{\kappa'}}} \sum_{l'} \phi(0\kappa, l'\kappa') \exp(i\mathbf{q}(\mathbf{r}_{l'} - \mathbf{r}_0)) \tag{7.30}$$

The eigenvector of the dynamic matrix is the similar grouping of the polarization vectors $\mathbf{e}(\mathbf{q}j\kappa)$ across all atoms within unit cell to be a $(3\mathcal{R} \times 1)$ vector $p(\mathbf{q}j)$; the eigenvalue is $\omega^2_{\mathbf{q}j}$. The eigenvalue problem is:

$$D(\mathbf{q})p(\mathbf{q}j) = \omega^2_{\mathbf{q}j} p(\mathbf{q}j) \tag{7.31}$$

Solving this linear algebraic equation, one can obtain phonon frequency $\omega_{\mathbf{q}j}$ corresponding to wavevector $\mathbf{q}$ and branch j.

7.3.2 First principle calculation of phonon

Calculation procedure of phonon dispersion in the ab initio fashion can be outlined based on the theory in last section: 1. calculate the second order force constants; 2. obtain dynamic matrix by Fourier transform of the force constants; 3. solve the eigenvalues of the dynamic matrix to obtain phonon frequencies.

The force on a particular atom $(l\kappa)$ can be written, with the harmonic approximation, as:

$$F_\alpha(l\kappa) = -\frac{\partial \Phi}{\partial u_\alpha(l\kappa)} \tag{7.32}$$

and the second-order force constant can be related with the force as:

$$\phi_{\alpha\beta}(l\kappa, l'\kappa') = \frac{\partial^2 \Phi}{\partial u_\alpha(l\kappa)\partial u_\beta(l'\kappa')} = -\frac{\partial F_\beta(l'\kappa')}{\partial u_\alpha(l\kappa)} \tag{7.33}$$

There are generally two methods to calculate the force constant in DFT: finite displacement method and density-functional perturbation theory (DFPT). In finite displacement method, one atom is artificially displaced in an equilibrium structure and the force between atoms are calculated by DFT. Then the force constant is calculated under finite difference approximation using Eq. 7.33. In DFPT method, the force constants are directly calculated by DFT. `VASP` incorporated DFPT method in its software so this is also a convenient method. The finite displacement method is a straightforward and easy to understand method which is often called the direct method. I mainly use finite displacement method to calculate the phonon dispersion of Si. I have also used DFPT method and find it gives very similar results for Si.

The open source software `phononpy` is used in the calculation process process. `phononpy` decides how many displacement is needed in order to calculate all phonon modes, based on the symmetry of the crystal. `phononpy` records the displacement and create the new `POSCAR` for force calculation. After the force is calculated by `VASP`, `phononpy` conduct the Fourier transform and solving eigenvalue problem, thus output phonon frequencies. In the end I write my own scripts to do final data analysis and plots.

In practise, the assumption of short range interaction is needed, which means the interaction between atoms can be omitted beyond n nearest neighbor where n is small. This is necessary because a very large supercell is too expansive to calculate in DFT. Also in the calculation, the periodic boundary condition is applied. By moving one particular atom, every other atom that mirrors this atom will also be moved. This can possibly cause error in finite displacement method. So one needs to find the supercell that is large enough so the two problem mentioned can be omitted.

7.3.3 Si phonon dispersion calculated by finite displacement method using VASP

Before one atom is artificially displaced, the equilibrium crystal structure of Si is obtained by fitting the EOS, through standard DFT calculation de-

scribed before. The the finite displacement method is applied to the fully relaxed unitcell.

As pointed out in Sec. 7.3.2, one of the most important parameters to determine in the calculation is the size of the supercell. So the "convergence test" is performed to determine the proper size. Fig. 7.8 shows that $4 \times 4 \times 4$ supercell gives almost same results as $5 \times 5 \times 5$ supercell. Calculation using $5 \times 5 \times 5$ supercell is also very computational expansive. So I chose supercell of $4 \times 4 \times 4$. Notice that the biggest difference is at the acoustic phonon branch. This point is mentioned again later. I think this is an inherent difficulty in calculation of phonon by DFT: an accurate calculation of acoustic phonon requires accurate calculation of force, which can be very challenging. I did similar convergence test to determine both `ENCUT` and `KPOINTS`. From the convergence test I chose `ENCUT=400` and k-mesh to be $4 \times 4 \times 4$

Using these parameters, I calculated phonon dispersion of Si. Fig. 7.9 shows the comparison between my calculation and experimental results [101]. It shows my calculation agrees very well with measurements.

7.4 Calculation of generalized Mode Grüneisen parameters of Si

Chapter 6 discusses experimental results regarding the attenuation of SAW. It shows that attenuation of shear acoustic wave is much less than attenuation of longitudinal acoustic wave. And according to the fitting results, the difference is mostly in generalized mode Grüneisen parameters of Si. To better understand this phenomenon, I calculate the generalized mode Grüneisen parameters of Si using DFT calculation.

7.4.1 Mode Grüneisen parameter of Si

The mode Grüneisen parameter is defined as:

$$\gamma_p = \frac{V}{\omega_p} \frac{\partial \omega_p}{\partial V} \tag{7.34}$$

where V is the volume of the lattice and ω_p is the phonon frequency of mode p. In real calculation, the derivative is replaced by finite difference. Then

the definition becomes:

$$\gamma_p = \frac{\Delta\omega_p/\omega_p}{\Delta V/V} \tag{7.35}$$

In the calculation, I change the volume of lattice V by ΔV and calculate the phonon frequency before and after the volume change, using the finite displacement method described before. The ratio of the relative change of phonon frequency and volume is the mode Grüneisen parameter. To check the assumption of linearity and finite difference, I choose relative change of volume to be 0.3 percent, 0.6 percent, and 0.9 percent. Fig. 7.10 shows the results of my calculation (colored line) of three different volume change, comparing with the calculation in Ref. [102] (black dots). The calculation converges in the sense that different volume change won't result in different Grüneisen parameters. And my calculation results is in reasonable agreements with results of others. This also means the volume change I choose is proper.

7.4.2 Generalized mode Grüneisen parameters of Si

The definition of generalized mode Grüneisen parameter is the change of phonon frequency to a particular strain applied to the crystal. It can be written as:

$$\gamma_p^{ij} = \frac{1}{\omega_p}\frac{\partial\omega_p}{\partial\eta_{ij}} \tag{7.36}$$

where ω_p is the angular frequency of phonon mode p. η_{ij} is the component of Lagrange strain tensor. Similar as before, in finite difference approximation, the definition becomes:

$$\gamma_p^{ij} = \frac{\Delta\omega_p/\omega_p}{\eta_{ij}} \tag{7.37}$$

To calculate generalized mode Grüneisen parameter, the straightforward procedure is: first a particular strain mode is applied to the lattice; and then the new phonon dispersion under strain is compared with the original phonon dispersion and generalized mode Grüneisen parameters can be calculated for each phonon mode. However as I will show later, there needs to be some modification to this process due to a possible numerical inaccuracy.

After a particular strain is applied, the lattice should not be relaxed. For example, if a longitudinal strain is applied at x direction, the lattice cannot be relaxed at the y and z direction. This is because the definition

of Grüneisen parameter is based on the derivative with regard to one strain component. If the crystal is relaxed at other directions, it introduces other strain components that are not under consideration.

For example, when a normal strain δ at x_3 direction is applied to the fulled relaxed cell, just like how it is applied in the calculation of elastic constants.

$$\eta_{ij} = \begin{pmatrix} 0 & 0 & 0 \\ 0 & 0 & 0 \\ 0 & 0 & \delta \end{pmatrix}$$

The cell cannot relax at x_1 and x_2 directions, i.e., η_{11} and η_{22} should be zero to study the effect of η_{33}.

To compute generalized mode Grüneisen parameters, I compare the change of phonon frequencies due to the strain applied. I discovered a serious problem. Fig. 7.11 shows the comparison of phonon frequency with 0%, +1%, +2%, and +3% normal strain. For optical phonons, the changes of phonon frequencies is linear with the change of strain. However for acoustic phonon branches, although the frequencies change looks almost linear between +1%, +2%, and +3% strain, it is not if one consider the zero strain case. This can be observed by the zoom-ined Fig. 7.12. Fig. 7.13 shows the comparison of phonon frequencies with -1%, 0%, and +1%. One can see that if only these three points are considered, they are linear. But it's definitely not linear if strains with different magnitude are included. This phenomenon means that: if the generalized mode Grüneisen parameter is calculated by comparing with the zero strain case, the results will be dependent on the magnitude of strain. It is still the case if one uses positive and negative strains, because the phonon frequencies of zero strain are in the center of phonon frequencies of positive and negative strains.

The non-linearity of acoustic phonon frequency change with strain is certainly not physical. And this is not a human error, because it only happens for acoustic branch not optical branch. Also this problem is not in the case of hydrostatic strain, as I show in Fig. 7.10. And this non-linearity happens between zero and non-zero strain but not between non-zero strains. So there is difference between calculation of zero strain lattice and non-zero strain lattice in non-hydrostatic strain case. But this difference disappears for hydrostatic strain case. I think these indicate this difference is symmetry related, since for non-hydrostatic strain, the symmetry of lattice changes;

while in hydrostatic strain the symmetry of lattice is preserved.

One possible solution to this problem, is to only use the linearity between non-zero strains with the same sign. Fig. 7.14 shows the generalized mode Grüneisen parameter of Si under normal strain.

7.5 Third order elastic constant and mode Grüneisen parameters

The full generalized mode Grüneisen parameters cannot be directly measured experimentally. The measurement of third order elastic constant (TOEC) represents behavior of generalized mode Grüneisen parameter at Γ point for acoustic phonon branches. During my work, I found that the relationship between TOEC and generalized mode Grüneisen parameter is not straightforward at all. It involves derivations and theories that are not familiar to me or maybe many students in physics or material science major. This derivation was done by Thurston and Brugger [103, 104] in a series of papers. I don't have any new contribution to the original theory. However I would like to present the full derivation of the related theories, as the original papers didn't contain most of the details which are not trivial in my opinion. Hopefully this derivation is helpful to anyone who, like me, has been misled by wrong derivation results in journals and books before.

This derivation is also the reason why I revisit some of the concept in solid mechanics. TOEC is an experimental results and we need to think about how the experiment is done. Previously I introduced two coordinate system, the unstrained one and the one with strain. Now as we will discuss acoustic wave in strained material, we need to consider three coordinate system. For initial temperature T, a_i is the coordinates in the natural or unstressed state; $X_i(a_j)$ is the coordinate in homogeneously stressed initial state; $u_i = x_i - X_i$ is the component of displacement from initial strained state due to the acoustic wave.

Consider the material that is under homogeneous strain. To construct the equation of motion in a deformed material, Cauchy stress tensor describes the physical force:

$$\rho \frac{\partial^2 x_j}{\partial t^2} = \frac{\partial \tau_{kj}}{\partial x_k} \tag{7.38}$$

Notice the density involved is density ρ of the deformed state which can be different with density ρ_0 of undeformed material. We want to describe the problem in the original coordinates. The method to achieve this is to use the various stress measure introduced before.

Recall the second order Piola-Kirchhoff stress t_{pq} that satisfies:

$$\tau_{kj} = \frac{1}{J}\frac{\partial x_k}{\partial q_p}\frac{\partial x_j}{\partial a_q}t_{pq} \tag{7.39}$$

Substitute τ_{kj} and utilize the properties listed in first section, we obtain the equation of motion using density and coordinates of undeformed states:

$$\rho_0\frac{\partial^2 x_j}{\partial t^2} = \frac{\partial P_{jp}}{\partial a_p} \tag{7.40}$$

and $P_{jp} = F_{jp}t_{pq}$ is the first Piola-Kirchhoff stress tensor. Expand P_{jp} about the initial state P^0_{jp} of coordinates X_i:

$$P_{jp} - P^0_{jp} = \frac{\partial P_{jp}}{\partial(\partial x_k/\partial a_m)}(\frac{\partial x_k}{\partial a_m} - \frac{\partial X_k}{\partial a_m}) + ... = A^0_{jkpm}\frac{\partial u_k}{\partial a_m} \tag{7.41}$$

with $A^0_{jkpm} \equiv \frac{\partial P^0_{jp}}{\partial(\partial x_k/\partial a_m)}$. Since the strain applied to the material is homogeneous, the first Piola-Kirchhoff stress is uniform through the material: $\partial P^0_{jp}/\partial a_p = 0$ and $\partial A^0_{jkpm}/\partial a_p = 0$. The equation of motion is:

$$\rho_0\frac{\partial^2 u_j}{\partial t^2} = \frac{\partial}{\partial a_p}\left[P^0_{jp} + A^0_{jkpm}(\frac{\partial x_k}{\partial a_m} - \frac{\partial X_k}{\partial a_m})\right] = A^0_{jkpm}\frac{\partial^2 u_k}{\partial a_p \partial a_m} \tag{7.42}$$

The coefficient A_{jkpm} can be expressed as:

$$\begin{aligned}
A_{jkpm} \equiv \frac{\partial P_{jp}}{\partial F_{km}} &= \frac{\partial (F_{jq} t_{pq})}{\partial F_{km}} = \delta_{jk} t_{pm} + F_{jq} \frac{\partial t_{pq}}{\partial F_{km}} \\
&= \delta_{jk} t_{pm} + F_{jq} \left[\sum_{i \neq m} \frac{\partial t_{pq}}{\partial \eta_{mi}} \frac{\partial \eta_{mi}}{\partial F_{km}} + \sum_{i \neq m} \frac{\partial t_{pq}}{\partial \eta_{im}} \frac{\partial \eta_{im}}{\partial F_{km}} + \frac{\partial t_{pq}}{\partial \eta_{mm}} \frac{\partial \eta_{mm}}{\partial F_{km}} \right] \\
&= \delta_{jk} t_{pm} + F_{jq} \left[\frac{1}{2} \sum_{i \neq m} \frac{\partial t_{pq}}{\partial \eta_{mi}} F_{ki} + \frac{1}{2} \sum_{i \neq m} \frac{\partial t_{pq}}{\partial \eta_{im}} F_{ki} + \frac{\partial t_{pq}}{\partial \eta_{mm}} F_{km]} \right] \\
&= \delta_{jk} t_{pm} + F_{jq} F_{ki} \frac{\partial t_{pq}}{\partial \eta_{mi}} \\
&= \delta_{jk} t_{pm} + F_{jq} F_{ki} \left[\rho_0 \frac{\partial^2 U}{\partial \eta_{pq} \partial \eta_{mi}} \right] \\
&= \delta_{jk} t_{pm} + F_{jq} F_{ki} c_{pqmi}
\end{aligned} \tag{7.43}$$

So $A^0_{jkpm} = \delta_{jk} t^0_{pm} + F^0_{jq} F^0_{ki} c_{pqmi}$, where F^0_{ij} is the deformation tensor of the original homogeneous strain.

Next we assume the plane wave solution: $u_j = M_j \exp[i\omega(t - (N_i a_i / W))]$. The wave front is a material plane which has unit normal N_i in the natural state; a wave front moves from the plane $N_i a_i = 0$ to $N_i a_i = L$ in the time L/W, where W is the wave speed referred to the natural dimensions and it is called the natural velocity for propagation normal to a plane of natural normal N_i. Put the plane wave solution back to the equation of motion, one obtains:

$$\rho_0 W^2 u_j = A^0_{jkpm} N_p N_m u_k \tag{7.44}$$

So the $\rho_0 W^2$ are the eigenvalues of the second rank tensor

$$S_{jk}(N_i) \equiv A^0_{jkpm} N_p N_m \tag{7.45}$$

To obtain a representation completely independent of rotation, transform the particle displacement u_i back to the natural undeformed direction of the material line along it by the transformation $u_i = (\partial X_i / \partial a_q) U_q$. Then

$$\rho_0 W^2 U_j = w_{jk} U_k \tag{7.46}$$

with:

$$\begin{aligned} w_{jk} &= \frac{\partial a_j}{\partial X_r}\frac{\partial X_s}{\partial a_k}S_{rs} = \frac{\partial a_j}{\partial X_r}\frac{\partial X_s}{\partial a_k}A^0_{rspm}N_pN_m \\ &= \frac{\partial a_j}{\partial X_r}\frac{\partial X_s}{\partial a_k}\left[\delta_{jk}t^0_{pm} + F^0_{jq}F^0_{ki}c_{pqmi}\right]N_pN_m \\ &= N_pN_m\left[\delta_{jk}t^0_{pm} + \frac{\partial a_j}{\partial X_r}\frac{\partial X_s}{\partial a_k}\frac{\partial X_r}{\partial a_q}\frac{\partial X_s}{\partial a_i}c_{pqmi}\right] \\ &= N_pN_m[\delta_{jk}t^0_{pm} + (2\eta_{ki} + \delta_{ki})\delta_{kj}c_{pqmi})] \\ &= N_pN_m[\delta_{jk}t^0_{pm} + (2\eta_{ki} + \delta_{ki})c_{pjmi})] \end{aligned} \tag{7.47}$$

The above is how Brugger [104] arrives at the equation:

$$\rho_0 W^2 U_u = w_{uv}U_v \tag{7.48}$$

with:

$$w_{uv} = [\delta_{uv}t^0_{mn} + (\delta_{vw} + 2\eta^0_{vw})c_{munw}]N_mN_n \tag{7.49}$$

again, N_i is the propagation direction, U_i is displacement unit vector, W is the acoustic velocity, all in unstrained reference; t_{mn} is the thermodynamic tension, η_{vw} is Lagrange strain, c_{munw} is elastic constant, in deformed state.

The definition of generalized mode Grüneisen parameter can be rewritten as:

$$\gamma^{(jk)}_p(N_i) = -\frac{1}{2\omega_p(N_i)}\frac{\partial[\rho_0 W^2_p(N_i)]}{\partial\eta_{jk}} \tag{7.50}$$

with $\omega_p = \rho_0 W^2$ evaluated at no strain state $\eta = 0$. Since U_i is the unit vector, and $\rho_0 W^2 \bar{U}^T\bar{U} = \bar{U}^T w\bar{U}$, i.e. $\rho_0 W^2 = U_uU_vw_{uv}$. Thus at $\eta = 0$ case, $\omega_p = c_{munv}U_uU_vN_mN_n$.

The next is the final step of the derivation is to connect Grüneisen

parameter with the TOEC:

$$\begin{aligned}
\gamma_p^{(jk)}(N_i) &= -\frac{1}{2\omega_p}\left[\delta_{uv}\frac{\partial t^0_{mn}}{\partial \eta_{jk}} + \delta_{vw}\frac{\partial c_{munw}}{\partial \eta_{jk}} + 2\frac{\partial(\eta_{vw}c_{munw})}{\partial \eta_{jk}}\right] N_m N_n U_v U_u \\
&= -\frac{1}{2\omega_p}[c_{jkmn}N_m N_n + \delta_{vw}c_{jkmunw}N_m N_n U_u U_v + \\
&\quad 2\eta_{vw}c_{jkmunw}N_m N_n U_u U_v + 2c_{munw}\frac{\partial \eta_{vw}}{\partial \eta_{jk}}N_m N_n U_u U_v] \\
&= -\frac{1}{2\omega_p}[(c_{jkmn} + c_{jkmunv}U_u U_v)N_m N_n + 2c_{munw}\delta_{vj}\delta_{wk}N_m N_n U_u U_v] \\
&= -\frac{1}{2\omega_p}[(c_{jkmn} + c_{jkmunv}U_u U_v)N_m N_n + 2c_{munk}N_m N_n (U_u/U_k)U_k U_j] \\
&= -\frac{1}{2\omega_p}[2\omega_p U_j U_k + (c_{jkmn} + c_{jkmunv}U_u U_v)N_m N_n]
\end{aligned} \tag{7.51}$$

This is the key equation derived by Brugger about the relationship between generalized mode Grüneisen parameters and TOEC.

7.6 Calculation settings in `VASP`

Following is the typical calculation parameters I used in `INCAR` file in elastic constant calculations for graphite. In volume sweep (to fit EOS), `ISIF=4`. When calculating energy with strain applied, `ISIF=2` to preserve the strain. Here I specify `EDIFFG` to be 10 times more accurate than default, which is `10*EDIFF`.

```
PREC = High
LREAL = .FALSE
IALGO = 48
ISMEAR = 0; SIGMA = 0.0001
ENCUT = 1000

EDIFF = 1.E-6
EDIFFG = 1.E-6
NBANDS = 48

```

```
ISIF = 4 (or 2)
IBRION = 2
NSW = 100
```

Next is the typical calculation parameters I used in `INCAR` file to calculate force constant in order to calculate phonon frequencies of Si, using finite displacement method. Since one atom is displaced, during calculation, there shouldn't be any relaxation of ionic positions.

```
PREC = Accurate
LREAL = .FALSE

ISMEAR = 0; SIGMA = 0.00001
ENCUT = 400
ADDGRID = TRUE

EDIFF = 1.E-8

ISIF = 2
IBRION = -1
NSW = 0
```

7.7 Figures and tables

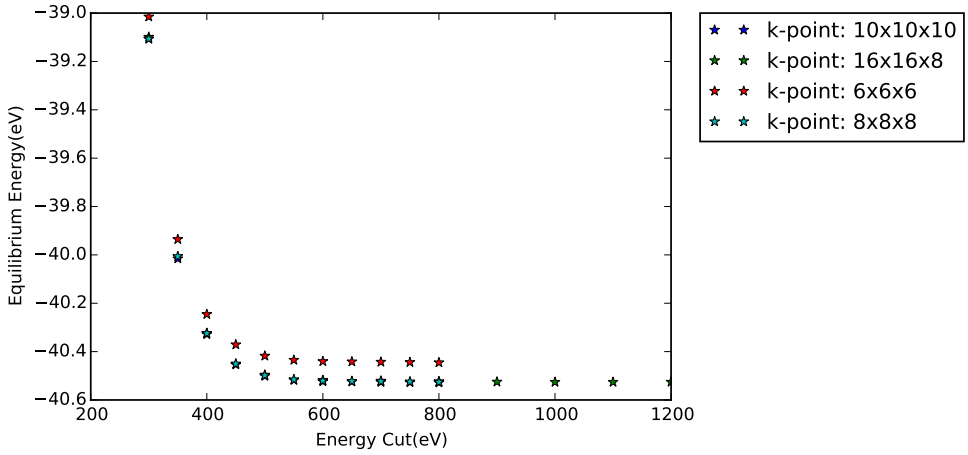

Figure 7.1: Convergence test of calculation of graphite (LDA).

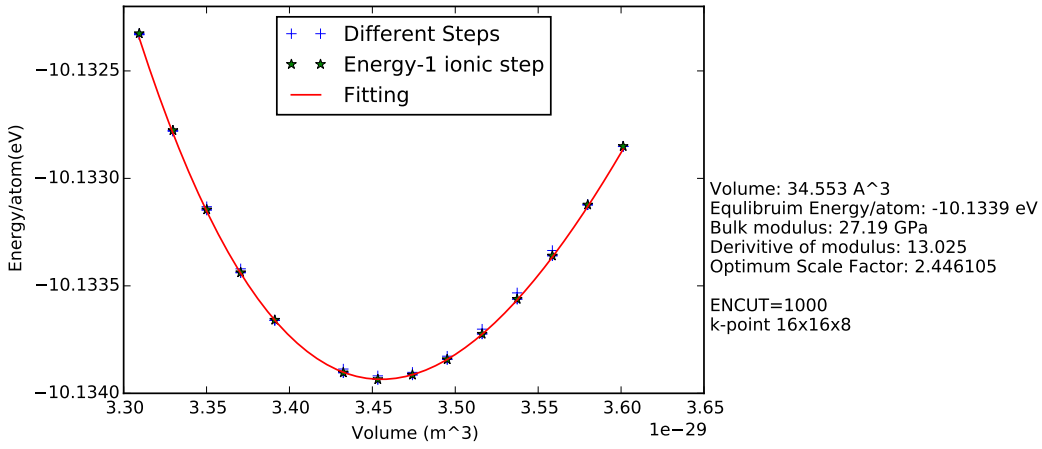

Figure 7.2: Fitting of EOS for graphite. "Volume" means the optimal volume of the unit cell. The cross symbol is each calculation with more than one ironic step. The star is the final calculation with only one ionic step. The red line is the fitting of star symbols using equation of states.

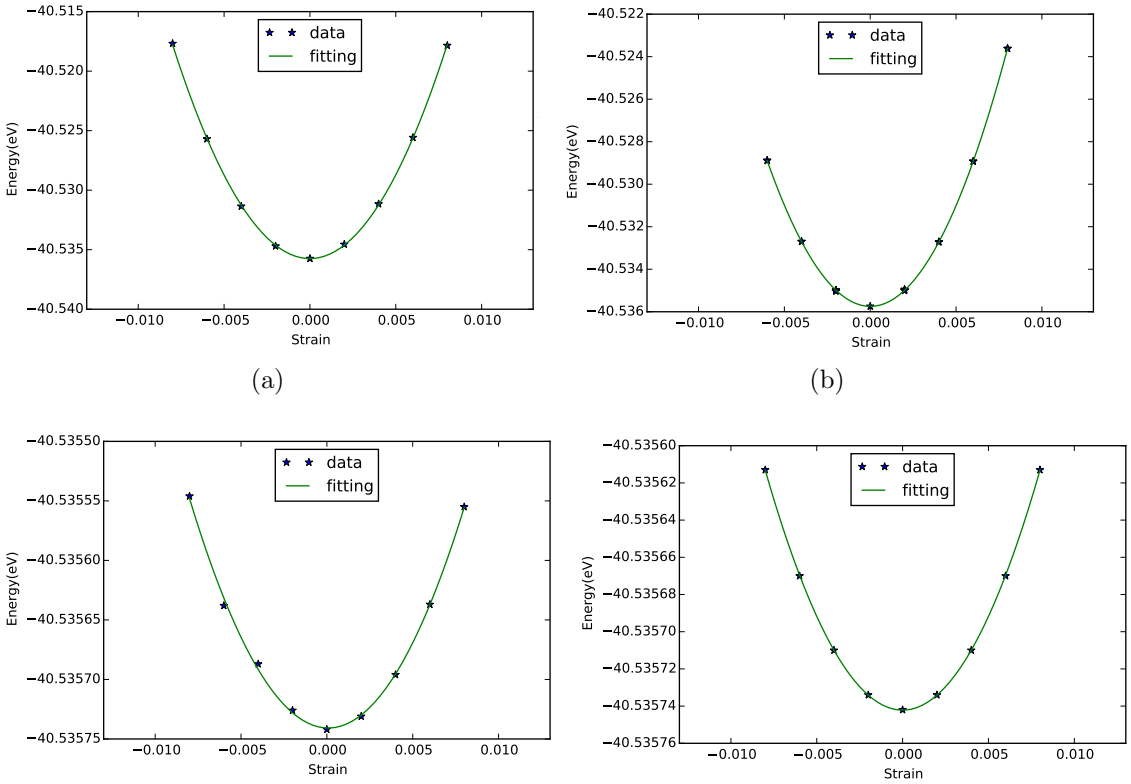

Figure 7.3: Fitting of energy vs. strain curve in graphite for different strains (in method 1) applied, in order to obtain (a). $c_{11} + c_{12}$, (b). $c_{11} - c_{12}$, (c). c_{33}, (d). c_{44}.

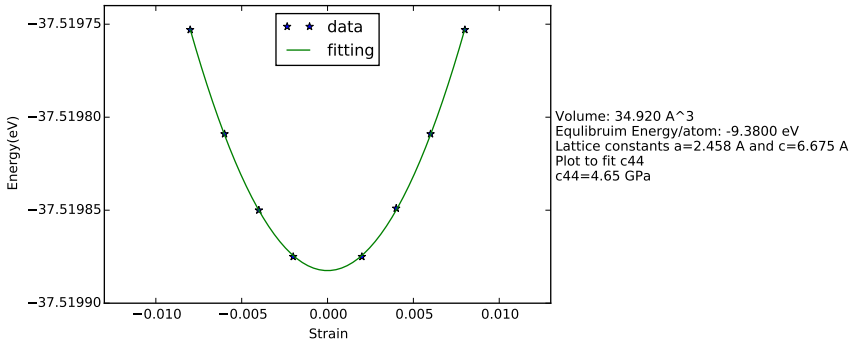

(a)

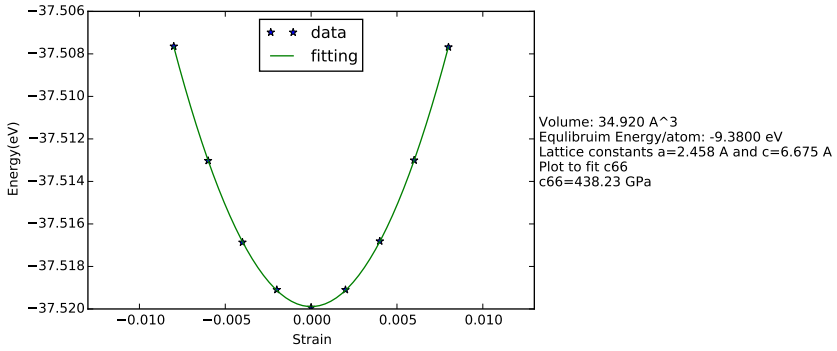

(b)

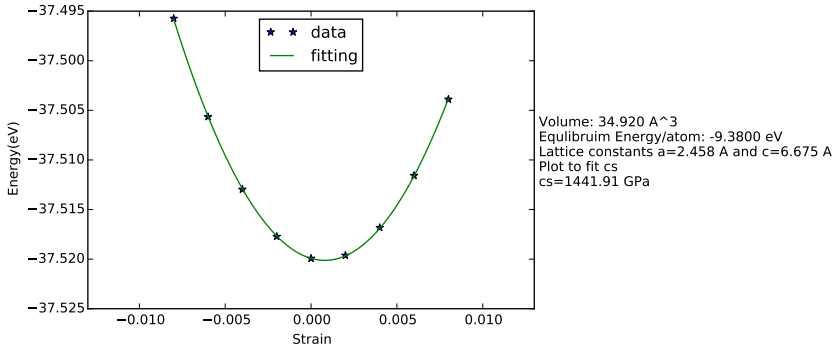

(c)

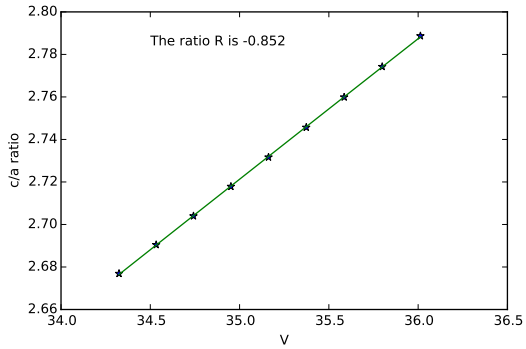

(d)

Figure 7.4: Fitting of energy vs. strain curve for different strain applied.

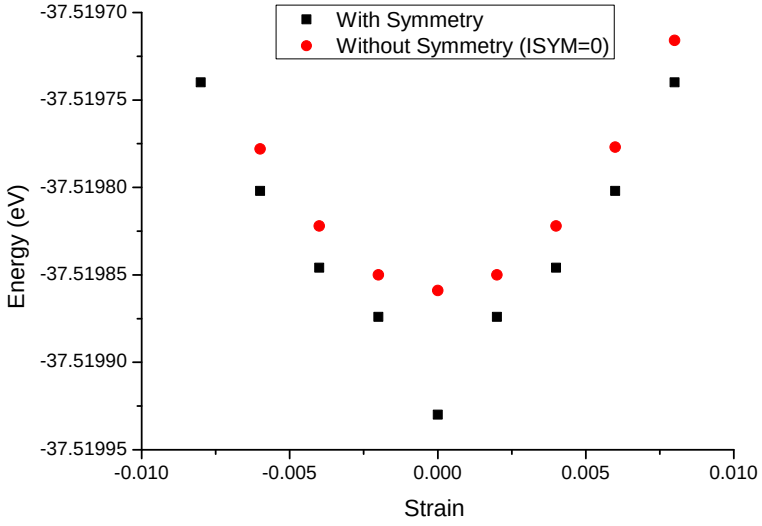

Figure 7.5: Comparison between calculations with and without symmetry, using strain corresponding to c_{44} of graphite. Turning off the symmetry makes the calculation result much closer to a parabola. But the energy difference considered here is below the accuracy of DFT.

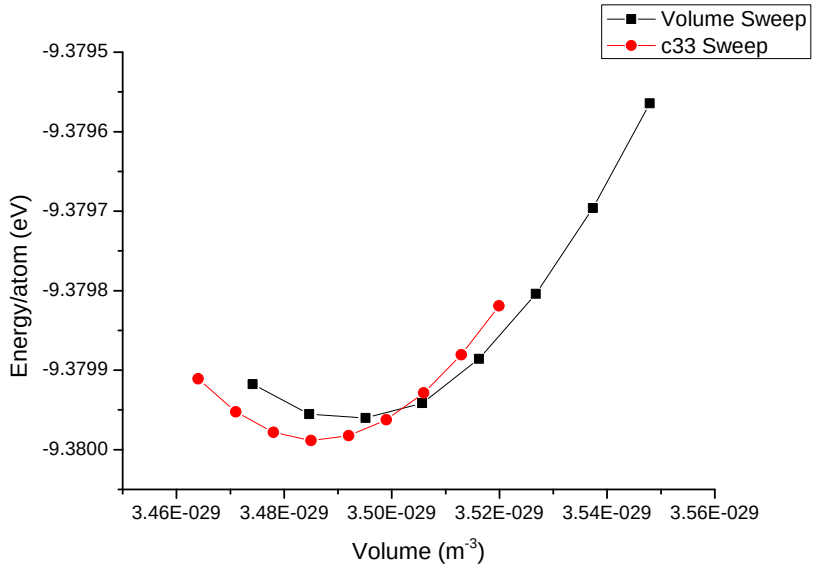

Figure 7.6: Comparison between volume sweep and c_{33} calculation of graphite, using GGA and TSvdW. The minimum found by volume sweep and c_{33} calculation are different.

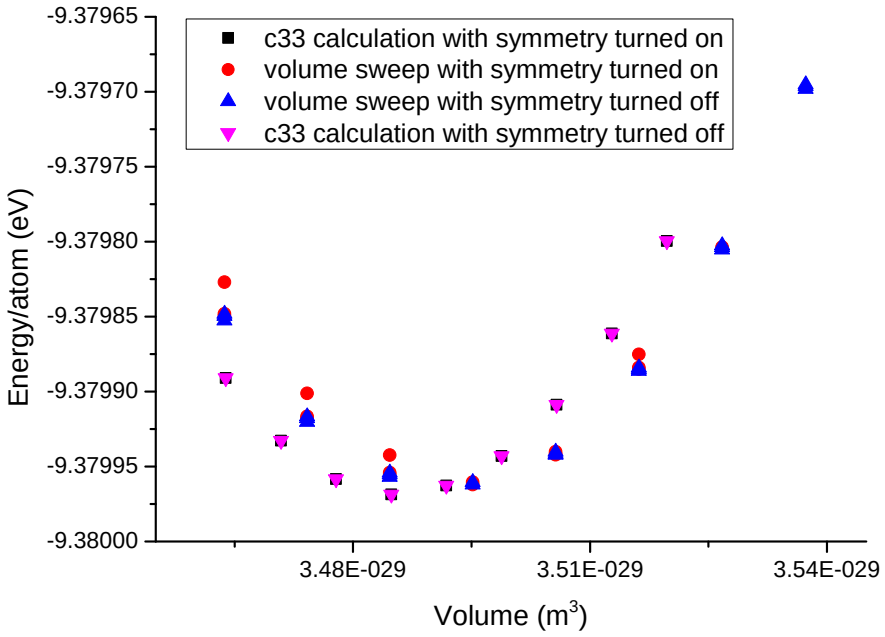

Figure 7.7: Comparison between volume sweep and c_{33} calculation of graphite, with symmetry turned on or off. Symmetry doesn't affect the calculation. The final results overlap with each other (the multiple red dots are steps before only 1 ionic step). The minimum found by volume sweep and c_{33} calculation are different.

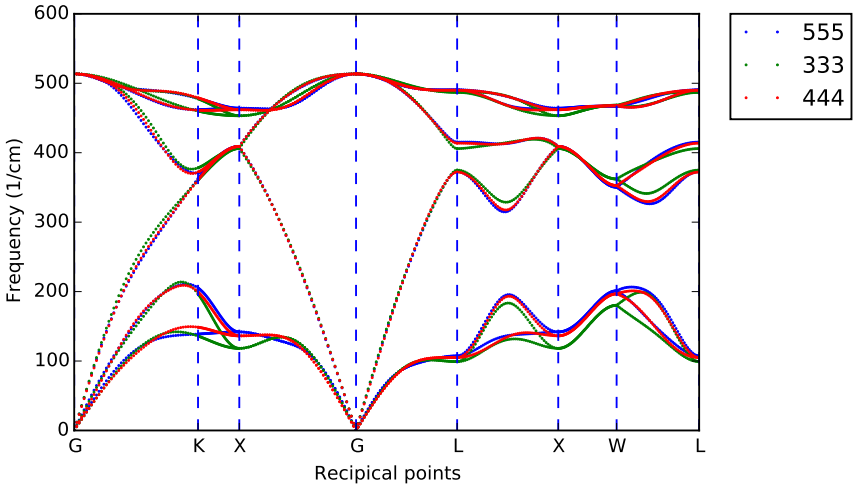

Figure 7.8: Convergence test for the size of supercell in phonon calculation of Si. "333" means a supercell of size $3 \times 3 \times 3$ of the unit cell, so is "444" and "555".

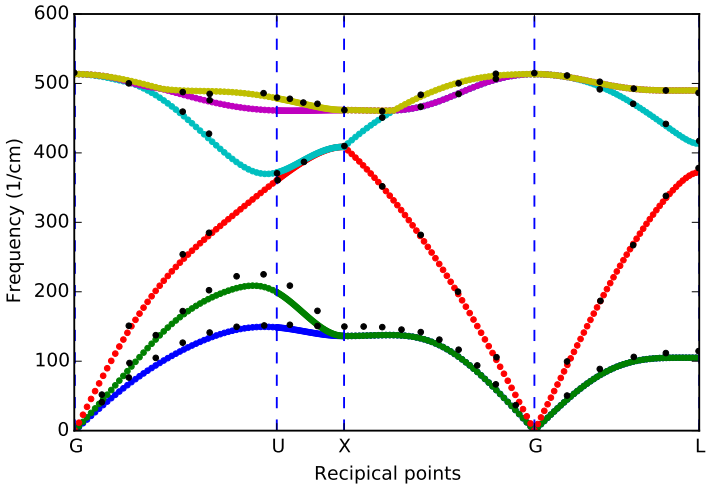

Figure 7.9: Phonon dispersion of Si: comparison between DFT calculation (color lines) and experiments [101] (black points).

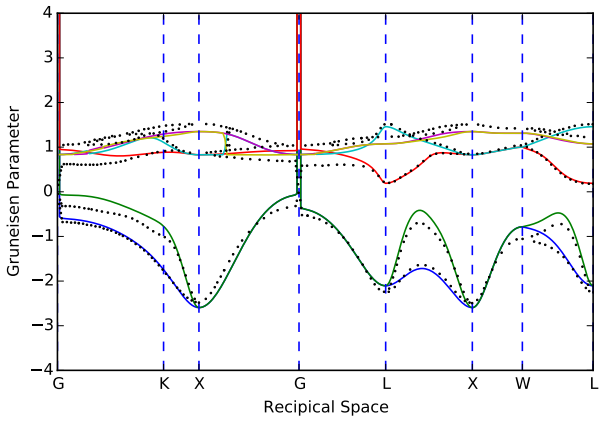

(a)

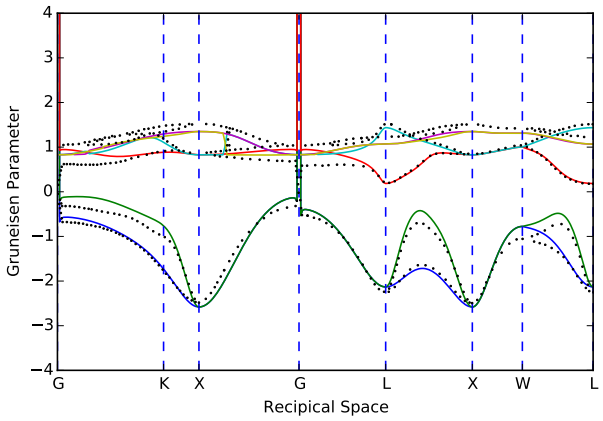

(b)

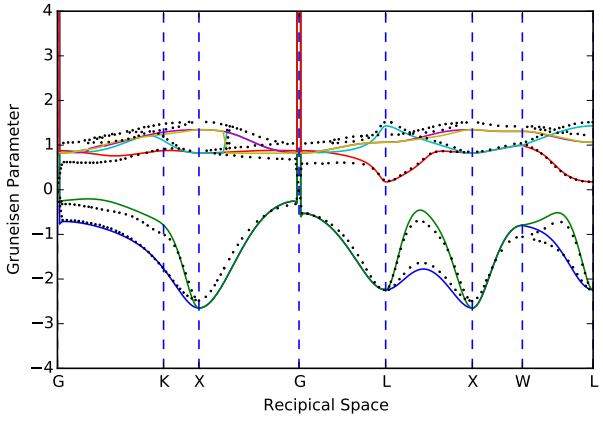

(c)

Figure 7.10: Comparison of calculated mode Grüneisen parameter. Color lines are my calculation and black dots are calculation from Ref. [102].(a). 0.3% volume change; (b). 0.6% volume change;(c). 0.9% volume change. Different volume changes have little effect on the calculation results.

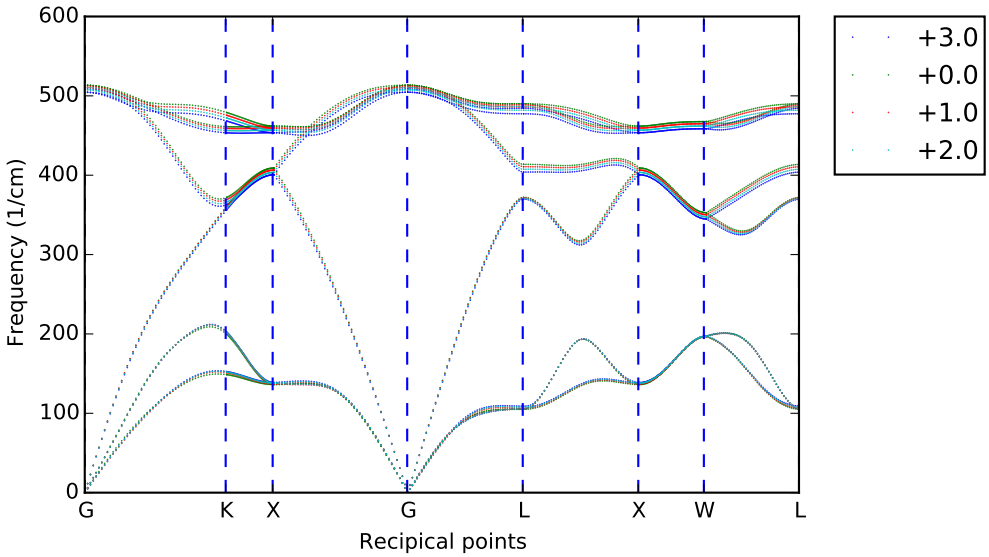

Figure 7.11: Comparison of phonon frequencies under different normal strain: 0%, +1%, +2%, and +3%.

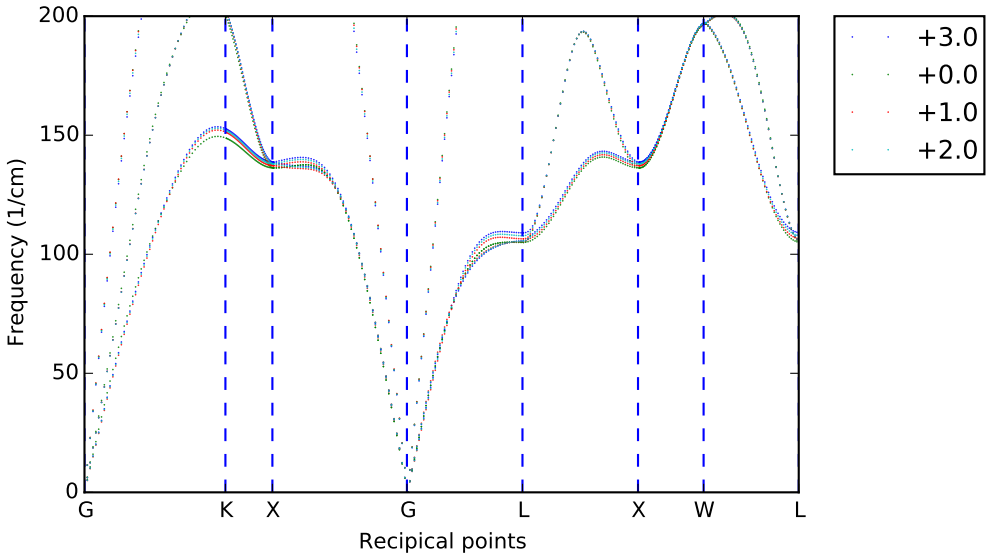

Figure 7.12: Acoustic phonon zoomed in of Fig. 7.11. The change of phonon frequency is not linear between zero and non-zero strain.

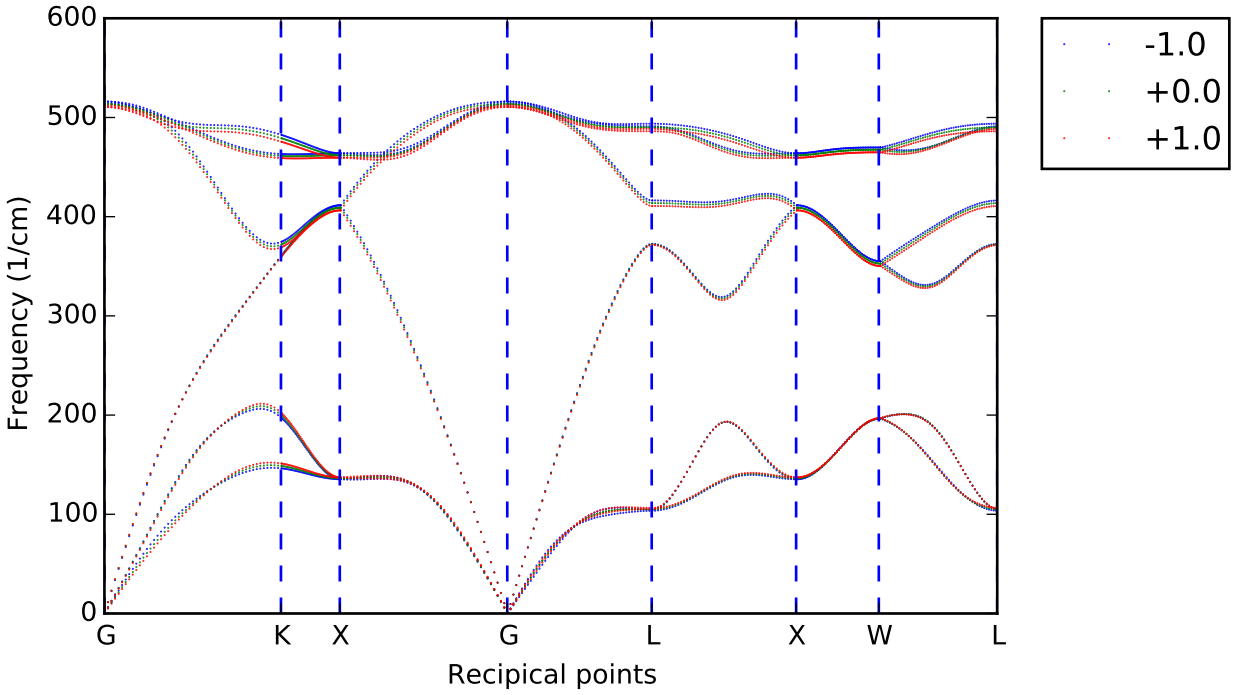

Figure 7.13: Comparison of phonon frequencies under different normal strain: -1%, 0%, +1%. The phonon frequency under no strain is at the center of phonon frequency under -1% and +1% strain.

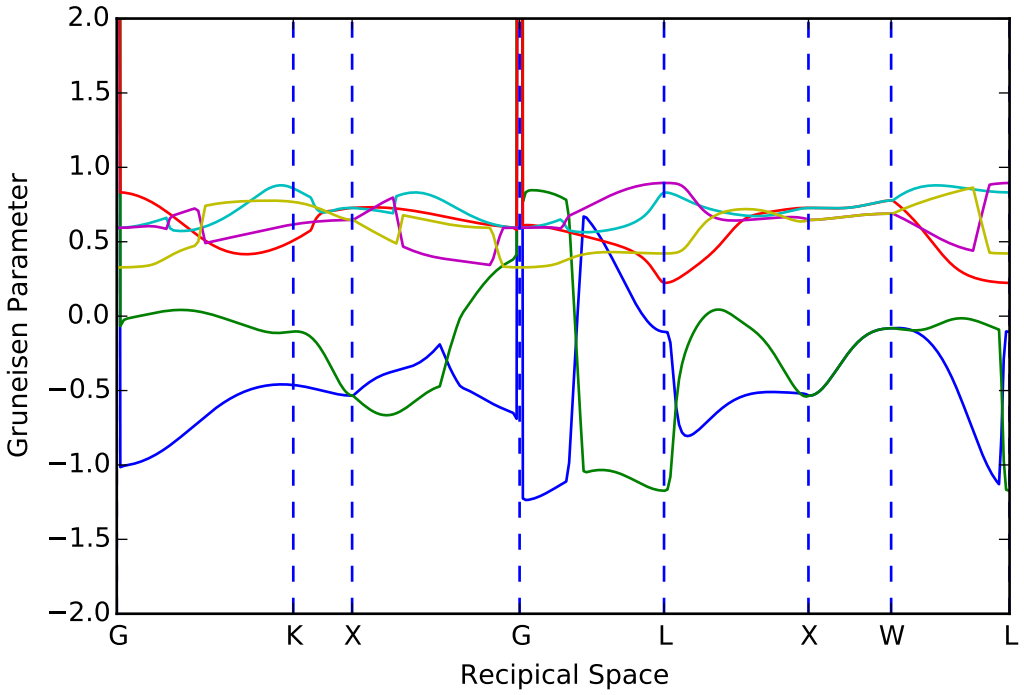

Figure 7.14: Generalized mode Grüneisen parameter of Si under normal strain. Calculated using results of +1% and +3% strain.

Table 7.1: Elastic constants of graphite. Comparison between my results and various results from references. The unit of elastic constants and bulk modulus is GPa; unit of lattice constant is Å. Note that my experiment is on HOPG which is the possible reason that c_{44} is smaller.

	Lattice Constant	Bulk Modulus	c_{11}	c_{12}	c_{33}	c_{44}	Method
My LDA	a=2.446, c=6.668	27	1091	211	27	4.67	LDA, no vdW
My GGA	a=2.454, c=6.690	60	1073	198	67	4.65	GGA, TS-vdW
My Exp					30.2	2	
Bosak[a]		36.4	1109	139	38.7	5.0	Exp.
Hasegawa[b]	a=2.441, c=6.64				30.4		LDA,no vdW
Mounet[c]		27.8	$c_{11}+c_{12}$=1283		29	4.5	LDA, no vdW
Bucko[d]	a=2.46, c=6.68	59					GGA, TSvdW
Al-Saidi[e]	a=2.46, c=6.65	56					GGA, TSvdW

[a]Phys. Rev. B 75, 153408 (2007)
[b]Phys. Rev. B 70, 205431 (2004)
[c]Phys. Rev. B 71, 205214 (2005)
[d]Phys. Rev. B 87, 064110 (2013)
[e]J. Chem. Theory Comput. 8, 1503(2012)

Table 7.2: Elastic constants of MoS_2. Comparison between my calculation result of MoS_2 and reference. The unit of elastic constants and bulk modulus is GPa; unit of lattice constant is Å

	Lattice Constant	Bulk Modulus	c_{11}	c_{12}	c_{13}	c_{33}	c_{44}	Method
My Cal	a=3.158, c=12.05	40.1	223	49.9	-59	51.8	16.9	TS, vdW
My Exp						54.1	15.4	
Exp1[a]	a=3.160, c=12.29	53						Exp.
Exp2[b]			238	-54	23	52	18.6	Exp.
Bucko[c]	a=3.16, c=12.01	43						GGA, TSvdW
Peelaers[d]			238	64	-68	57	18	hybrid
Volkova[e]	a=3.18, c=12.35		214	58		56	18	GGA, TS-vdW

[a] Z. Anorg. Allg. Chem. 541, 15 (1986)
[b] J. Phys. Chem. Solids 37, 141 (1976)
[c] Phys. Rev. B 87, 064110 (2013)
[d] J. Phys. Chem. C, 118, 12073 (2014)
[e] Phys. Rev. B 86, 104111 (2012)

CHAPTER 8

CONCLUSION

Despite the huge success of the application of piezoelectric material in ultrasonic techniques, new techniques are needed to meet the requirements in industry and scientific communities regarding the studies and applications of thin film materials. Optical measurement is inherently non-contact and non-destructive. The time-resolved optical pump-probe system using femtosecond pulse laser provides the highest possible frequency response. Both qualities make the optical pump-probe system an ideal candidate for high frequency acoustic wave applications. This dissertation makes several contributions to developing and improving surface acoustic wave (SAW) experimental techniques in optical pump-probe system. The calculations tools and processes developed along the way help the design, analysis, and understanding of the experiments.

I develop a simple and convenient method for measuring the velocity of surface acoustic waves at GHz frequencies using an elastomeric phase-shift mask. This approach is applicable to almost any samples with a smooth surface, without any micro-fabrication or special sample preparations. Using electromagnetic calculations, I obtain the optimal geometry of the phase-shift mask for high measurement efficiency corresponding to the 785 laser wavelength. The measurement is verified with various well known materials.

I implement the general calculations scheme for the properties of surface acoustic wave using Green's function methods. The software is capable of calculating surface acoustic wave of any layered structure with any number of layers of anisotropic materials. The properties that can be calculated include dispersion curve, as well as displacement of particles, stress, strain, and strain energy at different depth. With small changes, the software can further be used in calculation of other acoustic modes such as Lamb mode and Stoneley mode. The implementation should be able to cover almost any needs in the studies of acoustic mode in thin film structure. It can even calculate

acoustic modes with patterns of small mass, such as gratings. An analytical calculation software with numerical solution like this one is not only accurate but also convenient comparing with, for example, finite element simulations. One can deepen the physical intuition and understanding by using and tweak an analytical software, which is very difficult to achieve using a FE simulation software.

The shear elastic constants of various thin film materials that are difficult or maybe impossible to measure before, are measured using the SAW technique with phase-shift mask. Materials studied include hard materials grown by different deposition techniques, soft materials prepared by spin-coating, and layered materials prepared by mechanical exfoliation or thin film growth. Thickness of films under study spans from 60 nm to micron. The measured shear elastic constants have helped the analysis of thermal conductivity, magnetostrictive behavior, and to understand thin film quality for applications such as acoustic filters. When film thickness is small, thicker metal transducer on top can help improve the sensitivity. And the technique have one limitation that it cannot be used to measure SAW of typical polymer films of more than several hundred nanometer thick. But overall, I demonstrate the high versatility and compatibility of the SAW technique with phase-shift mask.

By fully understanding the details involved in propagation of surface acoustic wave generated by metal grating, I am able to design a better experiment and sample structure to measure the intrinsic attenuation of 7.2 GHz surface acoustic on Si, to be $\alpha_{Si} \approx 9\ \mathrm{cm}^{-1}$ at room temperature, which represents the intrinsic attenuation of transverse acoustic wave in Si. By fitting the attenuation at different temperature, I am able to obtain the phonon relaxation time under shear strain and the mean-squared variation of the generalized mode Grüneisen parameters. The result of small mean-squared variation of Grüneissen parameters for shear strain comparing with longitudinal strain indicates high Q factor for mechanical oscillator with mostly shear character. The experimental design can be readily used for other dielectric material. The attenuation properties obtained can be useful in the design of high frequency MEMS and acoustic filters.

DFT calculation is applied in calculation of second order elastic constant, phonon dispersion (both are harmonic behavior) and mode Grüneisen parameters (anharmonic behavior). The performance is generally good. How-

ever I observed that the numerical difference caused by the consideration of symmetry or not in DFT calculation (specifically `VASP`), can be appreciable when the strain applied is relatively small but big enough to break the crystal symmetry. This may not be a very serious problem if it's not the absolute values but the coefficients of change that matters.

REFERENCES

[1] L. Rayleigh, "On waves propagated along the plane surface of an elastic solid," *Proc. London Math. Soc.*, vol. 17, p. 4, 1885.

[2] R. Stoneley, "The propagation of surface elastic waves in a cubic crystal," *Proc. Roy. Soc. London*, vol. A232, p. 447, 1955.

[3] L. Gold, "Rayleigh wave propagation on anisotropic (cubic) media," *Phys. Rev.*, vol. 104, p. 1532, 1956.

[4] H. Deresiewicz and R. D. Mindlin, "Waves on the surface of a crystal," *J. Appl. Phys.*, vol. 28, p. 669, 1957.

[5] J. L. Synge, "Elastic waves in anisotropic media," *J. Math. Phys.*, vol. 35, p. 323, 1957.

[6] G. W. Farnell, "Properties of elastic surface waves," in *Physical Acoustics Vol 6* (W. P. Mason and R. N. Thurston, eds.), pp. 109–166, New York, USA: Academic Press, 1970.

[7] T. C. Lim and G. W. Farnell *J. Acoust. Soc. Am.*, vol. 45, p. 845, 1969.

[8] M. Matsuo, J. Ieda, K. Harii, E. Saitoh, and S. Maekawa, "Mechanical generation of spin current by spin-rotation coupling," *Phys. Rev. B*, vol. 87, p. 180402, 2013.

[9] E. M. Chudnovsky and R. Jaafar, "Manipulating the magnetization of a nanomagnet with surface acoustic waves: Spin-rotation mechanism," *Phys. Rev. Appl.*, vol. 5, p. 031002, 2016.

[10] W. J. M. Naber, T. Fujisawa, H. W. Liu, and W. G. van der Wiel, "Surface-acoustic-wave-induced transport in a double quantum dot," *Phys. Rev. lett.*, vol. 96, p. 136807, 2006.

[11] M. Weib, S. Kapfinger, T. Reichert, J. J. Finley, A. Wixforth, M. Kaniber, and H. J. Krenner, "Surface acoustic wave regulated single photon emission from a coupled quantum dotnanocavity system," *Appl. Phys. lett.*, vol. 109, p. 033015, 2016.

[12] C. H. W. barnes, J. M. Shilton, and A. M. Robinson, "Quantum computation using electrons trapped by surface acoustic waves," *Phys. Rev. B*, vol. 62, p. 8410, 2000.

[13] R. P. G. Mcneil, M. Kataoka, C. J. B. Ford, C. H. W. Barnes, D. Anderson, G. A. C. Jones, I. Farrer, and D. A. Ritchie, "On-demand single-electron transfer between distant quantum dots," *Nature*, vol. 477, p. 439, 2011.

[14] M. Kataoka, M. R. Astley, A. L. Thorn, D. K. L. Oi, C. H. W. Barnes, C. J. B. Ford, D. Anderson, G. A. C. Jones, I. Farrer, D. A. Ritchie, and M. Pepper, "Coherent time evolution of a single-electron wave function," *Phys. Rev. Lett.*, vol. 102, p. 156801, 2009.

[15] J. A. Rogers, A. A. Maznev, M. J. Banet, and K. A. Nelson *Annu. Rev. Mater. Sci.*, vol. 30, p. 117, 2000.

[16] R. M. Slayton, K. A. Nelson, and A. A. Maznev, "Transient grating measurements of film thickness in multilayer metal films," *J. Appl. Phys.*, vol. 90, p. 4392, 2001.

[17] A. J. Minnich, "Multidimensional quasiballistic thermal transport in transient grating spectroscopy," *Phys. Rev. B*, vol. 92, p. 085203, 2015.

[18] A. Vega-Flick, R. A. Duncan, J. K. Eliason, J. Cuffe, J. A. Johnson, J.-P. Peraud, L. Zeng, Z. Lu, A. A. Maznev, E. N. Wang, J. J. Alvarado-Gil, M. Sledzinska, C. M. S. Torres, G. Chen, and K. A. Nelson, "Thermal transport in suspended silicon membrances measured by laser-induced transient gratings," *AIP Advances*, vol. 6, p. 121903, 2016.

[19] T. Lee, K. Ohmori, C.-S. Shin, D. G. Cahill, I. Petrov, and J. E. Greene *Phys. Rev. B*, vol. 71, p. 144106, 2005.

[20] G. A. Paddock and G. L. Eesley, "Transient thermoreflectance from thin metal films," *J. Appl. Phys.*, vol. 60, p. 285, 1986.

[21] C. Thomsen, H. T. Grahn, H. J. Maris, and J. Tauc, "Surface generation and detection of phonons by picosecond light pulses," *Phys. Rev. B*, vol. 34, p. 4129, 1986.

[22] A. J. Schmidt, X. Chen, and G. Chen, "Pulse accumulation, radial heat conduction, and anisotropic thermal conductivity in pump-probe transient thermoreflectance," *Rev. Sci. Instru.*, vol. 79, p. 114902, 2008.

[23] D. G. Cahill, "Analysis of heat flow in layered structures for time-domain thermoreflectance," *Rev. Sci. Instrum.*, vol. 75, p. 5119, 2004.

[24] C. Thomsen, J. Strait, Z. Vardeny, H. J. Maris, J. Tauc, and J. J. Hauser, "Coherent phonon generation and detection by picosecond light pulses," *Phys. Rev. Lett.*, vol. 53, p. 989, 1984.

[25] B. C. Daly, K. Kang, Y. Wang, and D. G. Cahill *Phys. Rev. B*, vol. 80, p. 174112, 2009.

[26] D. Chanda, K. Shigeta, S. Gupta, T. Cain, A. Carlson, A. Mihi, A. J. Baca, G. R. Bogart, P. Braun, and J. A. Rogers *Nat. Nanotechnol.*, vol. 6, p. 402, 2011.

[27] S. Y. Chou, P. R. Krauss, and P. J. Renstrom *J. Vac. Sci. Technol.*, vol. 14, p. 4129, 1996.

[28] H. Schmid and B. Michel *Macromol.*, vol. 33, p. 3042, 2000.

[29] T. C. Lim and G. W. Farnell, "Search for forbidden directions of elastic surface wave propagation in anisotropic crystals," *J. Appl. Phys.*, vol. 39, p. 4319, 1968.

[30] X. Zhang, J. D. Comins, A. G. Every, P. R. Stoddart, W. Pang, and T. E. Derry *Phys. Rev. B*, vol. 58, p. 13677, 1998.

[31] D. Royer and E. Dieulesaint, "Rayleigh wave velocity and displacement in orthorhombic, tetragonal, hexagonal, and cubic crystals," *J. Acoust. Soc. Am.*, vol. 76, p. 1438, 1984.

[32] A. A. Maznev and A. G. Every *J. Appl. Phys.*, vol. 106, p. 113531, 2009.

[33] J. Park, X. Xie, D. Li, and D. G. Cahill, "Plasmonic sensing of ultrafast evaporation and condensation," *Nanoscale and Microscale Thermophysical Engineering*, 2016.

[34] J. Maria, V. Malyarchuk, J. White, and J. A. Rogers, "Experimental and computational studies of phase shift lithography with binary elastomeric masks," *J. Vacuum Sci. Tech. B*, vol. 24, p. 828, 2006.

[35] J. Aizenberg, J. A. Rogers, K. E. Paul, and G. M. Whitesides, "Imaging profiles of light intensity in the near field: applications to phase-shift photolithography," *Appl. Optics*, vol. 37, p. 2145, 1998.

[36] G. A. Antonelli, P. Zannitto, and H. J. Maris, "New method for the generation of surface acoustic waves of high frequency," *Physsica B*, 2002.

[37] Q. Miao, L.-W. Liu, T. Grimsley, A. V. Nurmikko, and H. J. Maris, "Picosecond ultrasonic measurements using an optical mask," *Ultrasonics*, vol. 56, p. 141, 2015.

[38] D. Li, P. Zhao, J.-C. Zhao, and D. G. Cahill *J. Appl. Phy.*, vol. 114, p. 143102, 2013.

[39] A. B. Mei, R. B. Wilson, D. Li, D. G. Cahill, A. Rockett, J. Birch, L. Hultman, J. E. Greene, and I. Petrov, "Elastic constants, poisson ratios, and the elastic anisotropy of vn(001), (011), and (111) epitaxial layers grown by reactive magnetron sputter deposition," *J. Appl. Phys.*, vol. 115, p. 214908, 2014.

[40] X. Xie, D. Li, T.-H. Tsai, J. Liu, P. V. Braun, and D. G. Cahill, "Thermal conductivity, heat capacity, and elastic constants of water-soluble polymers and polymer blends," *Macromolecules*, vol. 49, p. 972, 2016.

[41] J. Liu, X. Wang, D. Li, N. E. Coates, R. A. Segalman, and D. G. Cahill, "Thermal conductivity and elastic constants of pedot: Pss with high electrical conductivity," *Macromolecules*, vol. 48, p. 585, 2015.

[42] X. Xie, K. Yang, D. Li, T.-H. Tsai, J. Shin, P. V. Braun, and D. G. Cahill, "High and low thermal conductivity of amorphous macromolecules," *Phys. Rev. B*, vol. 95, p. 035406, 2017.

[43] C. Chiritescu, D. G. Cahill, N. Nguyen, D. C. Johnson, A. Bodapati, P. Keblinski, and P. Zschack *Science*, vol. 315, p. 351, 2007.

[44] N. S. Gunning, J. Feser, M. Beekman, D. G. Cahill, and D. C. Johnson *J. Am. Chem. Soc.*, vol. 137, p. 8803, 2015.

[45] G. J. Snyder and E. S. Toberer *Nat. Mater.*, vol. 7, p. 105, 2008.

[46] D. G. Cahill, P. V. Braun, G. Chen, D. R. Clarke, S. Fan, K. E. Goodson, P. Keblinski, W. P. King, G. D. Mahan, A. Majumdar, H. J. Maris, S. R. Phillpot, E. Pop, and L. Shi *Appl. Phys. Rev.*, vol. 1, p. 011305, 2014.

[47] Z. Wei, Y. Chen, and C. Dames *Appl. Phys. Lett.*, vol. 102, p. 011901, 2013.

[48] A. Kis, K. Jensen, S. Aloni, W. Mickelson, and A. Zettl *Phys. Rev. Lett.*, vol. 97, p. 025501, 2006.

[49] S. W. D. Bailey, I. Amanatidis, and C. J. Lambert *Phys. Rev. Lett.*, vol. 100, p. 256802, 2008.

[50] E. I. Volkova, I. A. Jones, R. Brooks, Y. Zhu, and E. Bichoutskaia *Phys. Rev. B*, vol. 86, p. 104111, 2012.

[51] J. L. Feldman *J. Phys. Chem. Solids*, vol. 37, p. 1141, 1976.

[52] N. S. Gunning, J. Feser, M. Falmbigl, M. Beekman, D. G. Cahill, and D. C. Johnson *Semicond. Sci. Technol.*, vol. 29, p. 124007, 2014.

[53] N. Wainfan and L. G. Parratt *J. Appl. Phys.*, vol. 31, p. 1331, 1960.

[54] M. Falmbigl, M. B. Alemayehu, D. R. Merrill, M. Beekman, and D. C. Johnson *Cryst. Res. Technol.*, vol. 50, p. 464, 2015.

[55] R. Atkins, D. B. Moore, and D. C. Johnson *Chem. Mater.*, vol. 25, p. 1744, 2013.

[56] M. B. Alemayehu, M. Falmbigl, K. Ta, and D. C. Johnson *Chem. Mater.*, vol. 27, p. 2158, 2015.

[57] C. K. Ghosh, D. Sarkar, M. K. Mitra, and K. K. Chattopadhyay *J. Phys. D: Appl. Phys.*, vol. 46, p. 395304, 2013.

[58] G. Savini, Y. J. Dappe, S. Oberg, J.-C. Charlier, M. I. Katsnelson, and A. Fasolino *Carbon*, vol. 49, p. 62, 2011.

[59] D. Li and D. G. Cahill *Phys. Rev. B*, vol. 94, p. 104306, 2016.

[60] H. J. Maris, "Interaction of sound waves with thermal phonons in dielectric crystals," in *Physical Acoustics Vol. 8* (W. P. Mason and R. N. Thurston, eds.), pp. 279–345, New York, USA: Academic Press, 1971.

[61] K. L. Ekinci and M. L. Roukes *Rev. Sci. Instrum.*, vol. 76, p. 061101, 2005.

[62] R. Lifshitz and M. L. Roukes *Phys. Rev. B*, vol. 61, p. 5600, 2000.

[63] X. Sun, X. Zhang, and H. X. Tang *Appl. Phys. Lett.*, vol. 100, p. 173116, 2012.

[64] A. Akhiezer *J. Phys. (USSR)*, vol. 1, p. 277, 1939.

[65] T. O. Woodruff and H. Ehrenreich *Phys. Rev.*, vol. 123, p. 1553, 1961.

[66] H. J. Maris *Phil. Mag.*, vol. 16, p. 331, 1967.

[67] W. P. Mason and T. B. Bateman *J. Acoust. Soc. Am*, vol. 36, p. 644, 1964.

[68] W. P. Mason, "Effect of impurities and phonon processes on the ultrasonic attenuation of germanium, crystal quartz, and silicon," in *Physical Acoustics Vol. 3B* (W. P. Mason, ed.), pp. 235–286, New York, USA: Academic Press, 1965.

[69] P. G. Klemens, "Effect of thermal and phonon processes on ultrasonic attenuation," in *Physical Acoustics Vol. 3B* (W. P. Mason, ed.), pp. 201–234, New York, USA: Academic Press, 1965.

[70] H. J. Maris *Phys. Rev.*, vol. 175, p. 1077, 1968.

[71] H. E. Bömmel and K. Dransfeld *Phys. Rev.*, vol. 117, p. 1245, 1960.

[72] J. Lamb and J. Richter *Proc. Roy. Soc. London A*, vol. 293, p. 479, 1966.

[73] S. Ghaffari, S. A. Chandorkar, S. Wang, E. J. Ng, C. H. Ahn, V. Hong, Y. Yang, and T. W. Kenny *Sci. Rep.*, vol. 3, p. 3244, 2013.

[74] J. Lamb, M. Redwood, and Z. Shteinshleifer *Phys. Rev. Lett*, vol. 3, p. 28, 1959.

[75] B. G. Helme and P. J. King *Phys. Stat. Sol. (a)*, vol. 45, p. K33, 1978.

[76] K. Lücke *J. Appl. Phys.*, vol. 27, p. 1433, 1956.

[77] Y. V. Ilisavskii and V. M. Sternin *Sov. Phys. Solid State*, vol. 27, p. 236, 1985.

[78] K. R. Keller *J. Appl. Phys.*, vol. 38, p. 3777, 1967.

[79] O. Matsuda, O. B. Wright, D. H. Hurley, V. E. Gusev, and K. Shimizu *Phys. Rev. Lett.*, vol. 93, p. 095501, 2004.

[80] A. A. Maznev, K. A. Nelson, and J. A. Rogers *Opt. Lett.*, vol. 23, p. 1319, 1998.

[81] J. Andrew J. Slobodnik *Proc. IEEE*, vol. 64, p. 581, 1976.

[82] J. Andrew J. Slobodnik *J. Appl. Phys*, vol. 43, p. 2565, 1972.

[83] D. Nardi, M. Travagliati, M. E. Siemens, Q. Li, M. M. Murnane, H. C. Kapteyn, G. Ferrini, F. Parmigiani, and F. Banfi *Nano. Lett.*, vol. 11, p. 4126, 2011.

[84] R. Loudon and J. R. Sandercock *J. Phys. C: Solid St. Phys.*, vol. 13, p. 2609, 1980.

[85] H. J. McSkimin, W. L. Bond, E. Buehler, and G. K. Teal *Phys. Rev.*, vol. 83, p. 1080, 1951.

[86] M. Tinkham, *Group Theory and Quantum Mechanics.* McGraw-Hill, Inc., 1964.

[87] M. Hamermesh, *Group Theory and Its Application to Physical Problems*. Addison-Wesley, Inc., 1962.

[88] B. Lüthi, *Physical Acoustics in the Solid State*. Springer-Verlag Berlin Heidelberg, 2005.

[89] M. P. Brassington and G. A. Saunders *Phys. Rev. Lett.*, vol. 48, p. 159, 1982.

[90] H. J. Maris *Phys. Rev.*, vol. 188, p. 1308, 1969.

[91] H. J. Maris *Phys. Rev. B*, vol. 28, p. 7033, 1983.

[92] M. R. Hauser, R. L. Weaver, and J. P. Wolfe *Phys. Rev. Lett*, vol. 68, p. 2604, 1992.

[93] H.-N. Lin, H. J. Maris, L. B. Freund, K. Y. Lee, H. Luhn, and D. P. Kern *J. Appl. Phys.*, vol. 73, p. 37, 1993.

[94] Y. Touloukian and C. Ho, *Thermophysical Properties of matter*. New York-Washington: IFI/Plenum, 1970-1975.

[95] K. Yum, Z. Wang, A. P. Suryavanshi, and M.-F. Yu *J. Appl. Phys*, vol. 96, p. 3933, 2004.

[96] Z. Hao, A. Erbil, and F. Ayazi *Sens. Actuators. A*, vol. 109, p. 156, 2003.

[97] I. Wilson-Rae *Phys. Rev. B*, vol. 77, p. 245418, 2008.

[98] A. A. Kiselev and G. J. Iafrate *Phys. Rev. B*, vol. 77, p. 205436, 2008.

[99] S. D. Lambade, G. G. Sahasrabudhe, and S. Rajagopalan *Phys. Rev. B*, vol. 51, p. 15861, 1995.

[100] G. Steinle-Neumann, L. Stixrude, and R. E. Cohen *Phys. Rev. B*, vol. 60, p. 791, 1999.

[101] G. Nilsson and G. Nelin *Phys. Rev. B*, vol. 6, p. 3777, 1972.

[102] K. Esfarjani, G. Chen, and H. T. Stokes *Phys. Rev. B*, vol. 84, p. 085204, 2011.

[103] R. N. Thurston and K. Brugger, "Third-order elastic constants and the velocity of small amplitude elastic waves in homogeneously stressed media," *Phys. Rev.*, vol. 133, p. A1604, 1964.

[104] K. Brugger, "Generalized grüneisen parameters in the anisotropic debye model," *Phys. Rev.*, vol. 137, p. A1826, 1965.